Formation Evaluation of Deep-water Reservoirs in the 13A and 14A Sequences of the Central Bredasdorp Basin, offshore South Africa

by

Tarig M. Hamad Hussien

Thesis presented in partial fulfilment of the requirements for the degree of ***Master of Science*** *at the University of The Western Cape*

Department of Earth Sciences,
University of the Western Cape,
Bellville, South Africa.

Supervisor: Dr. Mimonitu Opuwari

November 2014

Abstract

Formation Evaluation of Deep-water Reservoirs in the 13A and 14A Sequences of the Central Bredasdorp Basin, offshore South Africa

T.M Hammad Hussien

Department of Earth Sciences,
University of the Western Cape,
Bellville, South Africa.

Thesis: MSc

November 2014

The goal of this study is to enhance the evaluation of subsurface reservoirs by improving the prediction of petrophysical parameters through the integration of wireline logs and core measurements. Formation evaluations of 13A and 14A sequences in the Bredasdorp Basin, offshore South Africa have been performed. Five wells in the central area of the basin have been selected for this study.

Four different lithofacies (A, B, C, D) were identified, in the two cored wells, and used to predict the lithofacies from wireline logs in uncored intervals and wells. A method based on artificial neural network was used for this prediction. Facies A and B were recognized as reservoir rocks and 13 reservoir zones were identified and successfully evaluated in a detailed petrophysical model.

The final shale volume was considered to be the minimum among five different methods applied in this study at any point along the well log. The porosity model was taken from the density model. A value of 2.66 g/cm^3 was obtained from core measurements as the field average grain density, whereas the value of the fluid density of 0.79 g/cm^3 was obtained from core porosity and bulk density cross-plot.

In a water saturation model; an average water resistivity of 0.135 Ohm-m was estimated from SP method. The calculated water saturation models were calibrated with core measurements, and the Indonesia model best matched with the water saturation from conventional core analysis.

Six hydraulic flow units were recognized in the studied reservoirs, and were used for permeability predictions. The permeability predicted from hydraulic flow units were found more reliable than the permeability calculated from porosity-permeability relationship.

The net pay was identified for each reservoir by applying cut-offs on permeability 0.1 mD, porosity 7%, shale volume 0.35, and water saturation 0.60. The gross thickness of the reservoirs ranges from 4.83m to 41.07m and net pay intervals from 1.21m to 29.59m.

Declaration

I declare that Formation Evaluation of Deep-Water Reservoirs in the 13A and 14A Sequences of the Central Bredasdorp Basin, offshore South Africa is my own work, that it has not been submitted before for any degree or examination in any other University, and that all the sources I have used or quoted have been indicated and acknowledged by means of complete references.

Tarig M. Hamad Hussien

November 2014

Signature .....

Acknowledgements

This work has reached its successful completion mainly because of the help of so many people. I would like to express my sincere gratitude to my supervisor, Dr. Mimonito Opuwari, for his guidance and assistance.

Special thanks to the Earth Science Department of University of the Western Cape, for the use of their facilities to conduct my research.

To my parents for their understanding, and words of encouragement, during my research which helped me focus my effort and bring it to conclusion.

My deepest appreciation to my dear wife Amany Kamblawe, who has always encouraged me with love, patience, and understanding, I owe much of my success to her.

But above all, I would like to thank the Almighty Allah for everything that he has given to me, for his blessings and guidance to finish this work.

Contents

List of Figures

List of Tables

Chapter 1

Introduction

1.1 Preface

Formation evaluation is the process of interpreting a combination of measurements taken inside a porehole to detect and quantify hydrocarbon reserves in the strata adjacent to the porehole. It also involves determining of both, physical and chemical properties of rocks and the fluids they contain. This evaluation mainly depends on wireline logs which measure these various physical and chemical properties of the formations (Alger, 1980). These logs are commonly used for the determination of certain petrophysical properties of rocks such as porosity, permeability, water saturation and possibly pore geometry.

The petrophysical evaluation of subsurface strata also involves integration of different datasets from multiple disciplines for better reservoir description (Gunter et al., 1997). Normally, geologists use core measurements, seismic and well testing to improve the wireline petrophysical model. Core data presents an important means to calibrate a petrophysical model as it provides vital information unavailable from either wireline logs or productivity tests (Al-Saddique et al., 2000).

The Bredasdorp Basin is located off the south coast of South Africa. Five wells in the central area of the basin have been chosen for this study. The purpose of this study is to describe, characterize and quantify the reservoir properties of the basin by integrating the sedimentary facies characteristics and petrophysical properties. The study investigates the relationships between primary depositional facies and petrophysical properties; porosity, permeability and saturation.

1.2 Aims of the study

The main aim of any reservoir characterization is to quantify and describe the spatial distribution of petrophysical parameters, such as shale volume, porosity, permeability, and saturations for the purpose of defining flow units within it. Accurate knowledge of these parameters for any hydrocarbon reservoir is required for efficient development, management, and prediction of future performance of the oil field. Wireline logs offer the opportunity for determining the petrophysical parameters, while core data presents an important means to calibrate the petrophysical model.

The main goal of this research is to perform a complete characterization of the central Bredasdorp Basin through the integration and comparison of results from core analysis and petrophysical studies. The sand zones in the Bredasdorp Basin are considered as low permeability reservoirs. Reservoir characterization is the key for understanding the primary depositional facies which may control this low permeability. Another challenge is predicting of facies from wireline log using neural networks.

The process for achieving a complete characterization requires the following:

- Perform data quality control through the environmental corrections for wireline logs and overburden corrections for core data.

- To investigate the reservoir sedimentological characteristics of the basin strata and predict the lithofacies.

- Estimate petrophysical properties from the wire line logs data.

- To calculate the net pay of the studied reservoirs.

1.3 Location of the study area

The Bredasdorp Basin is located off the south coast of South Africa. The basin is the most south-westerly of the Southern African offshore basins as presented in figure 1.1 below. The study area of this project is situated in the central part of the basin. Five wells were selected for this research: E-AD1, E-AO1, E-AO2, E-BB1 and E-BB2. Figure 1.2 shows the distribution of the studied wells across the centre of the Bredasdorp Basin.

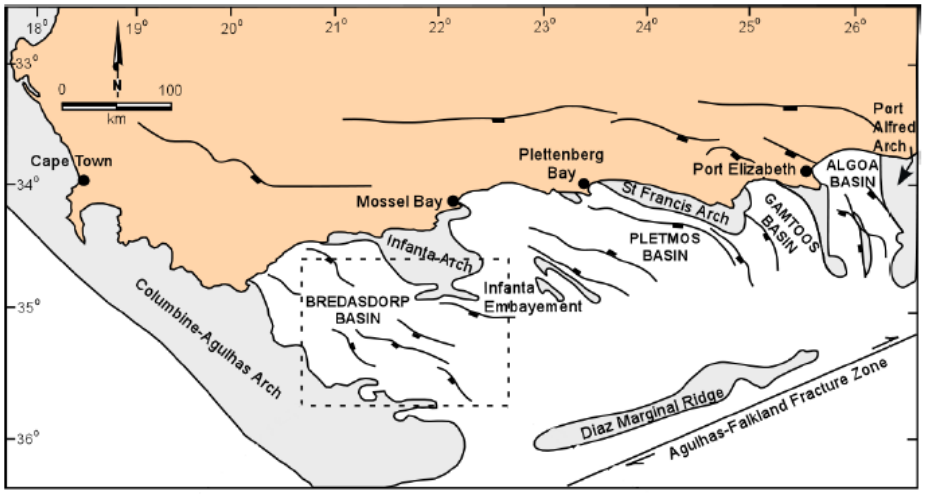

Figure 1.1: Location map showing the Bredasdorp Basin, offshore South Africa (modified from (McLachlan and McMillan, 1976).

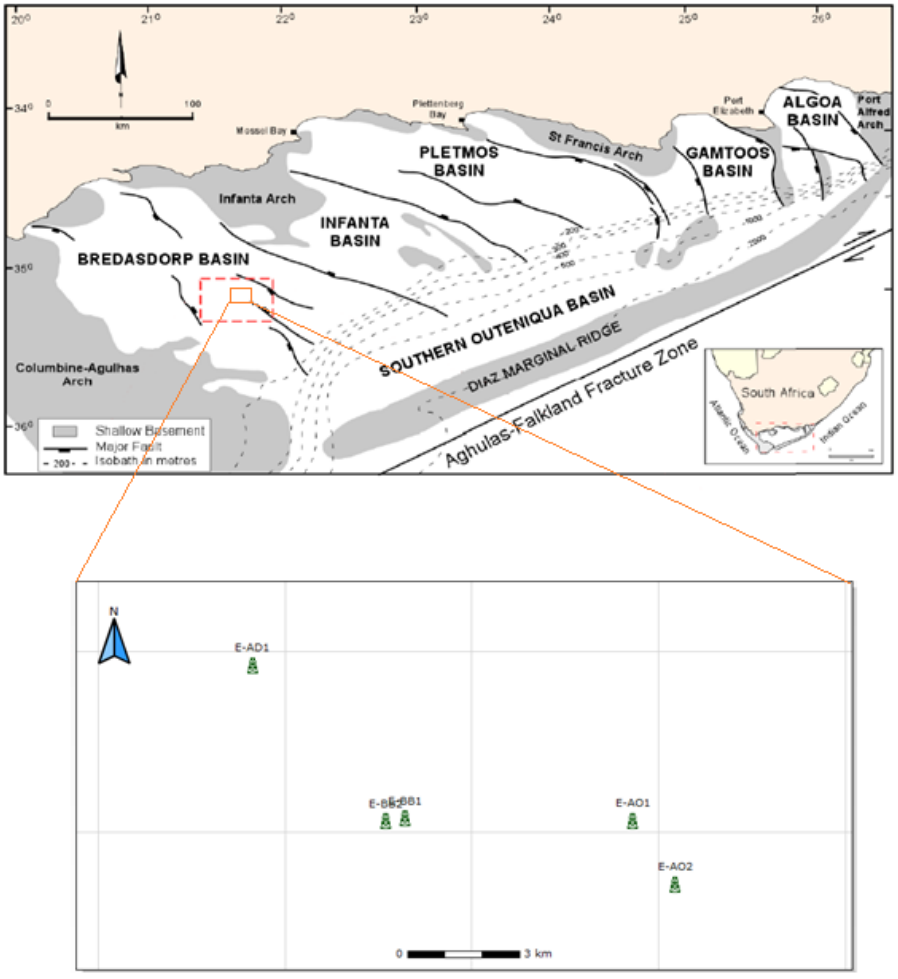

Figure 1.2: Location map showing distribution of wells in this study across the centre of the Bredasdorp Basin (modified from (Burden and Davies, 1997)).

1.4 Data set

The collected data for this study was classified into two main groups:

1. Wireline logs of the five studied wells.

2. Core analysis data from two wells E-AO1 and E-BB1.

All data has been provided by the Petroleum Agency of South Africa (PASA). The details of the data is given in chapter three.

1.5 Thesis structure

This thesis represents the written report of the research carried out to evaluate the hydrocarbon potential of 13A and 14A sequences in the central part of the Bredasdorp Basin.

In chapter one a general introduction to the study is given. The structure and sequences stratigraphy of the Bredasdorp Basin are briefly reviewed in the second chapter. The third presents the methodology of the study, with the corrections applied to the core and wireline data. Facies predictions from both core data and wireline logs are discussed in chapter four. Chapter four also includes determinations of the sequence boundaries of the studied interval and determinations of reservoirs zones within the interval. The petrophysical model is presented in detail in chapter five. Chapter six presents the determinations of the cut-off values and net pay of the studied reservoirs. With chapter seven covering remarks and conclusions drawn from the study.

Chapter 2

Geological Setting of the Bredasdorp Basin

In this chapter, a description of the Bredasdorp Basin is presented. This description introduces the structural development in favour of a detailed study of the stratigraphy, from which the sedimentation history might be determined. The Bredasdorp Basin is located off the south coast of South Africa, beneath the Indian Ocean. It covers about 18, 000km^2 (200km long and 80km wide) (McMillan et al., 1997).

2.1 The Structural Development of the Bredasdorp Basin

The South African coastline has a total length of about 3000 km. The west coast from the Orange River to Cape Point is almost 900 km long and the remainder, from Cape Point to the Mozambique border, is more than 2000 km long (PASA, 2008). The continental margin, along this coastline, formed as a result of the separation of South America, Africa and the Falkland Plateau (McMillan et al., 1997; Liro and Dawson, 2000). Three major offshore basins developed in western, southern and eastern South Africa, these are respectively the: Orange, Outeniqua and Durban basins (PASA, 2005).

The Outeniqua Basin in particular, developed as a result of the right-lateral shear movement along the Falkland-Agulhas Fracture Zone, which resulted in the separation of the Falkland Plateau from the Mozambique Ridge, and the break-up of west Gondwana (South America and Africa) during the Jurassic period (Tinker et al., 2008). During this time the normal faulting resulted in the graben and half-graben basins (Brown et al., 1995).

The Outeniqua Basin is bounded to the west by the Columbine-Agulhas Arch, to the east by the Port Alfred Arch, and to the south by the Diaz Marginal Ridge. It comprises of a series of rift sub-basins which are separated by fault-bounded Basement arches. These are, from east to west; Algoa, Gamtoos, Pletmos, and the Bredasdorp basins. Figure 2.1 shows the Southern African coastline, and the offshore basins and sub-basins.

Figure 2.1: (The Southern African offshore basins (modified from (PASA, 2003))

The Bredasdorp Basin can be described as a wide depression basement. The major structural features of the Bredasdorp Basin are the normal faults. These faults present a WNW-ESE trend, and bound half-grabens and structural highs throughout the basin (figure 2.2) (De Wit and Ransome, 1992). In general, the half-graben feature is developed when normal faults are dipping in the same direction making adjacent fault blocks to slip down and tilt relative to the fault next to it (Schalkwyk, 2005).

The break-up of Gondwana produced extensional stress, which led to the formation of the pull-apart basin represented in the Outeniqua Basin. This followed by the right-lateral movement along the Agulhas-Falkland Fracture Zone led to the creation of the half-graben sub-basins including the Bredasdorp Basin.

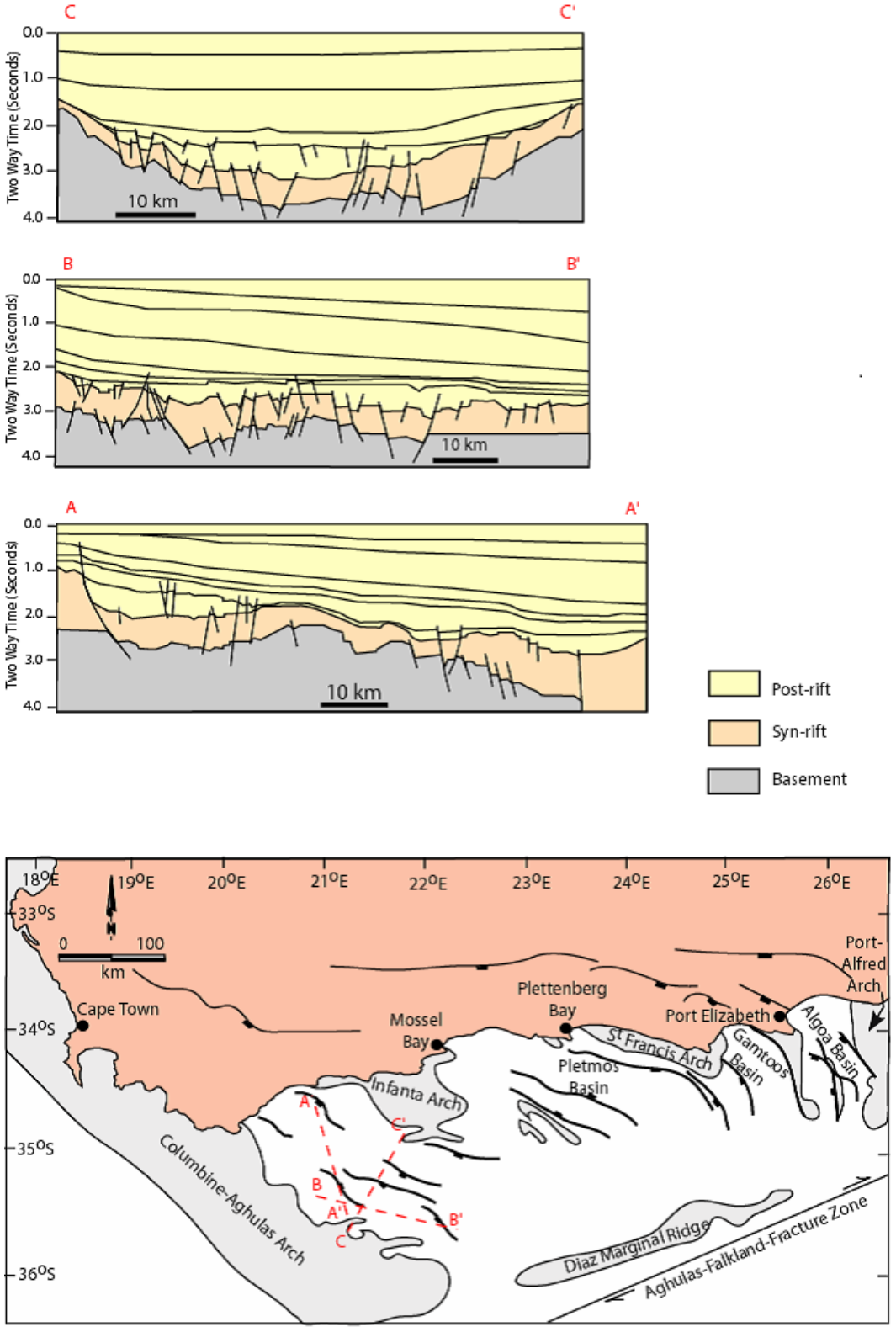

Figure 2.2: Three schematic cross-sections across the Bredasdorp Basin (from (Thomson, 1998)).

2.2 Stratigraphy and Sedimentology of the Bredasdorp Basin

The deposition in the Bredasdorp Basin is mainly controlled by the initial continental rifting and tectonic development. According to (McMillan et al., 1997) this rifting phase was followed by a transitional episode and then a drifting episode. A regionally correlatable unconformity 1At1 terminated the active rift tectonics and separates the syn-rift and post-rift sequences. The deposition of sediments in theses successions has been mainly controlled by global sea level change. The description of these successions is discussed in further detail further in this chapter. The stratigraphic chart of the Bredasdorp Basin is presented in figure 2.3.

2.2.1 Syn-rift Succession

The sedimentation rate of this sequence, which is bounded by horizon D and 1At1, was strongly influenced by the differential subsidence of the basement floor. All lithogenetic units, which consist of Late Jurassic to Early Cretaceous-aged sediments, rest unconformably on faulted basement within graben and condense over horsts (Figure 2.4).

The sediments within this interval consist of alluvial and channel fluvial deposits that accumulated with faulting (Burden, 1992). (McMillan et al., 1997) identified four lithogenetic units in the rift sediments in the Bredasdorp Basin, these are:

1. The lower fluvial unit. This unit consists of red and minor green argillite with subordinate reddish sandstones and rare conglomerates.

2. The lower shallow marine unit. This unit is considered to be the first marine deposit in the basin. It occurred at an erosional regional unconformity marked by the appearance of glauconitic, clean, fine grained sandstones.

3. The upper fluvial unit. This unit overlying the shallow marine sediments, it consists of interbedded non-glauconitic sandstones, red and green claystones, and siltstones.

4. The upper shallow marine unit. This unit was deposited in the second marine transgression, and it is characterized by the second occurrence of the glauconitic sandstones.

The deposition of syn-rift sediments was followed by a tectonically controlled break in sedimentation. The erosion of rift sediments during this period resulted in the formation of 1At1 unconformity.

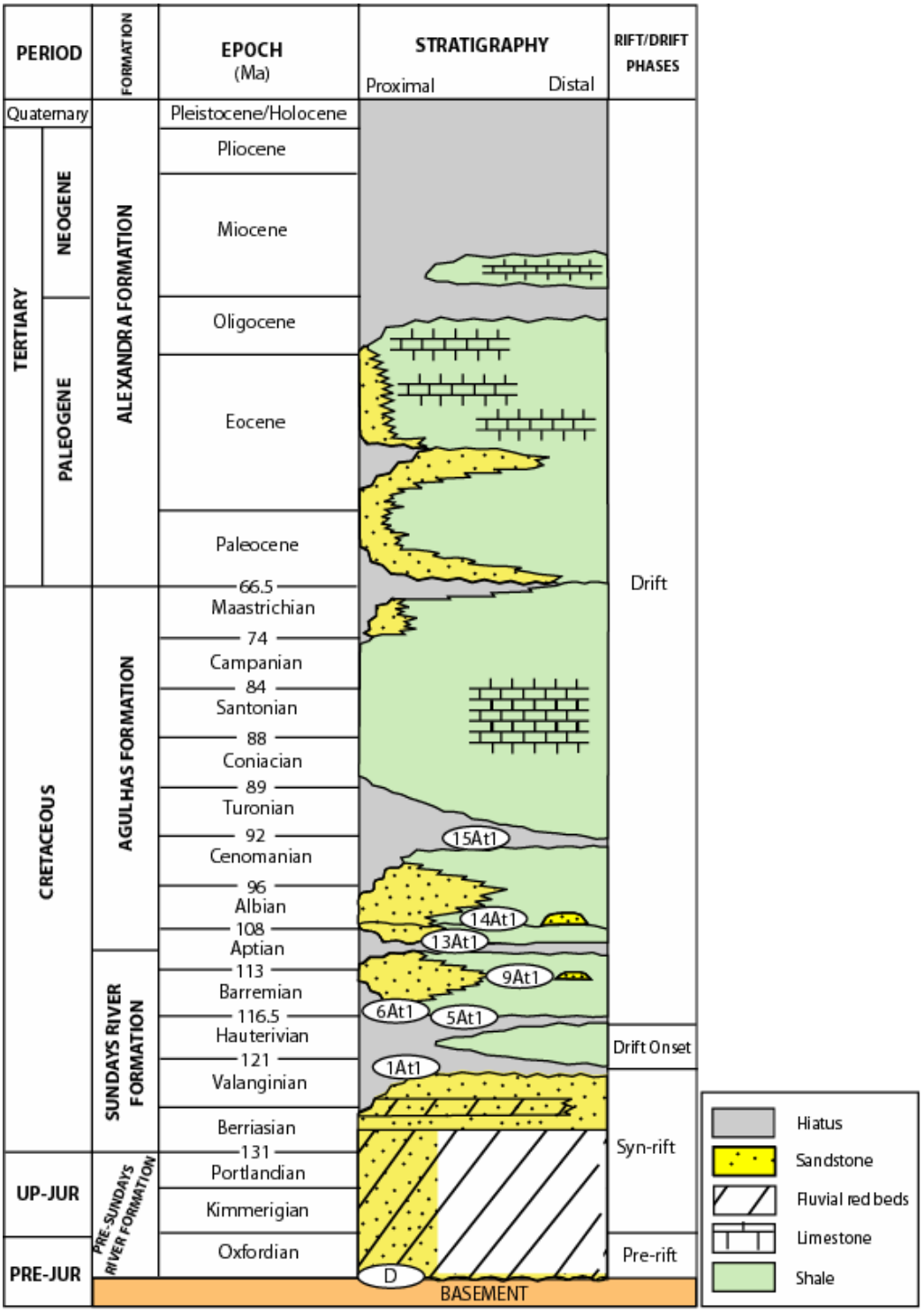

Figure 2.3: Stratigraphic chart of the Bredasdorp Basin (from Burden, 1992).

2.2.2 Drift Succession

The sea level rise after the rifting phase established an open marine environment in the Bredasdorp Basin during Mid-Cretaceous. These conditions allowed for deposits of shelf

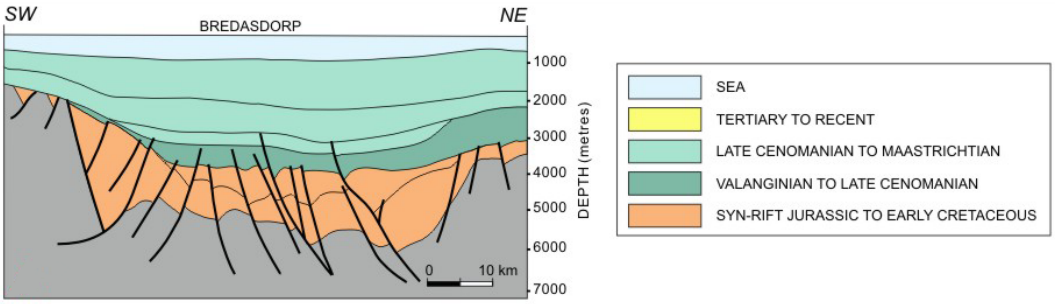

Figure 2.4: Rift faulting in the Bredasdorp Basin ((PASA, 2003)).

and slope shales, and channelised sandstone.

According to (McMillan et al., 1997), this sequence, from 1At1 to present, is divided into two intervals:

1. Transitional to early drift sequences.
2. Late drift sequence.

2.2.2.1 Transitional to early drift sequences

These sequences bounded on the bottom and top by 1At1 and 13At1 unconformities respectively. It considered as the first deep water deposits in the Bredasdorp Basin, deposits as result of major subsidence of the basin, and the increase of water depth. Deep-water environment sedimentation took place with low oxygen levels due to poor circulation in the overlying water column (McMillan et al., 1997).

2.2.2.2 Late drift sequences

These sequences followed a major marine regression in the Bredasdorp Basin during early Aptian. This regression caused significant erosion marked by the regional 13At1 unconformity. The marine transgression following this erosion carried organic rich claystone deposited under low oxygen conditions (McMillan et al., 1997).

Chapter 3

Methodology and Materials

This chapter describes the methodology and materials used to conduct the research project. The data available for the study is listed, with an outline of the various methods used to correct the data. The collected data is classified into two main groups: wireline logs of the five studied wells, and core analysis data from two wells. All the data has been provided by the Petroleum Agency of South Africa (PASA).

3.1 Methodology

Figure 3.1 presents the flow chart of the various methods used in this study. The process followed the following sequence:

1. Review the previous studies on the Bredasdorp Basin to become familiar with the basin tectonic history and structural features. The review also includes sequence stratigraphy studies of the basin, to understand the evolution of the sedimentary environment.

2. Develop a geological model based on the core data and wireline logs. The core data is used to identify the lithofacies; then the integration between core and wireline logs is used to calculate the electrofacies for all studied wells. The wireline logs and the calculated electrofacies are used to infer sequences boundaries.

3. Develop a petrophysical model dependent on wireline logs and core data to determine shale volume porosity, permeability and water saturation.

4. The petrophysical model is then used for determinations of cut-offs and net pay within the studied reservoirs to identify the hydrocarbons intervals.

5. Develop written report.

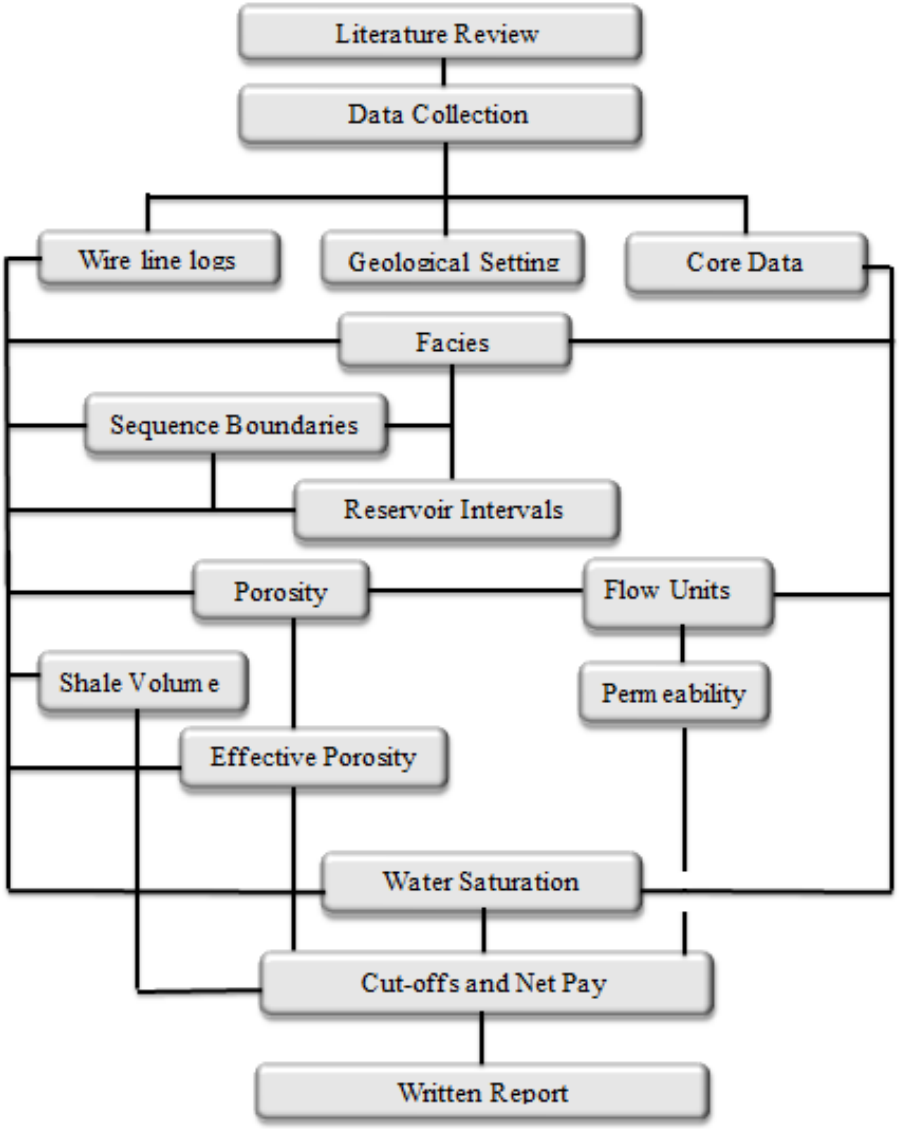

Figure 3.1: Research methodology flow chart.

The available data was carefully arranged and imported into Techlog software and the required corrections were done when necessary. The details of each data set, and the applied corrections are described and discussed further in this chapter.

3.2 Wireline Data

Wireline logs were collected from the five studied wells penetrating the central Bredasdorp Basin sandstones; the logging was carried out by Schlumberger Company in all the wells. The logs were provided in LAS file format, and only twelve of the many possible logs were used as primary logs in this study. The logs used were:

- The Caliper (CL)
- Gamma Ray (GR)
- Spontaneous Potential (SP)
- Microspherically Focussed (MSFL)
- Deep Laterolog (LLD)
- Shallow Laterolog (LLS)
- Medium Laterolog (LLM)
- Deep Induction (ILD)
- Shallow Induction (ILS)
- Density (RHOB)
- Neutron (NPHI)
- Sonic logs (DT)

The digital suites of the logs were imported into the Techlog software workstation. Before processing interpretation, the quality of the logs were checked, and editing performed where required. The editing included for following: depth shifting, environmental corrections, normalization, and curve splicing.

3.2.1 Depth shifting

Reservoir characterization involves the integration of wireline data from different tools runs. Consequently, measurements of formation properties from different tools runs must be depth shifted so that a log plot of formation properties versus depth puts all the properties at the correct location (Moake, 2008). The difference between logs recorded in the same borehole may exist due to borehole irregularities and tool type (Bassiouni, 1994).

Normally the logs which have been logged during the same logging run are considered to be in depth, and no depth shifting is required for them.

For this study, all logging runs were depth checked, the gamma ray logs were assumed to be the reference depth and two shale zones were used as correlation markers. When a gamma ray log is run on more than one tools run the reference gamma ray is chosen based on cable tension and cable speed. A single log has been chosen from each logging run to depth match against the depth reference log. Both logs were displayed side by side to allow visual correlation and define appropriate shift. In figure 3.2 , seven different logs from different data sets in E-AD1 are plotted together. All the logs are in depth except RHOB in track 7, which is 3.32 m shallower.

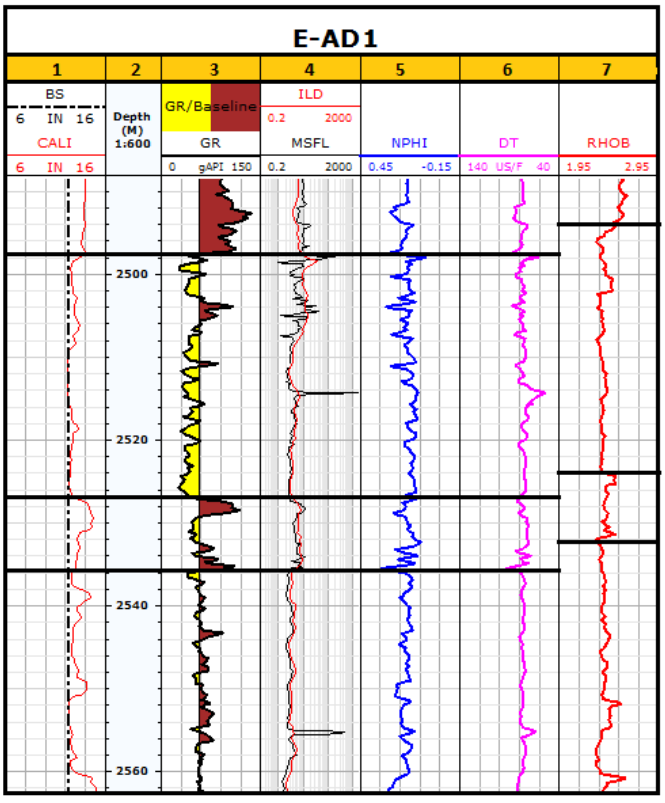

Figure 3.2: Example of gamma ray log used as reference to check the depth shift in different datasets in E-AD1.

3.2.2 Borehole Environmental Corrections

The objective of logging is to obtain undisturbed values for the formation properties. This is hardly accomplished because the drilling processes disturb the formation near the borehole. Borehole effects on wireline logs can be divided into those produced by borehole

geometry, drilling fluids conditions and mud cake. These parameters must be controlled to improve the quality of wireline logs data.

Rough or rugose borehole walls have the largest influences in the logs responds, the effect of enlarged borehole size on logs can be significant and it affects most logs to greater or lesser extent. Borehole enlargement beyond the bit size influences the reading of centralized tools, while rugose borehole influences pad type tools. Therefore, the borehole diameter is the mandatory input in any environmental correction procedure.

In this project environmental corrections were performed to compensate for most of the unwanted borehole effects.

3.2.2.1 Gamma Ray (GR)

Any material with non-zero density in the annular space between the walls of the borehole and the gamma ray detectors represents a disruptive environment to the measurement process. This medium will affect the tool readings by certain degrees of ray scattering and absorption, and thus decrease the final count rate (Lehmann, 2010).

Gamma ray environmental corrections have been historically presented in different forms using different assumptions. Open hole conditions have been applied to the studied wells measurements to compensate for hole size, mud weight and tool position. The corrections corrections in this study have been performed using both the Techlog software environmental corrections module and Schlumberger log interpretation charts book for comparisons. The essential input parameters were raw gamma ray logs, borehole diameter and fluid density.

Figure 3.3 presents an example of an uncorrected gamma ray log and environmentally corrected log for E-OA1 borehole. The green curve is the uncorrected gamma ray log, while the blue curve is the corrected one. In track one; caliper and bit size are plotted to show the effect of the borehole enlargement.

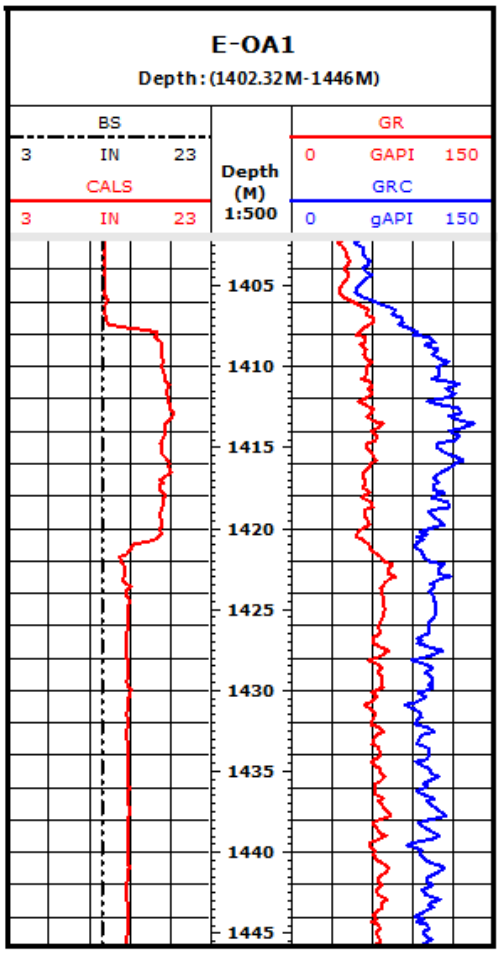

Figure 3.3: Graphics of uncorrected and corrected gamma ray logs.

Figure 3.4 below represents Schlumberger gamma ray corrections chart for hole size and mud weight (Schlumberger, 1989). The input parameter (t) in g/cm^2, is calculated as follows:

$$t = \frac{mud_w}{8.345}\left(\frac{2.54(hole_d)}{2} - \frac{2.54(tool_d)}{2}\right) \tag{3.1}$$

where:
t: The input parameter (g/cm^2)
mud_w : Mud weight (lb/gal)
$hole_d$: Hole diameter (in)
$tool_d$: Tool diameter (in)

For comparison with Figure 3.3 in depth 1424.40m gamma ray reads 67.63 API units. The input parameter (t) is 16.3 g/cm^2 (mud weight 1.1 Gram per Cubic Centimetre

(g/cm^3) equal to 9.18 pounds per gallon (lb/gal) resulting in a correction factor of 1.60. Therefore the corrected gamma ray is 108.20 API units, which is equal to the calculated value (107.25 API).

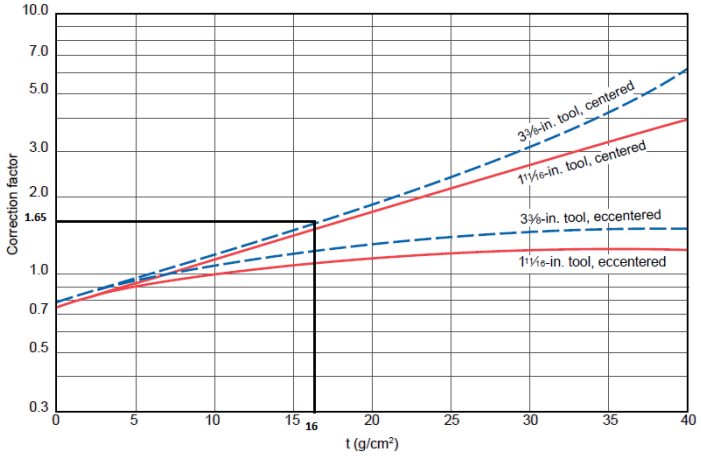

Figure 3.4: Schlumberger gamma ray corrections chart (modified from (Schlumberger, 1989)).

3.2.2.2 Neutron (NPHI)

The dual-detector, neutron porosity tools with ratio method used on the studied wells logging were first produced to reduce environmental effects on the measurement, but it is still necessary to apply corrections for certain borehole conditions (Galford et al., 1988). The logs need corrections for formation temperature, formation pressure, borehole salinity and mud weight.

For the studied wells, the raw near and far neutron count rate curves were used for corrections. The input parameters also include mud temperature curve, borehole salinity and borehole pressure.

The borehole pressure was calculated using mud weight and measured depth as replacement of the true vertical depth (TVD), and the borehole size was corrected by the service company during the logging.

Figure 3.5 shows an example of an uncorrected neutron log (red) and environmentally corrected log (blue) for E-OA1 borehole.

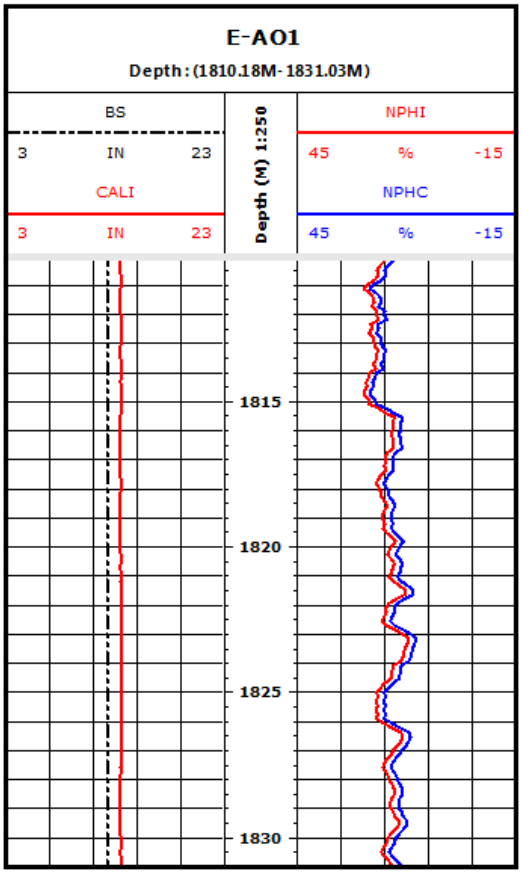

Figure 3.5: Graphics of uncorrected and corrected neutron logs.

3.2.2.3 Density (RHOB)

The density log is run eccentered with a pad bushing against the borehole wall. It is therefore affected by the rough borehole wall. Generally, the environmental effects that can influence the density tools are few in number, and the corrections are of very small magnitude (Ellis and Singer, 2008).

In the current study, the density logs have been corrected to the hole size and mud weight, Figure 3.6 is an example of an uncorrected density log (red) and environmentally corrected log (blue) for E-BB1 borehole.

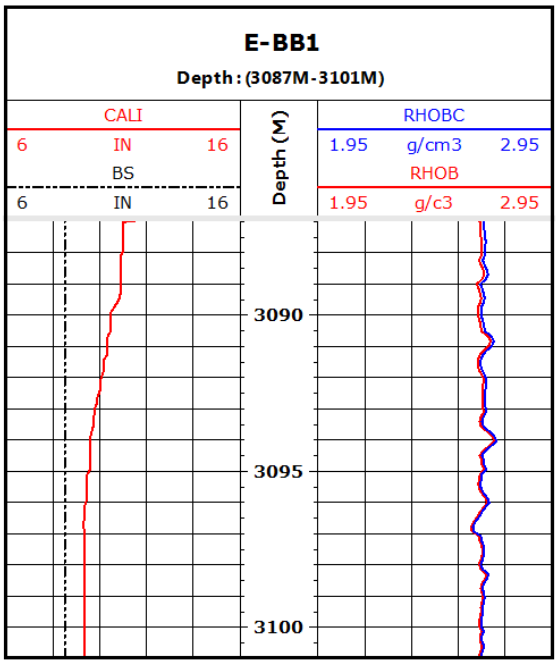

Figure 3.6: Graphics of uncorrected and corrected density logs.

3.2.2.4 Deep Resistivity (LLD/ILD)

To achieve accurate saturation results several environmental corrections must be done to resistivity tools. The tools measurements are sensitive to the borehole, and the applied corrections include hole size and mud resistivity. Mud resistivity at any point along the borehole is calculated using the mud sample resistivity and temperature from the LAS files header and the temperature logs.

Figure 3.7 shows an example of an uncorrected resistivity log (red) and environmentally corrected log (blue) for E-BB1 borehole.

3.2.3 Log Normalization

Normalization is statistical analysis aim to minimize the differences in log measurements caused by logging errors. Differences in log responses to identical formation conditions may be caused by numbers of factors including; inaccurate tool calibration, differences in tool types and when environmental corrections did not exactly match the actual logging conditions (Cluff and Cluff, 2004). The normalization procedure to compensate all logs of a particular type for these conditions involves using representative lithological zones in each well so that they have similar characteristics over the selected intervals.

The selection of such lithological zones to use as reference for normalization is crucial; it is difficult to find zones that have similar rock properties throughout an area or field. In

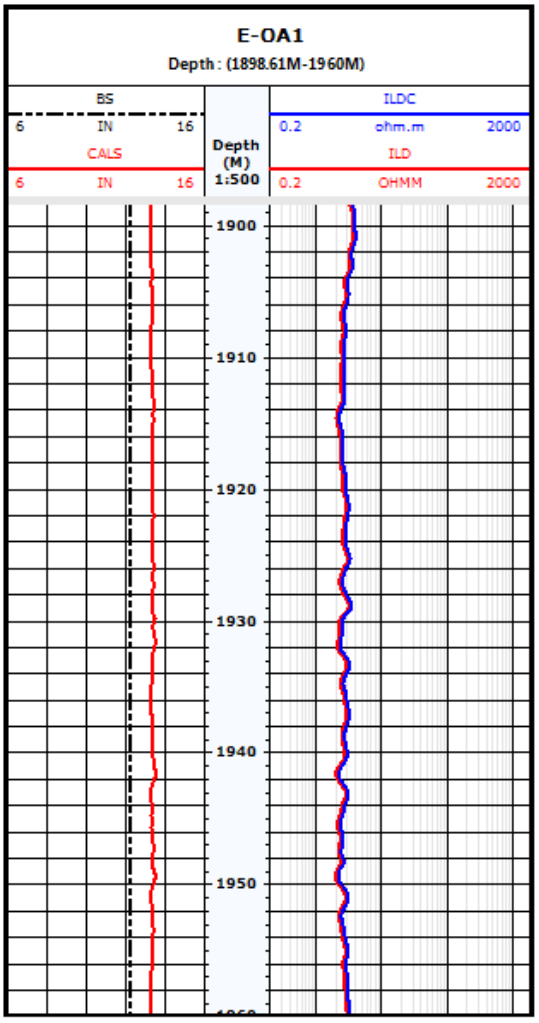

Figure 3.7: Graphics of uncorrected and corrected resistivity logs.

this project, since the studied wells have logged with the same service company and same tools, and since the environmental corrections have been done carefully; no normalization procedure was done. However, to identify facies from well logs which for qualitative analysis, normalization has been performed to the logs involved in the procedure.

3.2.4 Curve Splicing

After performing the corrections, for any particular log type, the different runs logged in the same borehole were spliced together into a continuous log.

3.3 Core Data

The core data consists of conventional core analysis and lithological description reports. Only two of the five studied wells had core data available for this study, E-BB1 and E-AO1. The total thickness of the sedimentary sections recovered from wells E-BB1 and E-AO1 were 15.1m and 8.9 m respectively.

3.3.1 Well E-BB1

Eight cores were cut in this borehole two, within the interval of interest (sequences 13A and 14A), were available for this study. Table 3.1 indicates the cored intervals of well E-BB1.

Table 3.1: E-BB1 Cored Intervals within 13A and 14A sequences.

core	Cored Interval (m)		Cut (m)	Recovery (%)	Recovered (m)	Sequence
	Top	Bottom				
5	2846.0	2864.0	18	58	10.44	13A
6	2872.0	2877.0	5	92.6	4.63	13A

3.3.2 Well E-AO1

Six cores were cut in this borehole, one of them within the interval of interest (sequences 13A and 14A). The table below shows the cored intervals of well E-AO1.

Table 3.2: E-AO1 Cored Intervals within 13A and 14A sequences.

core	Cored Interval (m)		Cut (m)	Recovery (%)	Recovered (m)	Sequence
	Top	Bottom				
1	2674	2683.25	9.25	96.75	8.9	13A

3.3.3 Conventional Core Analysis

The available conventional core analysis measurements include: porosity (%), liquid and air permeabilities (mD), fluid saturations (%) and grain density (g/cc). For E-AO1 the core data also included the overburden measurements of porosity and permeability. The provided core measurements were digitalized and entered into a spreadsheet database for processing. The raw conventional core analysis measurements for E-BB1 and E-AO1 is given in Appendix A and B.

Overburden corrections were applied to E-BB1 core data to simulate in situ reservoir conditions by making use of the provided E-AO1 overburden porosities and permeabilities. Figure 3.8 presents the relationship between the uncorrected and corrected porosities for E-AO1. The empirical linear relationship is given by the regression equation:

$$\Phi_{\text{corrected}} = 0.9905385 * \Phi_{\text{uncorrected}} - 0.5127908 \tag{3.2}$$

where:
$\Phi_{\text{corrected}}$ is the core porosity at overburden pressure.
$\Phi_{\text{uncorrected}}$ is the core porosity at room condition.

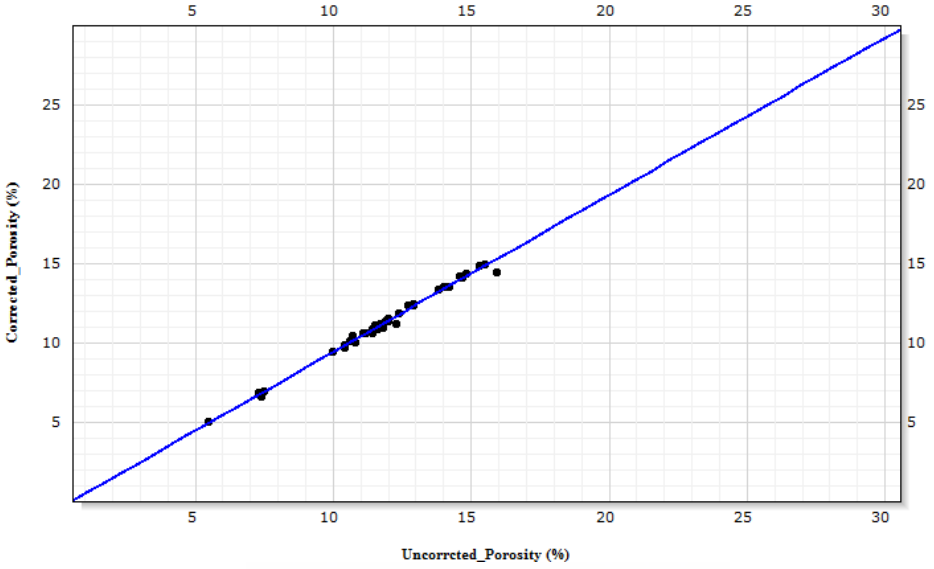

Figure 3.8: Uncorrected core porosity and corrected core porosity relationship for E-AO1.

The same procedure has been done for permeability corrections (Figure 3.9). The regression equation is:

$$\log10(\text{K}_{\text{corrected}}) = 1.098863 * \log10(\text{K}_{\text{uncorrected}}) - 0.1403815 \tag{3.3}$$

where:
$\text{K}_{\text{corrected}}$ is the core permeability at room condition.
$\text{K}_{\text{uncorrected}}$ is the core permeability at overburden pressure.

These two equations have been used to correct the porosity and permeability values for the other cored well E-BB1, the corrected values are given in Appendix C.

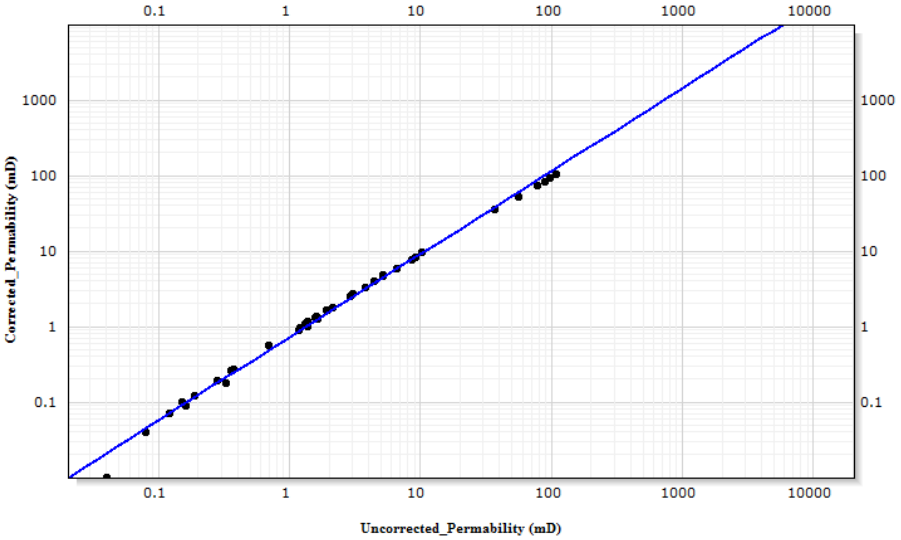

Figure 3.9: Uncorrected core permeability and corrected core permeability relationship for E-AO1.

3.4 Core-Log Depth Matching

Wireline logging and coring are two different processes. Logs are identified by Wireline depths; core by driller depths and the measurements are carried out by different service provider at different times. This implies differences between the two measured depths. Therefore, the core depth should be depth matched to the wireline depth (Worthington, 1991).

In this study, a correction based on correlation between gamma ray log and a reference shale point has been done. The conventional core analysis results have been compared to the log data by overlaying core measured data and wireline logs data, core depths have been shifted to match the wireline depths

The table below shows the required shift in each cored interval to match the log data.

Table 3.3: Core-log depth shift for E-BB1 and E-AO1 wells.

Well	Core	Cored Interval (m)		Corrected Interval (m)		Shift
		Top	Bottom	Top	Bottom	
E-BB1	5	2846	2864	2848	2866	2
E-BB1	6	2872	2877	2874.5	2879.5	2.5
E-AO1	1	2674	2683.25	2674.3	2683.55	0.3

Chapter 4

Facies, Sequence Boundaries and Reservoir Zones

4.1 Introduction

In exploration and production of hydrocarbon from sedimentary basins the full understanding of the properties of subsurface strata is essential. For better evaluation of hydrocarbon reservoirs, facies are of great importance. This importance rests upon their control of the variation of petrophysical properties and subsurface fluid flow (Yumei, 2006).

Facie refers to a body of rocks with unique lithological, physical, and biological attributes relative to all adjacent deposits (Octavian, 2006) . It reflects the physical, chemical and biological conditions and processes of the depositional environment.

The core data provided the basis on which sedimentologic observation and interpretation are established because reservoir properties are directly measured on core samples. It is normally the most reliable petrophysical data.

4.2 Facies from Core

Within the studied wells, the central Bredasdorp Basin has only three cores through the interval stratigraphy of 13A and 14A sequences available for this study. The sedimentological descriptions which were carried out by SOEKOR were used to determine facies distribution based on nearly 24m of the available cores. The facies have been classified based on grain size, textures, primary and secondary sedimentary structures.

Four distinct facies types have been distinguished in the studied wells. These facies were alphabetically designated, A through D, and are discussed further in this chapter.

4.2.1 Massive sandstone (A)

Clean massive sandstone characterised by very fine to medium grained, well sorted sands. No grading of the grain size can be detected. The sandstones are generally massive with rare sedimentary structure such as ripple stratification. This facies occurs in core 5 in E-BB1 from depth 2847.2m to 2857.5m (logger depth) and from 2872.2m to 2872.6m as presented in figure 4.1. This facies is interpreted to be the basal part of channel-fill sandstone deposited on a submarine fan in an inner fan to middle fan setting.

4.2.2 Shaly Sandstone (B)

This facies is also massive sandstone, but it is characterised by occasionally thin claystone interbeds. These claystones do not exceed 5cm and have sharp tops. The sandstone is very argillaceous, light to dark grey, fine to very fine grained with abundant claystone clasts. The sandstone individual beds vary in thickness from 0.2m to 1.3m or even more. This facies occurs in core 1 in E-AO1 from depth 2674.3m to 2681.3m as shown in figure 4.2.

4.2.3 Interbedded sandstone, siltstone and claystone (C)

The claystone in this facies is massive, dark grey to black and interbedded in millimetre to centimetre scale with argillaceous sandstone and siltstone. Carbonaceous materials are present in minor amounts. The interbedded sandstones are generally massive with sharp upper contacts. This facies occurs in core 1 in E-AO1 from depth 2681.4m to 2683.5m and in core 6 in E-BB1 from 2872.7m to 2874m as presented in figures 4.1 and 4.2 respectively.

4.2.4 Massive Claystone (D)

This facies is characterised by greyish black to dark grey claystone. The claystone is generally homogenous with occasionally very thin siltstone laminae of millimetre scale. This facies occurs in core 6 in E-BB1 from depth 2874.3m to 2976.9m as shown in figure 4.1.

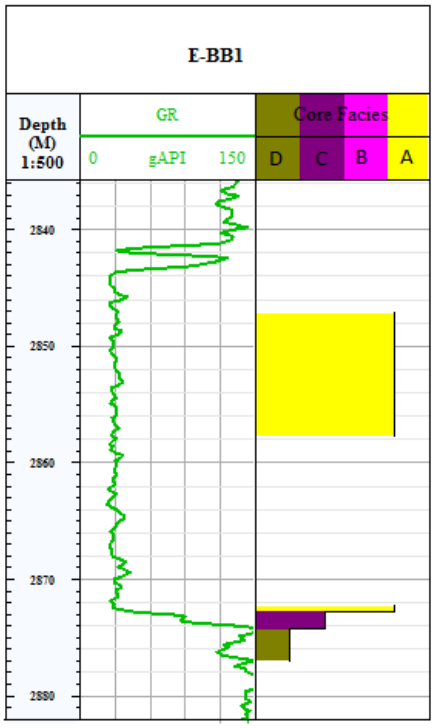

Figure 4.1: Core facies and gamma ray log in E-BB1 over a depth interval of about 2836m to 2882m.

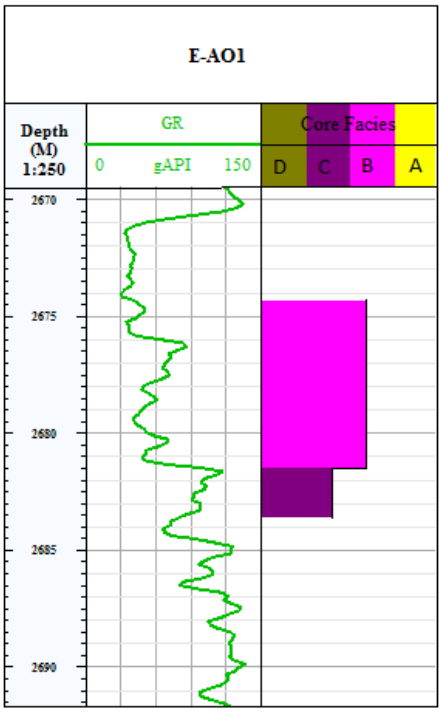

Figure 4.2: Core facies and gamma ray log in E-AO1 over a depth interval of about 2669m to 2692m.

4.3 Facies from Wireline Logs

Since facies can not be observed directly from wireline logs and the interpretation from core measurements is limited to the cored intervals of the wells; a method is needed to propagated facies to the uncored intervals or wells in the studied reservoir using wireline logs. The need of such method increases offshore where extra costs limit the acquisition of cores.

The basic idea of any proposed method to identify facies from wireline logs for a given formation is to make correlation between the behaviour of wireline logs and the lithological facies of this penetrated formation. However, facies prediction from wireline logs is challenge and is subject to great uncertainty.

Several methods have been used to overcome the problems associated with facies prediction from wireline logs. Early approaches applied cut-offs on wireline logs, such as GR in clastic lithology, to derive the facies (Zee Ma, 2011) . Modern theoretical methods involve two main classification approaches; statistical methods and artificial intelligence techniques.

Artificial neural network (ANN) is a popular intelligent system for solving non-linear complex problems. This system has been recently used to approach the problem of identifying lithological facies from well logs by clustering the input data to get representative sets of nodes. Then the system assigns facies to each node based on indexation input (Qi and Carr, 2006; Tang and White, 2008). The purpose of clustering wireline data is to classify the data into several sets that are internally similar and externally different on the basis of a measure of petrophysical similarity or dissimilarity between sets.

Facies prediction can be carried out in one of three indexation methods; supervised, semi-supervised, and unsupervised. In the supervised method, ANN learns the relationships between petrophysical properties and a pre-existing classification such as a geological facies interpretation. Once a model linking properties and facies has been learned, ANN applies this model and creates a geological facies prediction for the other wells.

4.3.1 Method of Facies Prediction

In this study, the facies prediction method is based on the neural network technology. The Ipsom module in Techlog software provides solution to identify facies from wireline logs with both supervised and unsupervised methods. The supervised method is applied by making use of the facies identified from E-BB1 and E-AO1 cores in the previous sections as indexation set. The advantage of using the supervised method is to combine

core description and wireline logs together since information about the sediments from wireline logs may not be sufficient alone (Gluyas and Swarbick, 2004) .

The gamma ray logs (GR), neutron porosity logs (NPHI), bulk density logs (RHOB), deep resistivity logs (ILD/LLD), compressional slowness logs (DT) and photoelectric factor (PEF) were used as lithology logs according to (Rider, 1996), Gifford2010 used the same combination of logs among others to create rock facies sequences from wireline logs data.

The core identified facies and the input logs in the two key wells are displayed together in figures 4.4 and 4.4 . To minimize the shoulder effects associated with facies boundaries; the logs values above and under theses boundaries have been flagged and removed from the analysis.

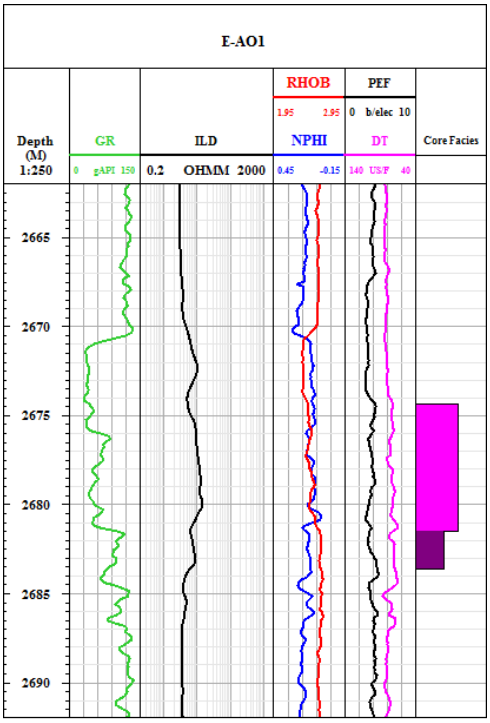

Figure 4.3: Input well logs GR, ILD, DT, NPHI, PEF, RHOB and core facies in E-AO1 over a depth interval of about 2662mto 2692m.

4.3.2 Results

After the indexation procedure was done to the zones correspond to the core facies in E-AO1 and E-BB1, the resultant computation model was applied for all the studied wells in order to create classification curves. For each input log, automatic normalization has been done. Table 4.1 below presents the multi-well normalized minimum and maximum values for each log.

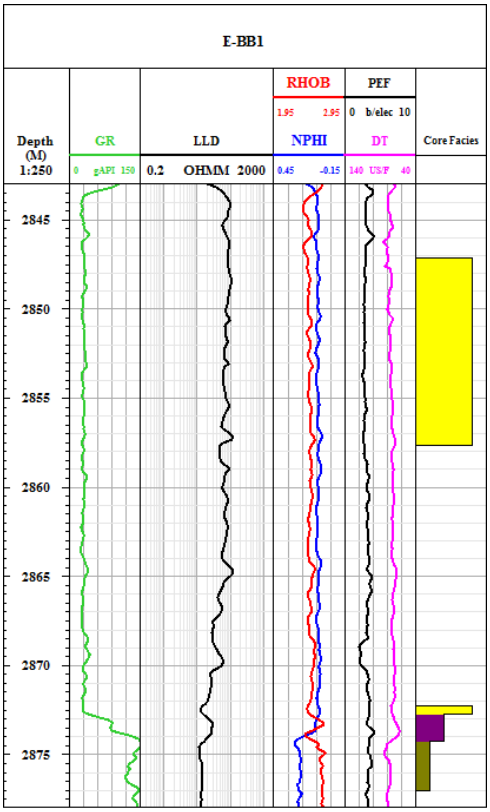

Figure 4.4: Input well logs GR, LLD, DT, NPHI, PEF, RHOB and core facies in E-BB1 over a depth interval of about 2843m to 2878m

Table 4.1: Normalized minimum and maximum values for input logs of the studied wells.

No	Input Log	Norm Min	Norm Max
1	RHOB	2.3966	2.6749
2	DT	63.07897	84.59282
3	ILD/LLD	5.085661	118.9951
4	GR	25.08148	140.9196
5	NPHI	0.044	0.2558
6	PEF	2.4648	4.499944

The statistic of each predicted facies is presented in table 4.2 . The number of samples is number of nodes associated to each facies.

Table 4.2: The statistic of predicted facies

Facies	A	B	C	D
Number of samples	45	43	20	13
Input logs	Mean	Mean	Mean	Mean
RHOB	2.4525	2.4647	2.5762	2.6270
DT	75.2941	74.1921	70.0478	77.1723
ILD/LLD	100.6652	32.5710	37.3077	38.9444
GR	30.9245	57.2024	93.5592	125.7785
NPHI	0.0783	0.1258	0.1428	0.2224
PEF	2.7670	3.7512	3.7841	3.4404

Table 4.3 below indicates the correlation between each input log and the output classification curve. Values close to zero will show that there is no correlation between the input log and the predicted facies. However, if the values are close to one, this means that the log is highly correlated with the facies. The information column shows the contribution of each input log in the facies classification.

The gamma ray and deep resistivity logs have the best correlation and therefore they have a bigger contribution in facies prediction classification. The sonic log has the lowest contribution due to its lower correlation factor.

Table 4.3: The correlation factor and the contribution of each input log.

No	Input log	Correlation	Information
1	GR	0.9331993	0.2030094
2	ILD/LLD	0.8803161	0.1915051
3	NPHI	0.8387994	0.1824735
4	RHOB	0.7991649	0.1738513
5	PEF	0.7177526	0.1561408
6	DT	0.427597	0.09301998

The calculated wireline facies were then compared with core identified facies for validation. The purpose of this comparison was to see if the results derived from wireline logs could be applied to other levels of the well, i.e. levels that did not have core data, and to the other wells without core data.

Figures 4.5 and 4.6 present the correlation between core facies and wireline facies in E-AO1 and E-BB1 respectively. The figures show that the wireline derived facies are in good match with core facies.

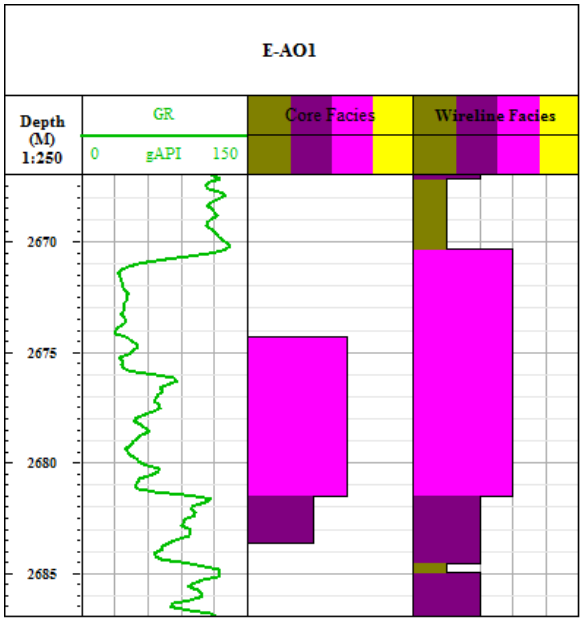

Figure 4.5: Correlation between core facies and wireline facies in E-AO1.

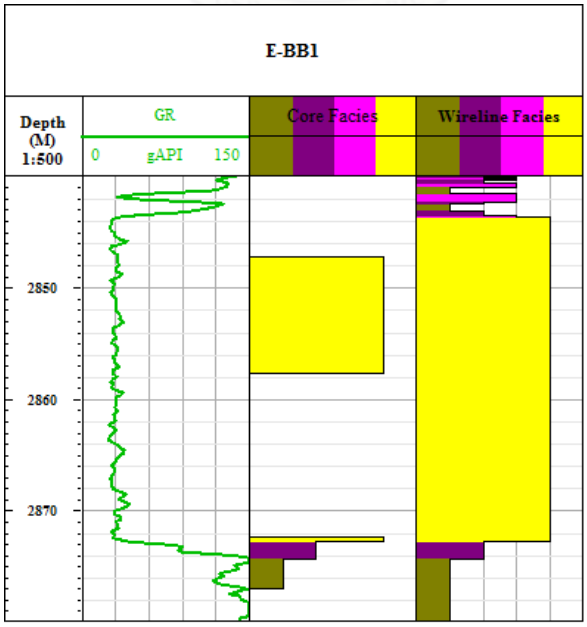

Figure 4.6: Correlation between core facies and wireline facies in E-BB1.

4.4 Sequences Boundaries

Depositional sequence is defined as a relative conformable succession of genetically related strata bounded by unconformities or their correlative conformities (Mitchum et al., 1977) . Every depositional sequence is a record of one cycle of relative sea level and it can be subdivided into number of system tracts. The system tract is genetically associated stratigraphic units that were deposited during specific phases of the relative sea-level cycle. Each system tract is a stratal stacking pattern of a particular genetic type of deposit, transgressive, normal regressive and forced regressive. (Catuneanu et al., 2009).

(Schlager, 1999), defined the sequence boundary as bounding surface of conformably stratified units. Accordingly, sequence boundary is an unconformity that characterises the base of a sequence. This unconformity is normally formed due to the sea level fall, so in wireline logs it is commonly marked by an abrupt increase in gamma ray response below thick sandstones intervals.

In this project, the stratigraphic surfaces 13At1 and 14At1 were identified from wireline logs. The gamma ray, sonic and deep resistivity logs were used for this determination. The proposed surfaces are presented in table 4.4 below, whereas figure 4.7 shows the correlation between these stratigraphic surfaces for the studied wells. The correlation cross-section is orientated SE-NW as shown on the inset map in the figure.

Table 4.4: Sequences boundaries in the investigated wells.

wells	14At1	13At1
E-AD1	2570.28m	2838.72m
E-AO1	2632.92m	2915.65m
E-AO2	2627.34m	2928.46m
E-BB1	N/A	2872.89m
E-BB2	2585.25m	2877.60m

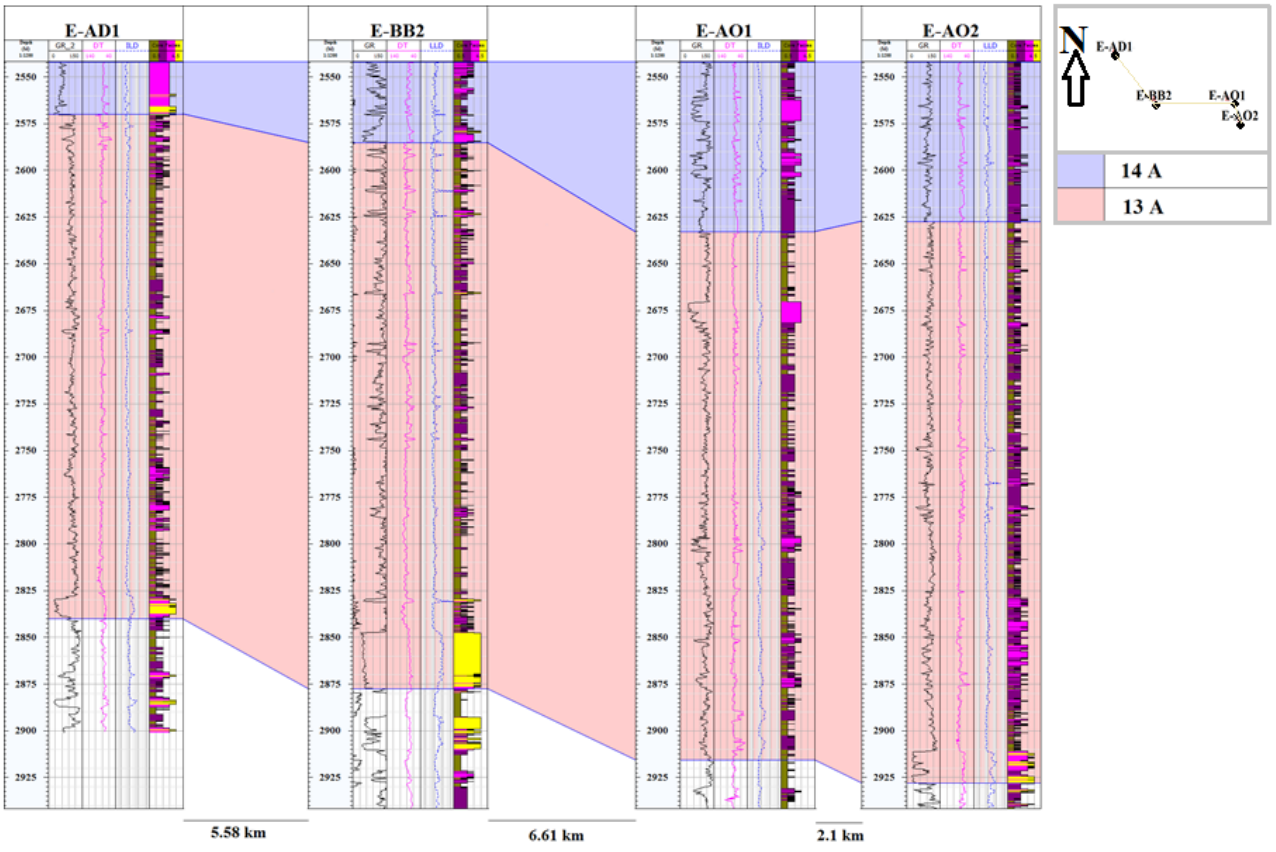

Figure 4.7: The correlation between sequences boundaries of 13A and 14A units.

4.5 Reservoir Zones Identification

From the previous facies identification; reservoir zones were recognised in the studied wells. Facies A and B are considered to be reservoir zones. They are discussed further in this chapter.

4.5.1 E-AD1 Reservoir Zones

Within the studied interval through 13A and 14A sequences, three reservoir zones were identified in E-AD1.
Zone one ranges from 2497.57m to 2527.81m in 14A the sequence has a thickness of 30.02m as presented in figure 4.8 below. This zone consists of clean sand (facies A) and shaly sand (facies B). The presence of facies D directly above this reservoir zone with average gamma ray reading of 110 API indicate a good cap rock for hydrocarbon trapping.

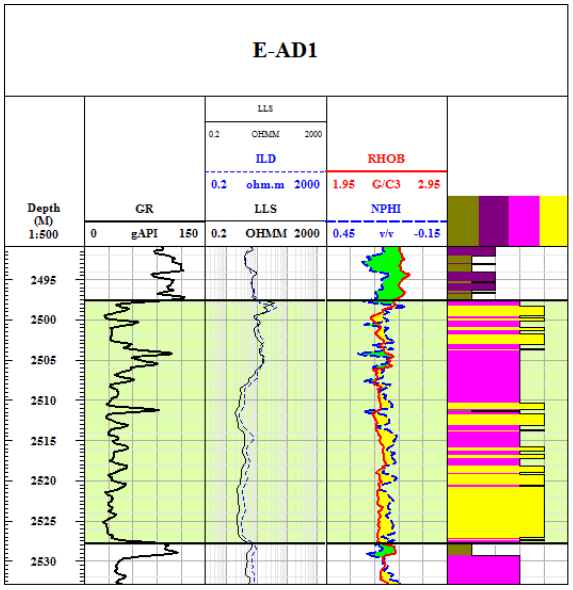

Figure 4.8: Reservoir zone one in E-AD1.

Zone two underlies zone one, both separated by non-reservoir formation. The range of this zone is from 2529.56m to 2570.28m just above 14At1 sequence boundary having thickness of 40.72m as presented in Figure 4.9 below. This zone is predominately shaly (facies B) with occasionally clean sand.

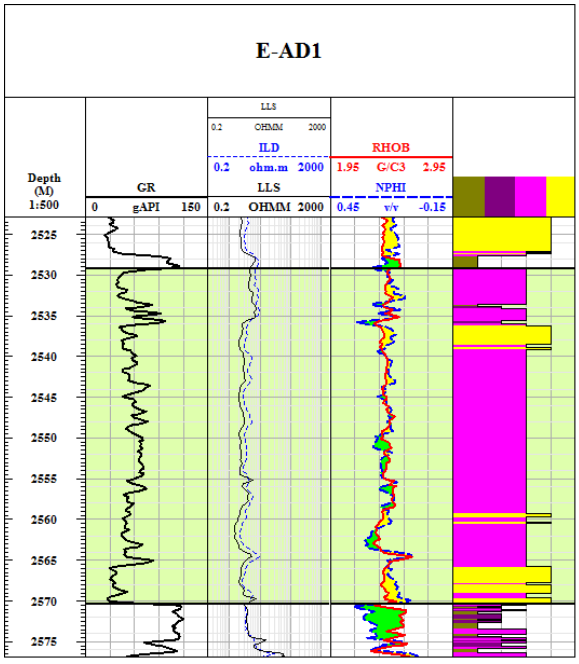

Figure 4.9: Reservoir zone two in E-AD1.

Zone three is mainly clean sand. This zone is just above 13At sequence boundary ranging from 2827.78m to 2838.72m with a thickness of 9.24m as presented in figure 4.10 below. This zone is predominately clean sand (facies A) with occasionally shaly sand (facies B) in the top and bottom of the zone.

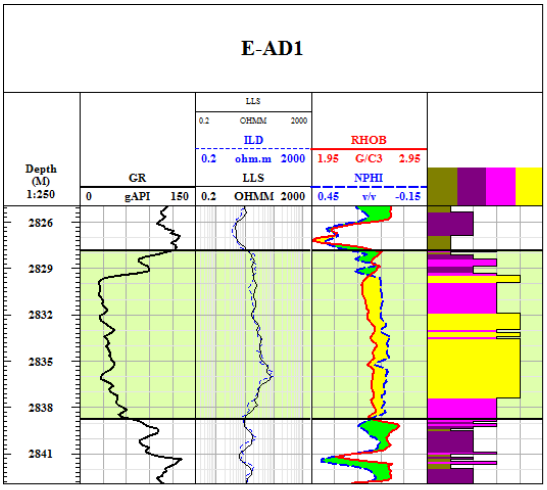

Figure 4.10: Reservoir three one in E-AD1.

4.5.2 E-AO1 Reservoir Zones

Within the studied interval through 13A and 14A sequences, four reservoir zones were identified in E-AO1.

Zone one ranges from 2560.71m to 2573.4m in 14A the sequence has a thickness of 12.69m as presented in figure 4.11 below. This zone completely consists of shaly sand (facies B).

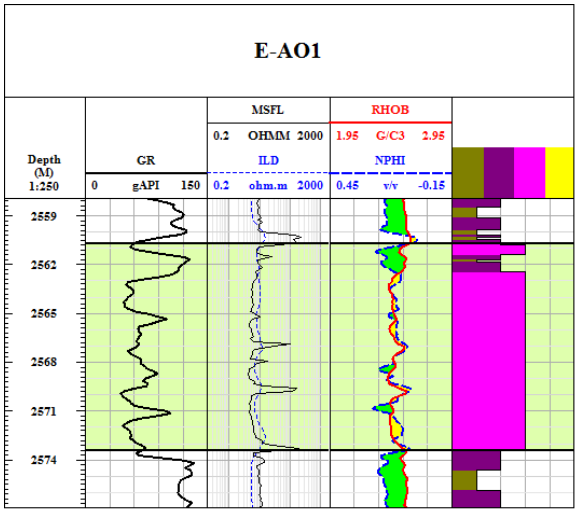

Figure 4.11: Reservoir zone one in E-AO1.

Zone two ranges from 2590.77m to 2603.30m in 14A with the sequence having a thickness of 12.53m as presented in figure 4.12 below. This zone also consists of shaly sand (facies B).

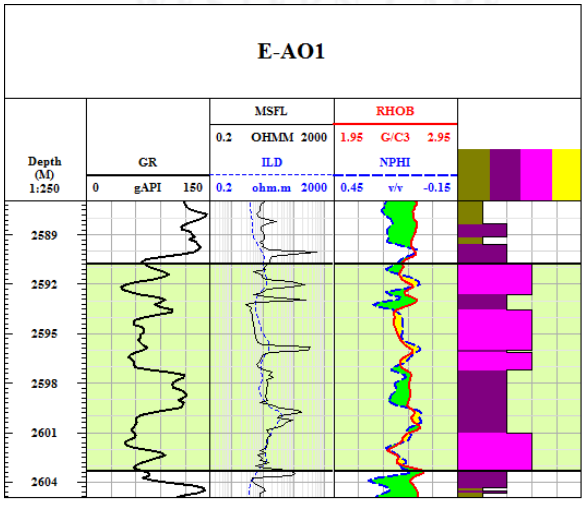

Figure 4.12: Reservoir zone two in E-AO1.

Zone three ranges from 2670.40m to 2681.56m in 13A the sequence has a thickness of 11.16m as presented in figure 4.13 below. This zone also consists of shaly sand (facies B).

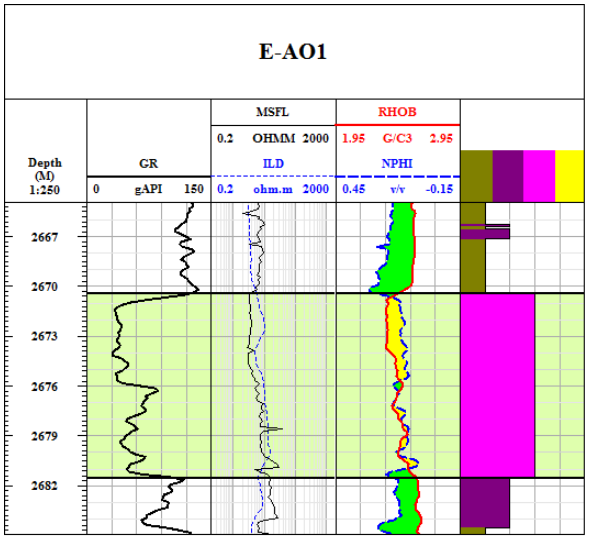

Figure 4.13: Reservoir zone three in E-AO1.

Zone four ranges from 2796.90m to 2803.73m in 13A with the sequence having a thickness of 6.83m as presented in figure 4.14 below. This zone also consists of shaly sand (facies B).

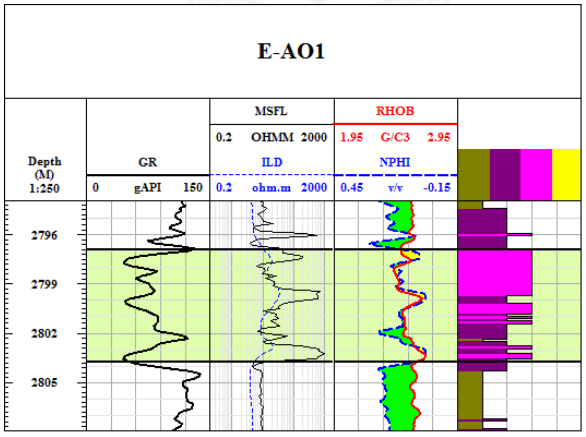

Figure 4.14: Reservoir zone four in E-AO1.

4.5.3 E-AO2 Reservoir Zones

Within the studied interval through 13A and 14A sequences, two reservoir zones were identified in E-AO2.

Zone one ranges from 2911.00m to 2921.30m in 13A the sequence hasa thickness of 10.30 as presented in figure 4.15 below. This zone consists of shaly sand (facies B) and clean sand (facies A).

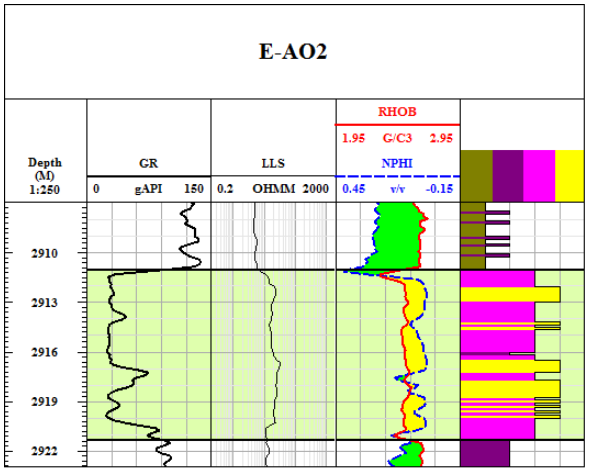

Figure 4.15: Reservoir zone one in E-AO2.

Zone two ranges from 2923.64m to 2928.46m just above 13A the sequence boundary has a thickness of 4.82m as shown in figure 4.16 below. This zone is almost clean sand (facies A).

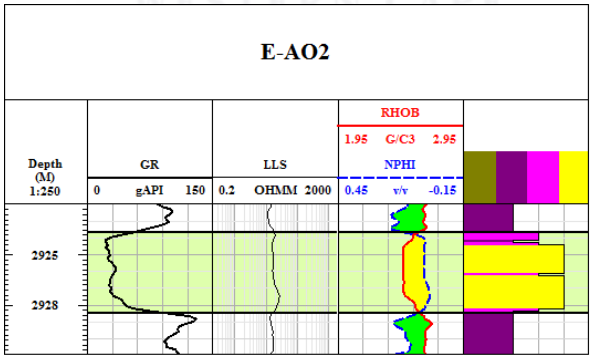

Figure 4.16: Reservoir zone two in E-AO2.

4.5.4 E-BB1 Reservoir Zones

Within the studied interval through 13A and 14A sequences, one reservoir zone was identified in E-BB1.

This zone ranges from 2843.70m to 2872.89m just above 13At with thesequence boundary having a thickness of 29.19m as presented in figure 4.17 below. This zone consists of clean sand (facies A).

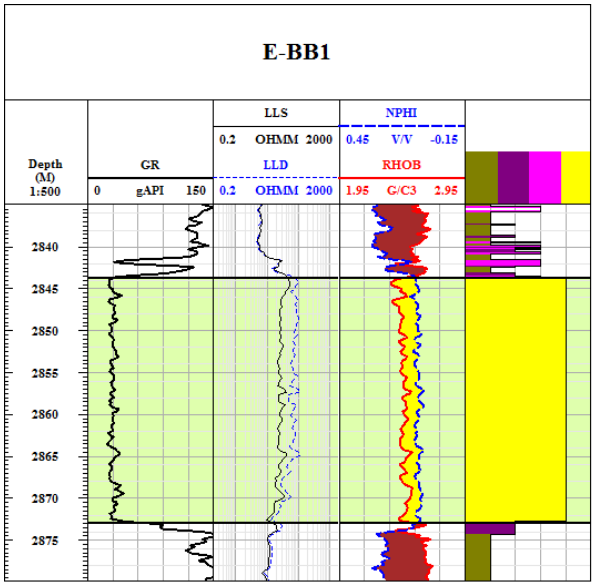

Figure 4.17: Reservoir zone one in E-BB1.

4.5.5 E-BB2 Reservoir Zones

Within the studied interval through 13A and 14A sequences, three reservoir zones were identified in E-BB2.

Zone one ranges from 2539.31m to 2550.59m in 14A with the sequence having a thickness of 11.28m as indicated in the figure below. This zone consists of shaly sand (facies B).

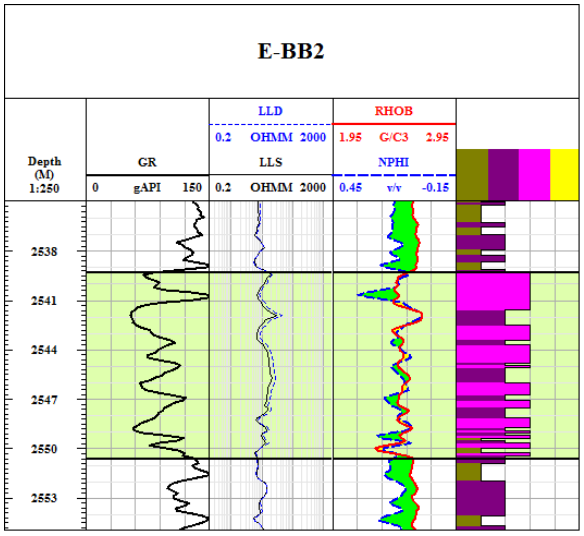

Figure 4.18: Reservoir zone one in E-BB2.

Figure 4.19 indicates that zone two ranges from 2577.43m to 2585.25m just above 14At the sequence boundary has a thickness of 7.82m . This zone consists of shaly sand (facies B).

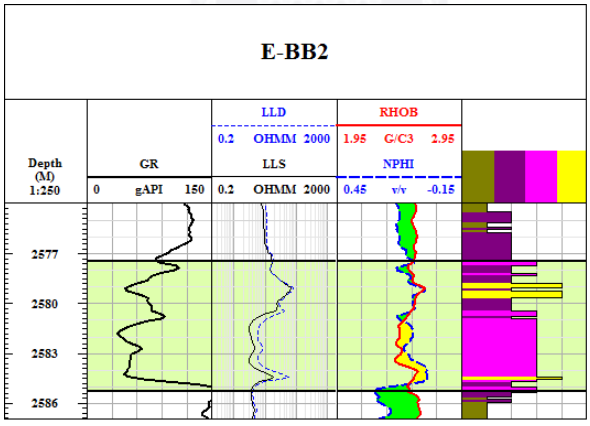

Figure 4.19: Reservoir zone two in E-BB2.

Figure 4.20 shows that zone three ranges from 2847.42m to 2877.60m just above 13At th sequence boundary has a thickness of 30.18m. This zone consists of clean sand (facies A).

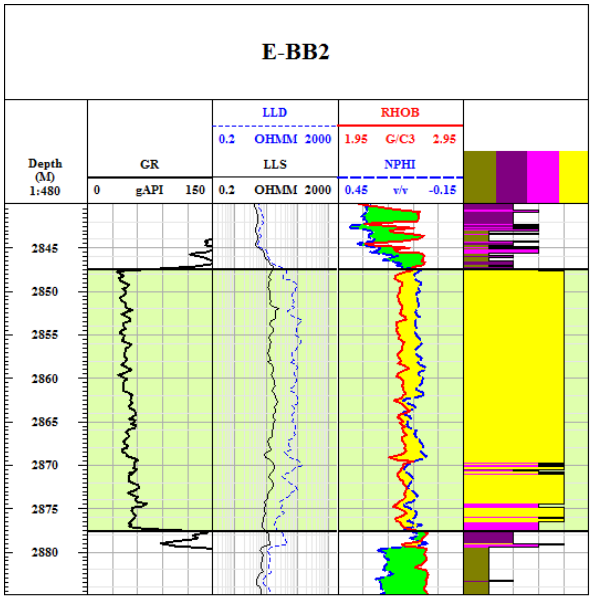

Figure 4.20: Reservoir zone three in E-BB2.

Chapter 5

Petrophysical Model

This chapter presents a fully integrated petrophysical model of the predefined reservoirs zones. This model includes determinations of: volume of shale, porosity, water saturation and permeability. Deterministic methods were used to obtain these petrophysical parameters from wireline logs using Techlog software. The core data was used to calibrate the petrophysical model to get the most reliable values.

5.1 Volume of Shale Determinations

The volume of shale (V_{sh}) is the bulk volume fraction of shale, or the volume of shale per unit volume of reservoir rock, and it is expressed in decimal fraction or percentage. The presence of shale in sand formations (shaly sand) affects logging tool responses, and reduces the accuracy of porosity and water saturation values. Therefore, the accurate determination of the volume of shale present in the pay intervals is an essential procedure in the reservoir evaluation process.

Usually, the shale volume (V_{sh}) is calculated using different methods. These include single curve indicators such as; gamma ray and resistivity responses, and double curve indicators (Neutron/Density, Neutron/Sonic, Density/sonic). In the absence of laboratory analysis and X-ray diffraction to calibrate these methods, one must rely on accurate model that consider the complexity of the studied reservoir.

In gas bearing reservoirs, the use of a porosity log as shale indicators is not applicable (4). Gas saturation within the depth of investigation of porosity tools causes a decrease in density log and an increase in neutron log. As a resul, where the size of the separation between neutron and density logs is the one of the common quantitative estimators of shale volume; the calculated shale volumes will be too low (Kamel. and Mabrouk., 2003; Adeoti

et al., 2009). Also, the presence of gas in poorly compacted sand results in considerable increase in sonic log (Bassiouni, 1994).

In this study shale volume (V_{sh}) has been calculated using resistivity and gamma ray responses. The detailed method in (Soto et al., 2010) to calculate the shale volume from gamma ray without Uranium effect is adopted in this work.

5.1.1 Resistivity Shale Volume

The use of the deep resistivity log as a shale indicator depends upon the contrast of the resistivity response in shale and in a clean sand. Resistivity decreases with higher shale volume. The method calculates the volume of shale using resistivity logs from the following relationship:

$$V_{sh} = \frac{\log R_t - \log R_{ma}}{\log R_{sh} - \log R_{ma}} \tag{5.1}$$

where:
R_t : True resistivity (Resistivity log reading in zone of interest).
R_{sh} : Resistivity log reading in 100% shale.
R_{ma} : Resistivity log reading in 100% matrix rock.

For all the studied wells, the values of shale resistivities (R_{sh}) were selected against the nearby shale, while values of matrix resistivities were measured against the most clean sand. The results are presented in table 5.1.

5.1.2 Gamma Ray Shale Volume

The direct relationship between the gamma ray response and the shaliness of the formation makes the gamma ray method one of the most common volume of shale indicators in the evaluation of shaly sand. The tools measure the radioactivity of the formation minerals, and these in most cases are clay minerals. The procedure of the method is to use the relative gamma ray deflection between minimum response (clean sand) and maximum response (pure clay) as a shale indicator.

The volume of shale can be calculated from gamma ray by using linear methods. The gamma ray index (I_{GR}) is calculated from the following relationship:

$$I_{GR} = \frac{GR_{log} - GR_{min}}{GR_{max} - GR_{min}} \tag{5.2}$$

where:
I_{GR} : gamma ray index
GR_{log} : gamma ray log reading in zone of interest
GR_{min} : gamma ray log reading in 100% clean zone
GR_{max} : gamma ray log reading in 100% shale

For all the studied wells, the minimum and maximum gamma ray log readings were selected, the results are indicated in table 5.1.

5.1.3 Computed Gamma Ray Volume of Shale

The gamma ray log is a sum of three radioactive elements; uranium (U), thorium (Th) and potassium (K). Generally, the largest source of formation radioactivity is potassium, where uranium and thorium are rare. In clay minerals particularly, potassium and thorium have large concentration comparing with the negligible amount of uranium. The significant concentrations of uranium is only associated with the organic material in the shales rather than the clay minerals (Ellis and Singer, 2008). As a result when calculating shale volume, the presence of uranium in source rock formation increases the total gamma ray values, which result in a high gamma ray at 100% shale zone.

The computed gamma ray log (CGR) is sum of potassium and thorium responses, without uranium response, and it is used in this study to calculate the shale volume. The log was only run in well E-AD1. For the other four wells, the total gamma ray logs (GR) have been normalized using the available CGR log as reference. The result is presented in figure 5.1 below. The total gamma ray logs are fitted into the distribution of the computed gamma ray log (the brown colour).

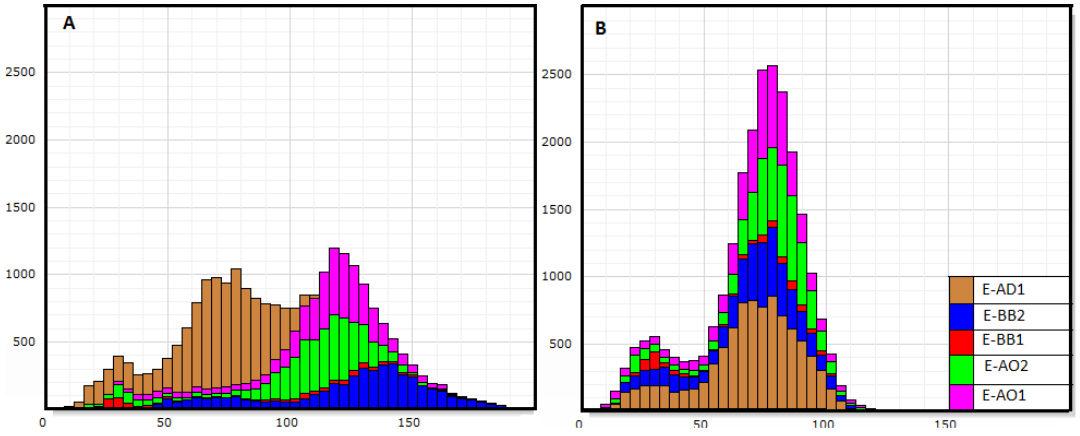

Figure 5.1: (A) The GR logs of the four wells before normalization together with CGR from E-AD1, (B) The same logs after normalization.

For all the studied wells, the relationship (5.1) has been used and the minimum and maximum computed gamma ray log readings are selected, the results are presented in table 5.1 below.

Table 5.1: The minimum and maximum values of gamma ray logs (GR), computed gamma ray logs (CGR) and resistivity logs (ILD/LLD) used in shale volume calculations.

well		E-AD1	E-AO1	E-AO2	E-BB1	E-BB2
Resistivity	Min	2.23	2.1	2.5	4.5	3.4
	Max	48.7	56	93.5	100	100
GR	Min	24	30	22	22	33
	Max	141	139	142	145	147
CGR	Min	12	8	5	20	12
	Max	101	97	107	88	98

5.1.4 Correction of Shale Volume

The values of gamma ray index (I_{GR}) obtained above have been corrected by making use of the nonlinear formulas introduced by (Clavier et al., 1971) and (Steiber, 1973). These are empirical formulas developed for different geologic ages and were found to be more reliable.

(Clavier et al., 1971) relationship is:

$$V_{sh} = 1.7 - \sqrt{3.38 - (I_{GR} + 0.7)^2} \tag{5.3}$$

(Steiber, 1973) relationship is:

$$V_{sh} = \frac{I_{GR}}{3 - 2I_{GR}} \tag{5.4}$$

5.1.5 Final Volume of Shale

Figures 5.2 and 5.3 present comparisons between the different methods applied in this study to calculate the volume of shale in E-AO1 and E-BB2 respectively. In the absence of a special core analysis to calibrate these models, the final volume of shale is considered to be the minimum among the models at any point along the well log.

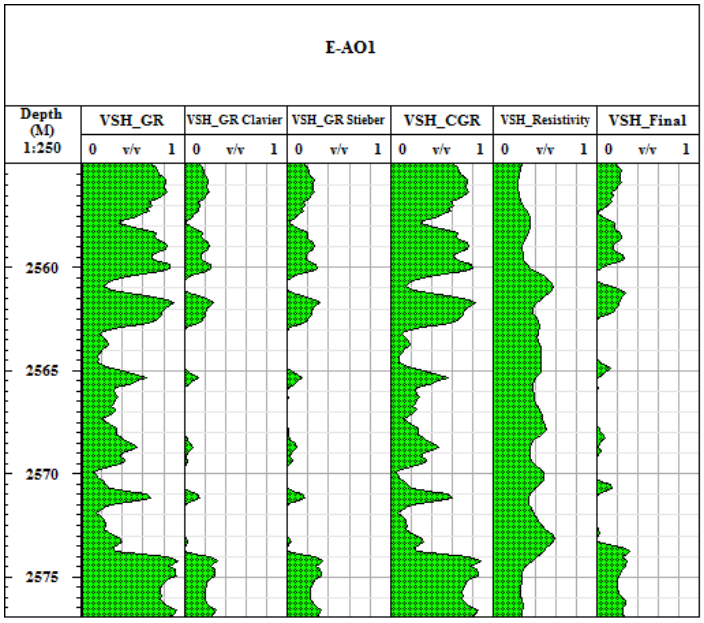

Figure 5.2: Shale volume calculation by using GR, GR Clavier et al, GR Steiber, CGR, resistivity and final volume of shale in E-AO1 from depth 2555m to 2577m.

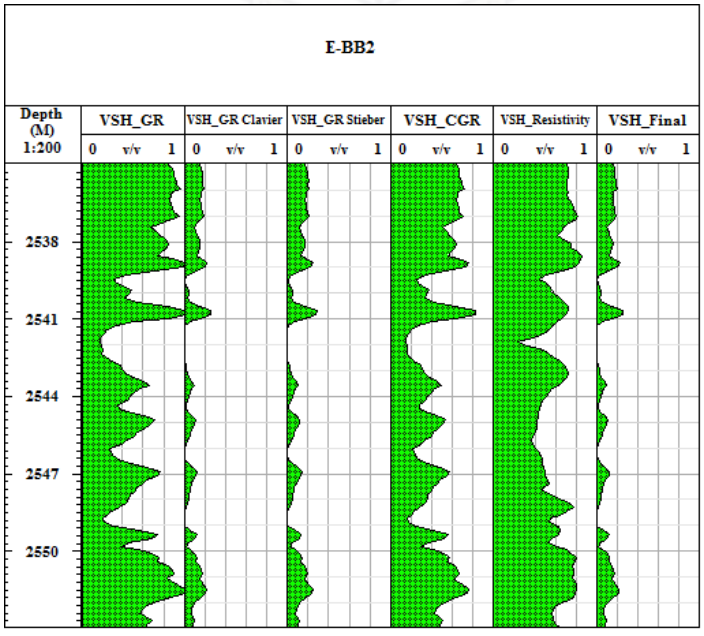

Figure 5.3: Shale volume calculation by using GR, GR Clavier et al, GR Steiber, CGR, resistivity and final volume of shale in E-BB2 from depth 2535m to 2553m.

5.2 Porosity Determinations

Porosity is the most basic and important rock property; it defines the ability of the formation to store fluids. (Selley, 2000) defined the porosity as the ratio of pore space volume, which is not occupied by the solid constituents, to the total volume. It can be expressed either as fraction or percentage and it is mathematically given as:

$$\text{Porosity } (\Phi) = \frac{\text{Volume of the pore spaces}}{\text{Total volume of rock}} \tag{5.5}$$

Porosity has been classified based on the connectivity into total porosity and effective porosity. Total porosity is the ratio of the total volume of the pore space to the total volume of the rock, whereas effective porosity is the ratio of interconnected pore space to the total volume of the rock.

Porosity is also classified based on its geological origin to primary porosity and secondary porosity. Primary porosity is developed during the deposition of the sedimentary material and secondary porosity develops by geological processes after the original deposition. Porosity is normally estimated quantitatively from density, neutron and sonic logs.

5.2.1 Core Porosity

Core plugs from wells E-AO1 and E-BB1 were analysed through volumetric measurements to estimate the porosity of the reservoirs. Porosity measurements obtained from core are considered to be accurate and it is normally used to validate the logs calculated porosity.

The core porosity for the two key wells is distributed between 5% and 15.7% with a mean value of 11.4% as shown in figure 5.4.

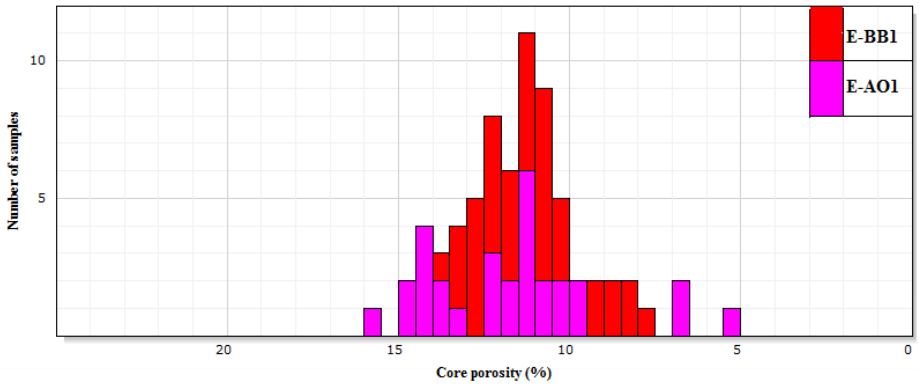

Figure 5.4: E-BB1 and E-AO1 core porosity (%) histogram.

5.2.2 Porosity from Density Log

The density log measures the bulk density of the formation and it used as a primary indicator of the total porosity. The logging technique of the density tools is to emit medium to high gamma rays continuously from special chemical source into the formation. These gamma rays interact with the electrons of the elements in the formation, where they lose some energy until they are either completely absorbed or return with diminished energy to one or the other of the two detectors in the tools. The amount of detected gamma ray is dependent upon the density of formation.

The measured bulk density results from the combined effects of the matrix component of the formation and the fluids occupying the pore spaces (porosity). This relationship is used to calculate porosity from density log, it can be written as:

$$\Phi = \frac{\rho_{\mathrm{ma}} - \rho_{\mathrm{b}}}{\rho_{\mathrm{ma}} - \rho_{\mathrm{f}}} \tag{5.6}$$

where:
Φ : the porosity of the rock.
ρ_{b} : the bulk density of the formation.
ρ_{ma} : the density of the rock matrix.
ρ_{f} : the density of the fluids occupying the porosity.

The relationship 5.11 required input of values for matrix and fluid densities. The accurate knowledge of these values gives trusted estimation of the porosity. The following sections show the methods employed in this study to calculate these two values.

5.2.2.1 Matrix Density

The matrix density is the density of the solid material of the formation without the pore space. In complex lithologies, inadequate determination of the matrix could yield inaccurate porosity. In sandstone the matrix density is normally lies between 2.65 and 2.67 g/cm3. However, to get the actual value representing the grain density of the studied reservoir; the core calculated grains densities are used.

The grain densities of wells E-AO1 and E-BB1 are shown in figure 5.5. The values range from 2.64 to 2.73 g/cm^3 with a mean value of 2.67 g/cm^3. The high values indicate the presence of calcite within the samples obtained from E-AO1. Excluding these values, a mean value of 2.66 g/cm^3 is obtained and will be used in porosity calculations.

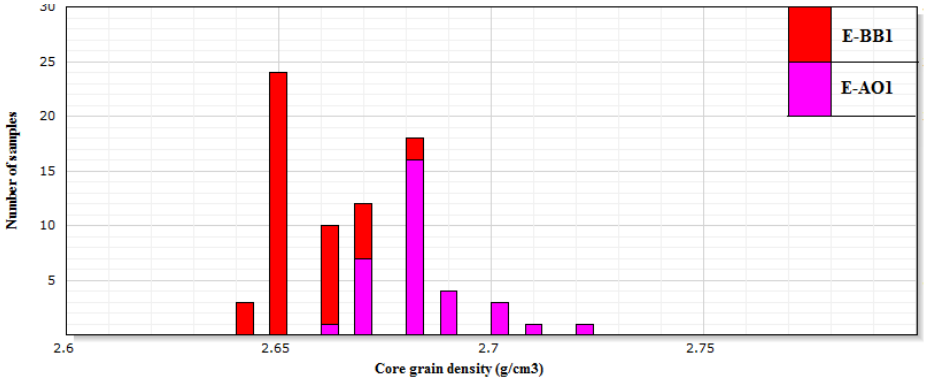

Figure 5.5: Core grain density histogram of wells E-AO1 and E-BB1.

5.2.2.2 Fluid Density

The fluid density is the density of fluid within the pore space of the formation without the matrix materials. The depth of investigation of the bulk density tool is limited to about 10cm (Rider, 1996). Therefore, the tools measure the invaded zone where the mud filtrate replaced the formation water or hydrocarbons. So, the value of the fluid density in relationship 5.11 represents the mud filtrate density and not the formation fluid density. In gas bearing formations the situation is more complex. The gas phase has high mobility and it replaces the invading mud filtrate rapidly (Benedictus, 2007). As consequence, the actual fluid investigated by the density tool is a mixture of mud filtrate and gas.

In this study, to get reliable values, the fluid density (ρ_f) was obtained from core porosity and bulk density (RHOB) cross-ploting. An example of this cross-plot is shown in figure 5.6, where the core porosity and density log from E-AO1 are plotted together. In this plot, zero porosity corresponds to the value of the matrix density of the formation (2.66 g/cm^3), which is equal to the matrix density obtained from core analysis. In other hand, 100% porosity is corresponds to the value of fluid density. A value of 0.79 g/cm^3 is obtained from the graph and will be used in porosity calculations in gas bearing formations.

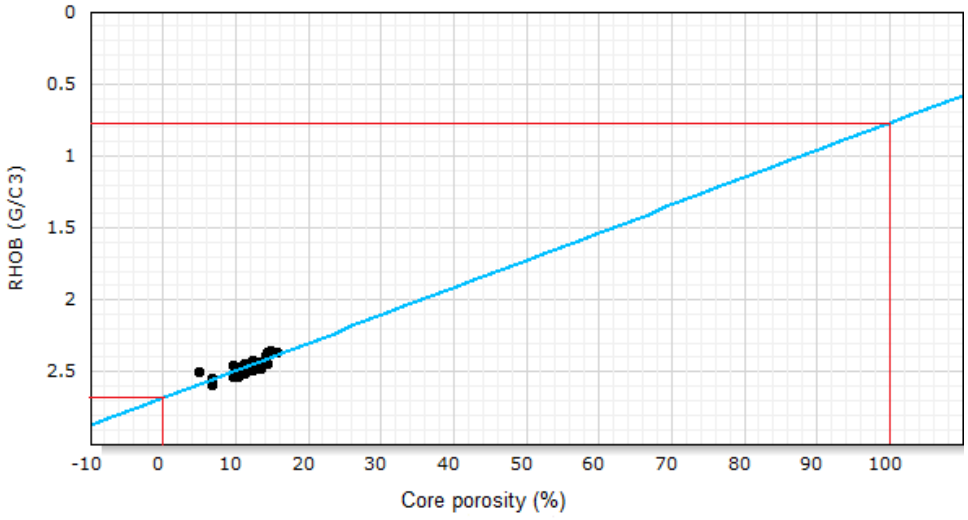

Figure 5.6: Core porosity and density log cross-plot of E-AO1.

5.2.3 Porosity from Sonic Log

The sonic log is a recording of the time required for a sound wave to traverse one foot of formation. This time (Δt) known as transit time or slowness, it depends on lithology and porosity. The logging technique of the tools is to fire a pulse of sound wave from a transmitter and measure the travel time through the formation to a receiver. Slowness is reciprocal of the velocity of the sound, and it is expressed in microsecond per foot (μsec/ft). A reliable formation porosity value could be extracted from the sonic log when the lithology is known.

(Wyllie et al., 1956) proposed a simple equation to describe the behaviour of slowness and porosity and called it the time average equation (Asquith and krygowski, 2004). This equation can be written as:

$$\Phi = \frac{\Delta t_{log} - \Delta t_{ma}}{\Delta t_f - \Delta t_{ma}} \tag{5.7}$$

where:
Φ : the porosity of the rock.
Δt_{log} : the transit time in the formation.
Δt_{ma} : the transit time in the rock matrix.
Δt_f : the transit time in the fluids occupying the porosity.

However, in this study the Raymer-Hunt-Gardner equation has been used to calculate porosity from sonic log. This equation is more suitable for low porosity formations and it

can be applied over the entire porosity range from 0% to 100%, and porosity is provided without any corrections (Raymer et al., 1980). The equation can be expressed as following for porosity less than 37%:

$$\Phi = 1 - \left(\frac{\Delta t_{ma}}{2 * \Delta t_f}\right) - \sqrt{\left(\frac{\Delta t_{ma}}{2 * \Delta t_f}\right)^2 - \frac{\Delta t_{ma}}{\Delta t_f} + \frac{\Delta t_{ma}}{\Delta t_{log}}} \tag{5.8}$$

5.2.4 Porosity from Density and Neutron Logs

The combination of density and neutron logs is a popular method for the estimation of total porosity. This method is usually used in the gas reservoir to compensate the effect of gas on neutron and density logs (Hamada and Abushanab, 2008). In literature, various combination formulas are used, but the most widely used is obtained by averaging the apparent neutron and density porosities as the following:

$$\Phi = \frac{\Phi_{density} + \Phi_{neutron}}{2} \tag{5.9}$$

5.2.5 Core-Log Calibration

The calculated porosities from wireline logs have been compared with laboratory core measured porosity. This procedure is done to check which log derived porosity will give the most reasonable match with core porosity, and to what degree.

For E-BB1, the log derived porosities are shown in figure 5.7 overlaid by core porosity. Density porosity is plotted in track 4 in black, sonic porosity in track five in green, and density-neutron porosity in track six in red. In track seven, the core facies is plotted as indicator of the lithology.

The porosities derived from the density log and density-neutron best match with the core porosity, where the sonic log derived porosity is higher than core porosity as shown. The figure also shows that the cored interval is clean sandstone (facie A). Because of this shale free interval, no shale effect in porosity computation can be detected. In addition, both the density log and density-neutron derived porosities have corrected for gas effect as previously discussed.

For E-AO1, the log derived porosities are shown in figure 5.8 overlaid by core porosity. Density porosity is plotted in track 4 in black, sonic porosity in track five in green, and density-neutron porosity in track six in red.

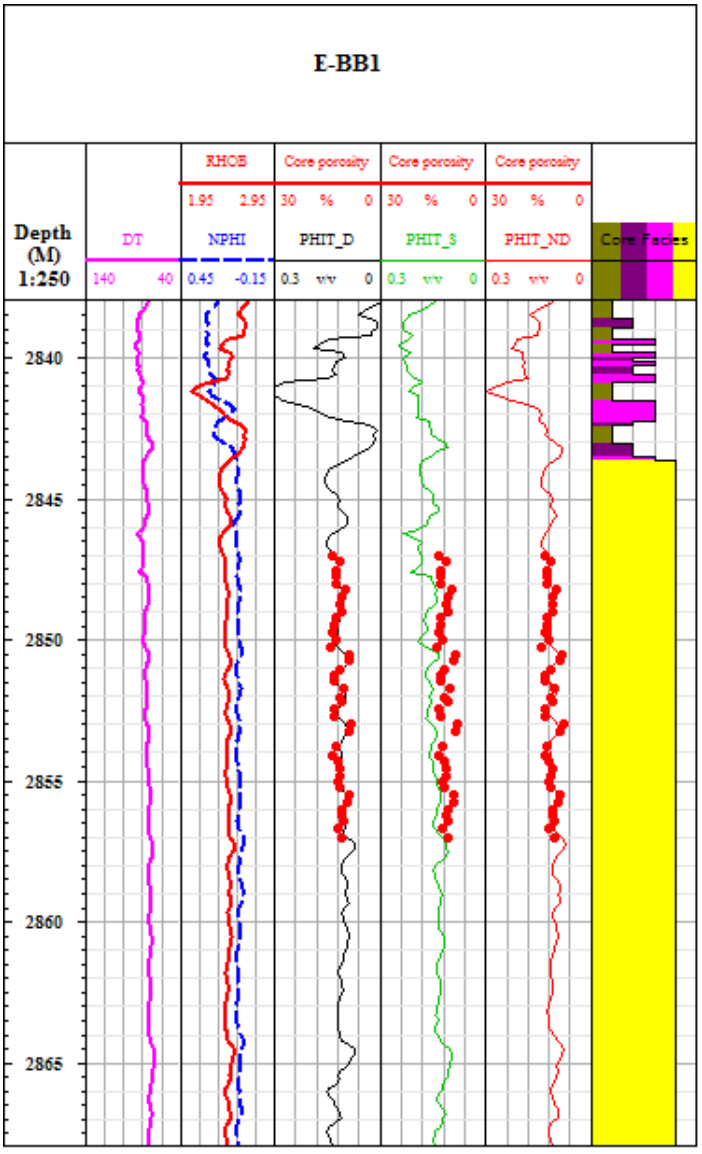

Figure 5.7: Calculated porosities overlaying core porosity in E-BB1.

The porosity derived from the density log gives a reasonable match with the core porosity with some deviations. The figure shows that the cored interval is shaly sandstone (facie B). The effect of shale is therefore clearly observed in density derived porosity.

In conclusion, the density derived porosity showed the best match with the core porosity. It will be used as porosity model in this study.

5.2.6 Effective Porosity

Effective porosity is defined as the total porosity less clay bound water (Ellis and Singer, 2008). This means it excludes all the bound water associated with clays. By this definition, shale has no effective porosity, whereas clean sandstone has an effective porosity

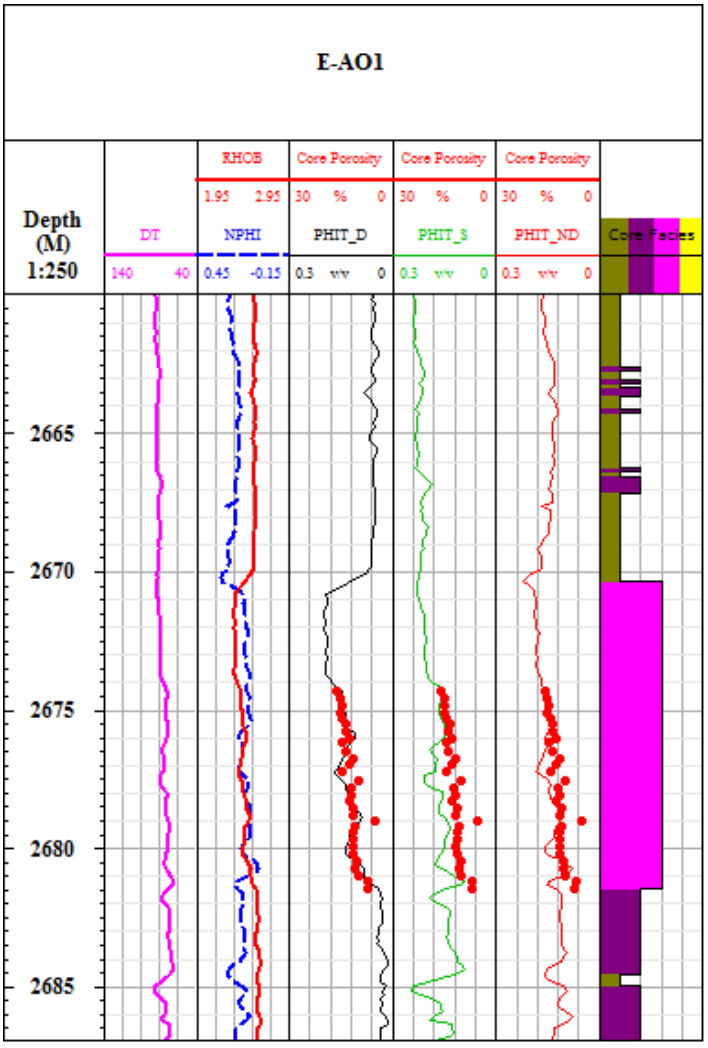

Figure 5.8: Calculated porosities overlaying core porosity in E-AO1.

equal to the total porosity.

For all studied wells, effective porosity has been determined from the density log as the following:

$$\Phi_e = \Phi_T - (\Phi_{sh} * V_{sh}) \tag{5.10}$$

where:
Φ_e : Effective porosity.
Φ_T : Total porosity.
Φ_{sh}: Shae porosity.
V_{sh} : Shale volume.

given that:

$$\Phi_{\text{sh}} = \frac{\rho_{\text{ma}} - \rho_{\text{sh}}}{\rho_{\text{ma}} - \rho_{\text{f}}} \tag{5.11}$$

5.3 Saturation Determinations

The fluid saturation is the fraction or percentage of the formation porosity occupied by a certain fluid. In a reservoir, the occupied fluids are either hydrocarbons (oil and/or gas) or water. The nature of the fluid is generally inferred from resistivity logs. Resistivity logs are also used in saturation calculations to quantify the values of oil and gas in place. The true formation resistivity (R_t) is the most important parameter because it is related to hydrocarbon saturations.

5.3.1 Water Saturation

Distinguishing between hydrocarbons and water occupying the reservoir is critical. This can be done by determine the water saturation within the zone of interest, since the total saturation of the fluids in the reservoir is 100%. Water saturation distribution is one of the most important parameters in formation evaluation. The accurate determination of water saturation is essential for accurate volumetric calculation which is of commercial interest.

In this project, water saturation was calculated from wireline logs and compared with core data for validation. Five saturation models were used namely: dispersed Shale, Indonesia, modified Simandoux, total shale and modified total shale. All these models are shaly-sand methods and use the effective porosity as input in the calculations. These models were developed from Archie equation to account for the effect of shale and all regress to the basic Archie equation at zero shale volume.

The exact equations for these models together with Archie equation are shown in table 5.2 below.

Table 5.2: Water saturation equations used in the study.

No	Model	Equation
1	Archie	$S_w = \left(\frac{a*R_w}{R_t*\Phi^m}\right)^{\frac{1}{n}}$ (Archie, 1942)
2	Total shale	$S_w = \left[\frac{aR_w}{\Phi_e^2*R_t} + \left[\frac{aR_wV_{sh}}{2\Phi_e^2R_{sh}}\right]^2\right]^{0.5} - \frac{aR_wV_{sh}}{2\Phi_e^2R_{sh}}$
3	Indonesia	$\frac{1}{\sqrt{R_t}} = \left[\frac{V_{sh}^{(1-\frac{V_{sh}}{2})}}{\sqrt{R_{sh}}} * \frac{\Phi_e^{\frac{m}{2}}}{\sqrt{aR_w}}\right] * S_w^{\frac{n}{2}}$ (Poupon and Leveaux, 1971)
4	Modified Simandoux	$S_w = \left[\frac{aR_w(1-V_{sh})}{\Phi_e^mR_t} + \left[\frac{V_{sh}aR_w(1-V_{sh})}{2\Phi_e^mR_{sh}}\right]^2\right]^{\frac{1}{n}} - \frac{V_{sh}aR_w(1-V_{sh})}{2\Phi_e^m}R_{sh}$
5	Modified total shale	$S_w = \left[\frac{aR_w(1-V_{sh})}{\Phi_e^mR_t} + \left[\frac{V_{sh}aR_w(1-V_{sh})}{2\Phi_e^mR_{sh}}\right]^2\right]^{0.5} - \frac{V_{sh}aR_w(1-V_{sh})}{2\Phi_e^mR_{sh}}$
6	Dispersed Shale	$S_w = \Phi_e^2 + \left(\frac{a*R_w}{R_t*\Phi_e^m}\right) + \left[\frac{V_{sh}(R_{sh}-R_w)}{2R_{sh}}\right]^2$

where:
S_w : Water Saturation of the uninvaded zone.
R_t : True Resistivity of the formation (i.e. deep laterolog or deep induction log).
R_{sh} : Resistivity of shale.
V_{sh} : Volume of shale.
Φ : Porosity.
Φ_e : Effective porosity.
R_w : Formation Water Resistivity at formation temperature.
n : Saturation exponent.
m : Cementation exponent.
a : Tortuosity factor.

For the saturation calculations, most of these input parameters can be obtained from the logs. However, some needed to be determined. These include the formation temperature, formation water resistivity, saturation exponent and cementation exponent.

5.3.1.1 Formation Temperature

The accurate predictions of hydrocarbon saturations require knowledge of formation temperature since temperature controls the salinity of the formation water and therefore the electrical properties of the formation. The resistivity of formation water decreases with increasing temperature.

The formation temperature of the studied wells has been estimated using the following equation:

$$F_{temp} = TLT + \frac{(BLT - TLT) * (depth - TLI)}{(BLI - TLI)} \tag{5.12}$$

where:
F_{temp} : Formation temperature (degC).
TLT : Top log temperature (degC).
TLI : Top log Interval (m).
BLT : Bottom log temperature (degC).
BLI : Bottom log Interval (m).

5.3.1.2 Formation Water Resistivity

Formation water is defined as the water uncontaminated by drilling mud that saturates the porous formation (Ushie, 2001). The value of formation water resistivity needs to be determined for any formation evaluation to quantify the saturation. Several methods were proposed, in literature, to calculate the formation water resistivity. However, in this project the spontaneous potential method was used.

The magnitude of SP deflection depends on the resistivity of water saturation and the resistivity of the mud filtrate. Therefore, it is possible to calculate formation water resistivity when the resistivity of the mud filtrate is known. The equation used for this determination is (Enikanselu and Adekanle, 2008):

$$SSP = -K \log(R_{mfe}/R_w) \tag{5.13}$$

where:
SSP: The static SP which is the maximum deflection of the SP opposite permeable bed.
K : Temperature dependent constant.
R_{mfe} : Equivalent Resistivity of mud filtrate.
R_w : Resistivity of formation water.

The resistivity of the mud filtrate (R_{mf}) is determined in the studied wells from direct measurement on the drilling mud samples and provided in log headers as shown in table 5.3.

Table 5.3: Water saturation equations used in the study.

Well	R_{mf} (ohm.m)	Temperature (degC)
E-AD1	0.198	22.2
E-AO1	0.199	16.1
E-AO2	0.212	25
E-BB1	0.185	24.4
E-BB2	0.128	19.5

This method has been applied to water zones in the studied wells. An average value of water resistivity of about 0.135 ohm.m was estimated. This value will used in saturation calculations.

5.3.1.3 Pickett Plot

Pickett plot is a graphical solution of Archie equation; it plots the formation resistivity R_t against the porosity on a double logarithm scale. This can be expressed mathematically by rearranging Archie equation as following:

$$\log \Phi = -\frac{1}{m} \log R_t - n \log S_w + \log R_w \tag{5.14}$$

At 100% water saturation, the plot should result in a straight line of negative slope through the lowest resistivity points corresponding to different porosities (Opuwari, 2010). The intercept at the 100% porosity point gives the value of the formation water resistivity directly.

Hydrocarbon bearing points will plot away from the 100% water saturation, moved horizontally to the right by their increased resistivity. The distance of a point from the 100% water saturation line depends on the water saturation of that point (Krygowski, 2003). Lines of constant water saturation lie parallel to the 100% water saturation and the separations between these lines are dependent on the saturation exponent (n).

In this study the Pickett plot is used to determine the values of saturation exponent (n) and cementation exponent (m). Normally these values are obtained from special core analysis which were not available for this study.

An example of the Pickett plot is shown in figure 5.9. The plotted points represent water bearing intervals in E-AD1.

The formation water resistivity is 0.135 as obtained from the SP method. The calculated values of saturation exponent (n) and cementation exponent (m) from the plot are 2 and 1.94 respectively.

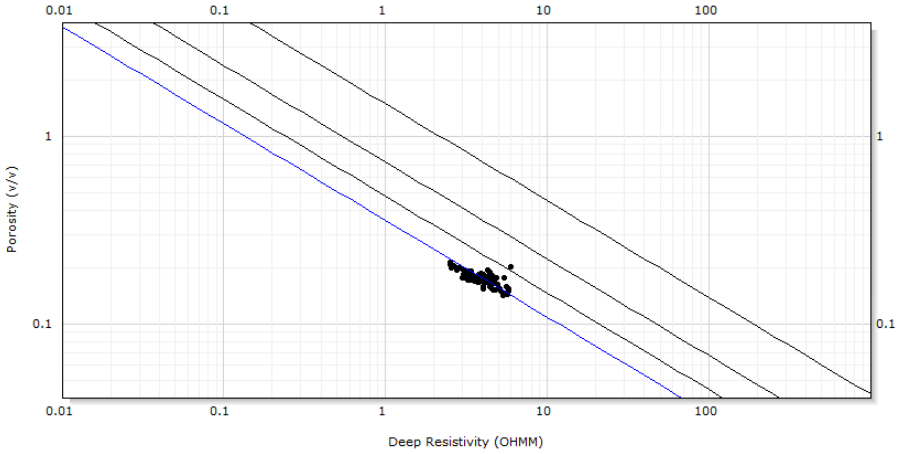

Figure 5.9: Pickett Plot for determination of exponent (n) and cementation exponent (m) for well E-AD1.

5.3.1.4 Core-log Calibration

The calculated water saturation from the wireline logs have been compared with laboratory core measured water saturation. Figures 5.10 and 5.11 are the comparisons of conventional core water saturation measurements with log calculated water saturation models.

The water saturation models total shale, Indonesia, modified Simandouk, modified total shale, and dispersed shale are plotted in track 3,4,5,6 and 7 respectively. The Indonesia model in track 4 (green) best matches with the water saturation from conventional core analysis and will be used in saturation calculation.

The Indonesia model was developed empirically by Poupon and Leveaux for the fresh formation waters and high shaliness of many Indonesian reservoirs in which oil was produced from zones of low resistivity values (Poupon and Leveaux, 1971), (Ellis and Singer, 2008).

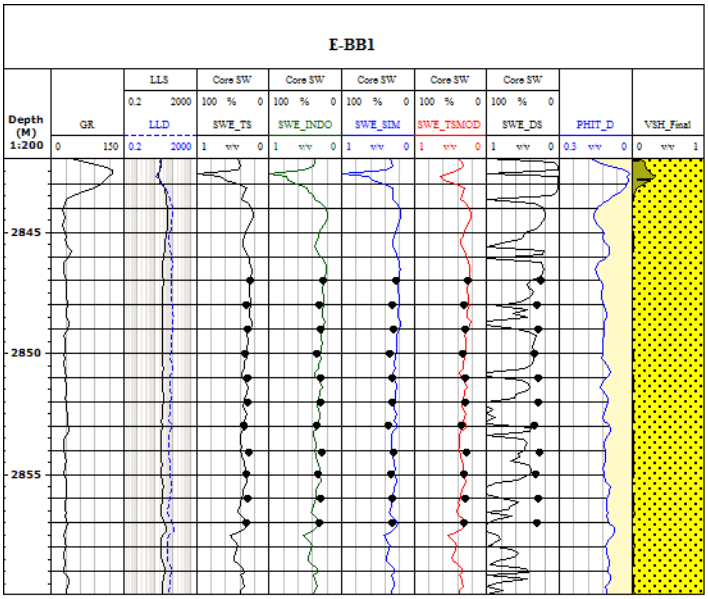

Figure 5.10: Comparison of core and log water saturation models for Well E-BB1.

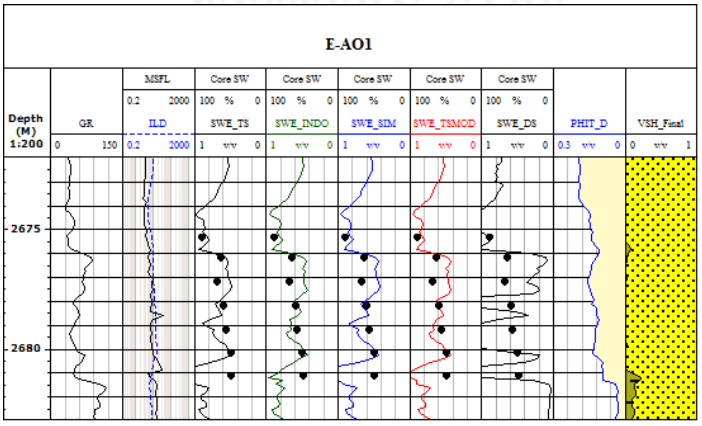

Figure 5.11: Comparison of core and log water saturation models for Well E-AO1.

5.4 Permeability Determinations

Permeability is the property porous medium that characterises the ability of the formation to conduct fluids. Its importance in reservoir management and development comes from the fact that permeability is the parameter which controls the movement, and the flow rate of the reservoir fluids in the formation. In general, permeability is a function of the properties of the pore space, it increases with increasing porosity, increasing grain size and improved sorting (Fuad, 2008). Permeability is measured in Darcies, usually in millidarcies (mD).

Permeability is usually obtained from well testing, cores and formation testers (Ahmed et al., 1991). Generally, it is difficult to obtain permeability from wireline logs, although several approaches have been introduced for this purpose (Balan et al., 1995), (Afify and Hassan, 2010). However, in the absence of well testing, data from core samples could be a good source for this determination.

The permeability of studied reservoirs has been calculated using two methods. They are; permeability estimated from core data by applying regression analysis of the core porosity versus core permeability, and hydraulic flow units derived permeability.

5.4.1 Core Permeability

Core technique produces direct measurement of permeability which can be obtained either under room condition or in situ reservoir conditions. The core permeability of the two key wells (E-BB1 and E-AO1) have been corrected to reservoir conditions (chapter three refers).

The core permeability of E-BB1 and E-AO1 is distributed between 0.01 mD and 103.48 mD with a mean value of 12.9 mD as shown in figure 5.12.

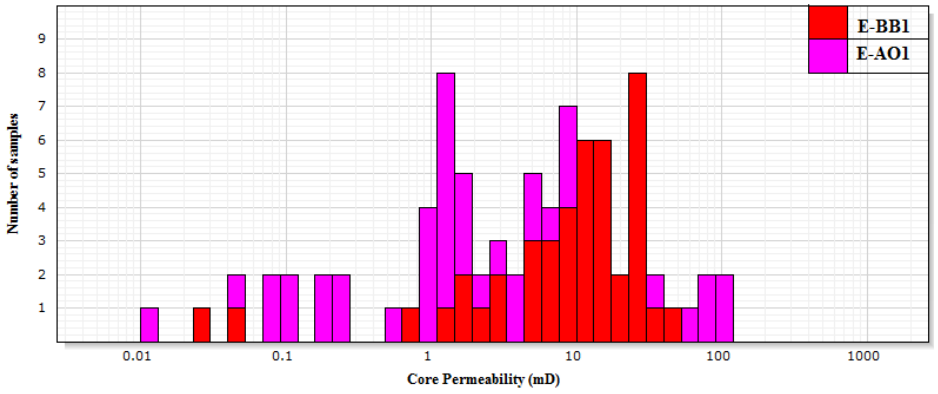

Figure 5.12: E-BB1 and E-AO1 core permeability (mD) histogram.

5.4.2 Core Permeability and Core Porosity Relationship

Regression analysis is normally used to find a relationship between two input measurements by generating a best fit equation. The obtained regression equation is then used for formation evaluation.

The linear relationship between permeability and porosity is fundamental in petrophysical studies and has been used in the early stage of petroleum industry. However, this simple relationship was unreliable and results were not in good agreement with field data (Nooruddin and Hossain, 2011).

The correlation between core porosity and core permeability of E-BB1 and E-AO1 is presented in Figure 5.13 below. The resultant regression equation which represents the porosity-permeability function is:

$$\log(\text{Permeability}) = 0.378323 * \text{Porosity} - 3.663236 \tag{5.15}$$

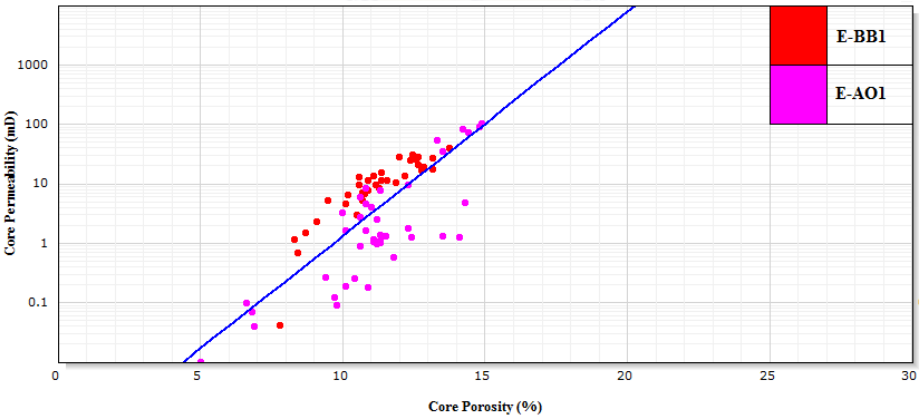

Figure 5.13: The correlation between core porosity and core permeability of E-BB1 and E-AO1.

The R^2 is obtained as a medium value (0.59), meaning that a fair correlation exists between the measured permeabilities and porosities of the core data. The figure also shows the influence of facies on the porosity-permeability relationship. E-BB1 shows a better correlation because the cored interval is clean sand (facies A) unlike E-AO1 which consists of shaly sand (facies B) along the cored interval.

Equation 5.15 is used to convert the porosity profile into an equivalent permeability profile in the studied wells. Figures 5.19 and 5.20 show the calculated permeability of E-AO1 and E-BB1 plotted in track five together with the core permeability for validation. The calculated permeability is not a good match with the core permeability, as expected.

5.4.3 Hydraulic Flow Units

Hydraulic Flow Units (HU) have been widely used as a reliable technique to predict the permeability in uncored wells and intervals, and for classification of rock types. There are numerous different definitions for hydraulic flow units to be found in literature.

(Ebanks et al., 1993), defined the hydraulic flow unit as a representative volume of the total reservoir rock within which geological properties that control fluid flow are internally consistent and predictably different from properties of other rocks.

Generally, hydraulic flow units are resultant of deposition environment and diagentic process (Borhani and Emadi, 2011). It can be identified as a zone in a reservoir where the flow of the hydrocarbons is consistent throughout the zone.

5.4.3.1 Estimation of Hydraulic Flow Units Using Core Data

To determine the hydraulic flow units within the cored intervals; K/Φ ratio method was used. This method was proposed by (Amaefule et al., 1993) for identification and characterization of the hydraulic flow units. Porosity and permeability of the reservoir have been considered as two of the most important parameters to predict flow units. Porosity controls the hydrocarbon storage, and flow capacity is a function of permeability.

To predict flow units using the K/Φ ratio method, three petrophysical parameters were defined; the reservoir quality index (RQI), normalized porosity index (NPI), and flow zone indicator (FZI). These parameters can be defined as:

$$(\mathrm{RQI}) = 0.0314\sqrt{\mathrm{K}/\Phi}$$
$$(\mathrm{NPI}) = \Phi/(1-\Phi)$$
$$(\mathrm{FZI}) = \mathrm{RQI}/\mathrm{NPI}$$

where:
k: core permeability.
Φ: core porosity.

These parameters have been identified in the key well (E-AO1 and E-BB1). The results are given in tables 5.4 and 5.5.

Table 5.4: E-BB1 Calculated values for RQI, NPI and FZI.

Depth	Permeability	Porosity	RQI	NPI	FZI
2847.049	27.34672	13.15664	0.04527	0.151499	0.298814
2847.249	13.62789	11.07651	0.034829	0.124562	0.279612
2847.539	28.30297	12.46326	0.047318	0.142378	0.332345
2847.789	30.30068	12.46326	0.04896	0.142378	0.343874
2848.049	24.40224	12.36421	0.044112	0.141086	0.312663
2848.249	5.211018	9.491648	0.023266	0.10487	0.221854
2848.499	12.98408	10.58124	0.034783	0.118334	0.29394
2848.749	11.30828	10.8784	0.032014	0.122062	0.262279
2849.029	9.632478	10.58124	0.029959	0.118334	0.253176
2849.249	25.85081	12.46326	0.045222	0.142378	0.317621
2849.499	25.64252	12.56232	0.044862	0.143672	0.312251
2849.749	26.73131	13.15664	0.044758	0.151499	0.295433
2850.049	28.69115	11.96799	0.048618	0.13595	0.357612
2850.269	40.29866	13.75096	0.053754	0.159433	0.337155
2850.529	1.168268	8.303001	0.011778	0.090548	0.130078
2850.779	1.490173	8.699217	0.012996	0.095281	0.136396
2851.049	15.08593	11.37367	0.036163	0.128333	0.281791
2851.249	28.19883	12.66137	0.04686	0.144969	0.323244
2851.469	20.96543	12.66137	0.040406	0.144969	0.278719
2851.719	4.690289	10.08597	0.021413	0.112174	0.190889
2852.049	8.401665	11.27462	0.027106	0.127073	0.213308
2852.219	7.13298	10.68029	0.025661	0.119574	0.214604
2852.459	18.98666	12.85948	0.038154	0.147572	0.258547
2852.719	16.72386	12.76043	0.035947	0.146269	0.245761
2853.029	0.041601	7.807733	0.002292	0.08469	0.027064
2853.289	0.685411	8.402056	0.008968	0.091728	0.097772
2853.789	13.41013	12.1661	0.032966	0.138513	0.238002
2854.109	17.33926	13.15664	0.036047	0.151499	0.237938
2854.329	11.31775	11.57178	0.031053	0.130861	0.237301
2854.579	7.596902	10.8784	0.02624	0.122062	0.214973
2854.829	9.62301	11.17556	0.029137	0.125816	0.231587
2855.049	10.59819	11.86894	0.029672	0.134674	0.220321
2855.219	11.2136	11.37367	0.031178	0.128333	0.242948
2855.509	1.471238	8.699217	0.012913	0.095281	0.135527
2855.759	2.266533	9.095432	0.015675	0.100055	0.156661
2856.049	5.182613	10.68029	0.021873	0.119574	0.182927
2856.219	6.763735	10.77935	0.024873	0.120817	0.205873
2856.469	6.441831	10.18503	0.024972	0.1134	0.220211
2856.719	10.52245	11.86894	0.029565	0.134674	0.219533
2857.049	3.042892	10.48219	0.016918	0.117096	0.144479

Table 5.5: E-AO1 Calculated values for RQI, NPI and FZI

Depth	Permeability	Porosity	RQI	NPI	FZI
2674.572	103.48	14.9	0.082749	0.175088	0.472616
2674.822	72.75	14.4	0.070577	0.168224	0.419543
2675.072	91.54	14.8	0.078092	0.173709	0.449554
2675.322	82.99	14.2	0.07591	0.165501	0.458667
2675.522	52.74	13.3	0.062528	0.153403	0.407607
2675.772	35.15	13.5	0.050667	0.156069	0.324644
2676.022	9.6	12.3	0.02774	0.140251	0.197791
2676.172	4.81	14.3	0.018211	0.166861	0.109139
2676.472	1.29	13.5	0.009706	0.156069	0.062193
2676.722	1.38	11.3	0.010973	0.127396	0.086134
2676.972	1.8	12.3	0.012012	0.140251	0.085646
2677.232	1.25	14.1	0.009349	0.164144	0.056957
2677.572	0.09	9.8	0.003009	0.108648	0.027696
2677.822	0.57	11.8	0.006901	0.133787	0.051584
2678.072	1.32	11.5	0.010638	0.129944	0.081868
2678.242	1.25	12.4	0.00997	0.141553	0.07043
2678.522	0.18	10.9	0.004035	0.122335	0.032984
2678.772	1	11.3	0.009341	0.127396	0.073322
2679.022	0.01	5	0.001404	0.052632	0.026681
2679.202	0.9	10.6	0.00915	0.118568	0.077167
2679.422	1.08	11.1	0.009794	0.124859	0.078444
2679.672	0.97	11.2	0.009241	0.126126	0.073266
2679.922	1.1	11.3	0.009797	0.127396	0.076901
2680.162	1.16	11.1	0.010151	0.124859	0.081297
2680.472	0.19	10.1	0.004307	0.112347	0.038334
2680.722	0.26	10.4	0.004965	0.116071	0.042773
2680.972	0.12	9.7	0.003492	0.10742	0.032513
2681.162	0.07	6.8	0.003186	0.072961	0.043665
2681.422	0.04	6.9	0.002391	0.074114	0.032258

To use the calculated FZI for a definition of the flow units in the cored intervals within the studied reservoirs, a log-log plot of NPI versus RQI was used. In such a plot samples with similar FZI values should lie in straight line with slope equal to one (Amaefule et al., 1993). Samples that lie in the same line constitute a hydraulic flow unit.

Applying this procedure to the cored interval of E-AO1 and E-BB1; six hydraulic flow units have been identified as shown in figure 5.14.

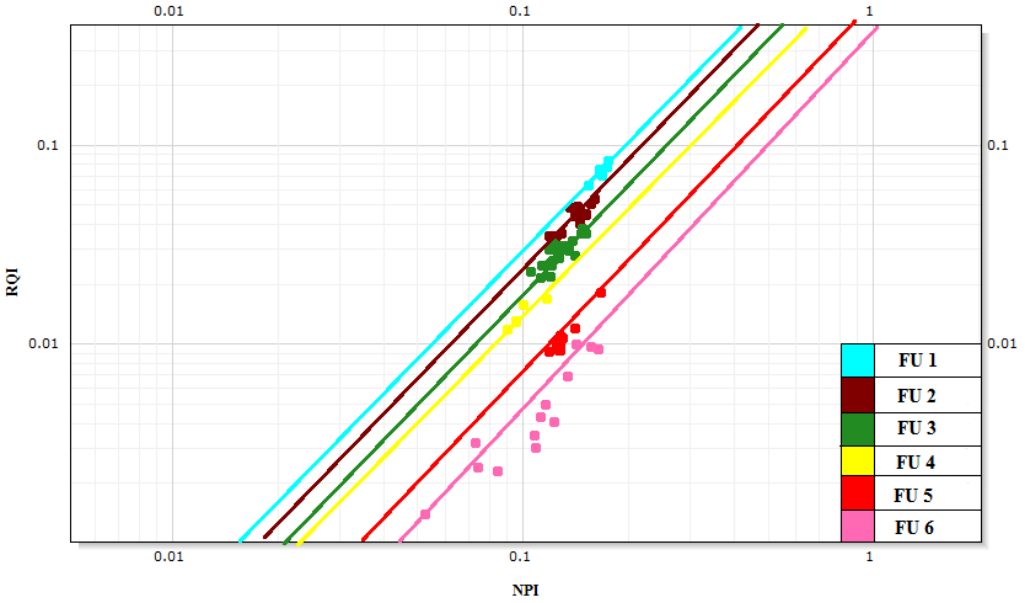

Figure 5.14: Plot of RQI versus NPI for the cored interval of E-AO1 and E-BB2 resulting in six different flow units.

The table below gives the range and the mean of FZI within each flow unit and figure 5.15 presents a histogram of FZI showing the calculated flow units. FU1 represents the best reservoir rock while FU6 represent the poorest one.

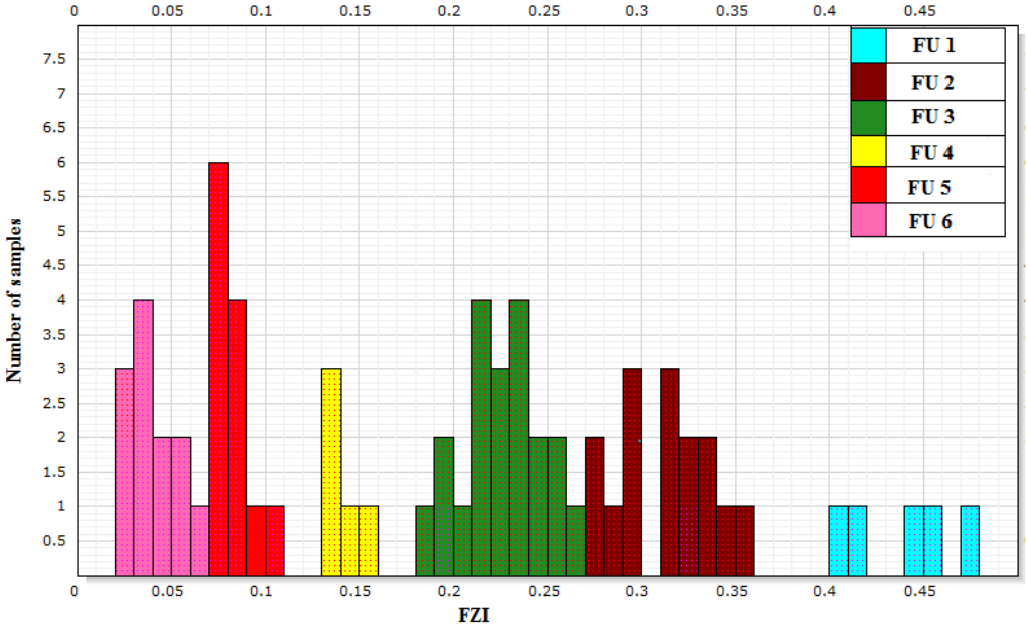

Figure 5.15: A histogram of FZI and calculated flow units.

Table 5.6: The range and the mean of FZI within the calculated flow units.

Flow Unit	FZI Range	Mean FZI
FU 6	0-0.07	0.04
FU 5	0.07-0.13	0.083
FU 4	0.13-0.18	0.141
FU 3	0.18-0.27	0.225
FU 2	0.27-0.36	0.313
FU 1	$>$ 0.36	0.441

5.4.3.2 Estimation of Flow Units in Uncored Intervals and Wells

The method discussed in the previous section predicts the flow units for the cored interval of the studied wells. To extend the calculated flow units in uncored interval and wells the Ipsom module in Techlog is used. This module provides automatic classification based on the neural network technology as discussed in chapter four. Generally, this classification is an identification of groups that are internally similar and different from others in the data according to indexation set.

To predict flow units from wireline logs; five logs were used as input parameters. The five are the: density log (RHOB), neutron log (NPHI), gamma ray log (GR), sonic log (DT) and deep resistivity log (ILD/LLD). The core identified flow units were used as an indexation set.

The obtained flow units in E-AO1 and E-BB1 are shown in figures 5.16 and 5.17 with the core identified flow units for validation. The results obtained from the Ipsom classifier are in good match with the core identified flow units and can be used for permeability calculations.

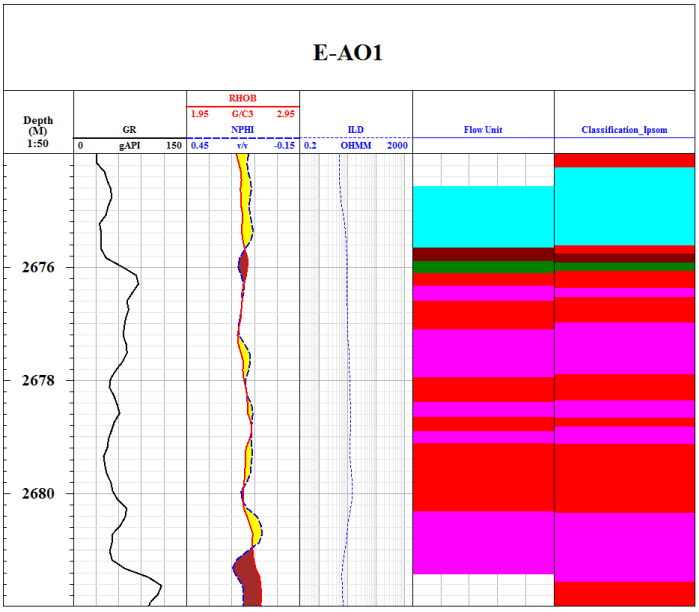

Figure 5.16: Correlation between core flow units and wireline flow units in E-AO1.

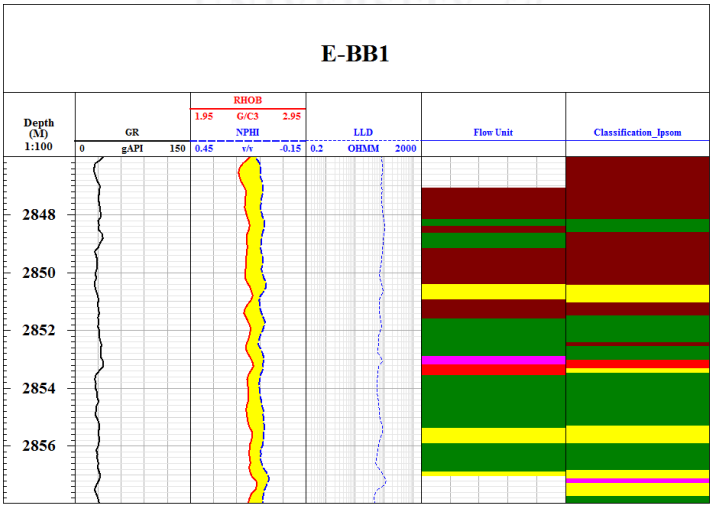

Figure 5.17: Correlation between core flow units and wireline flow units in E-BB1.

5.4.3.3 Permeability Prediction from Flow Units

The regression approach used to predict permeability in the previous section ignores the effects of lithological sequence and physics of flow at the pore scale within the cored formation. Flow units offer the opportunity to establish a relationship between formation of similar fluid conductivity and petrophysical parameters.

The correlation of RQI versus FZI yields a R^2 of 0.96 as shown in figure 5.18.

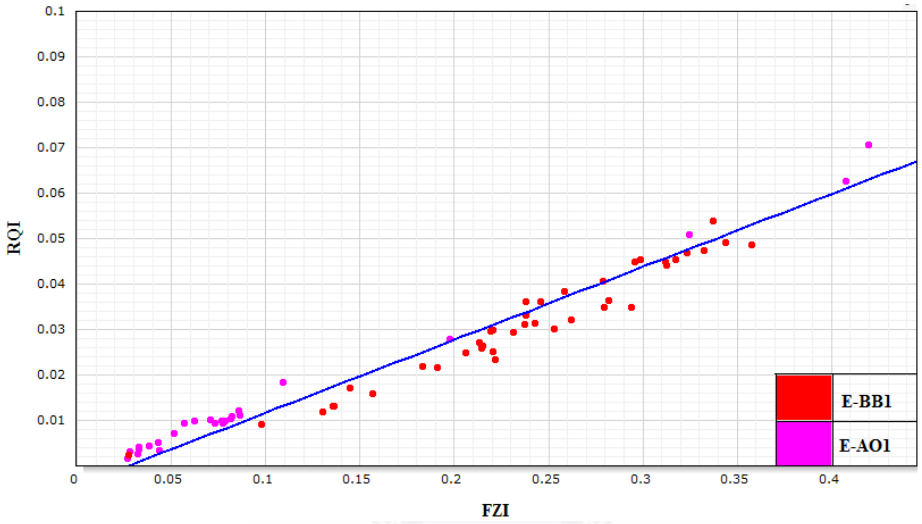

Figure 5.18: The relationship between flow zone indicator (FZI) and reservoir quality index (RQI) in the cored wells.

The regression equation is:

$$\mathrm{RQI} = 0.2019 * \mathrm{FZI} - 0.0045 \tag{5.16}$$

given that:

$$(\mathrm{RQI}) = 0.0314\sqrt{\mathrm{K}/\Phi}$$

Equation 5.16 can be written as:

$$0.0314\sqrt{\mathrm{K}/\Phi} = 0.2019 * \mathrm{FZI} - 0.0045 \tag{5.17}$$

The permeability then can be obtained as following:

$$\mathrm{K} = (5.893 * \mathrm{FZI} - 0.1433)^2 * \Phi \tag{5.18}$$

Equation 5.18 is used to calculate the permeability from wireline logs. The total porosity model and the mean FZI presented in table 5.6 are used as inputs. Figures 5.19 and 5.20 show the predicted permeability of E-AO1 and E-BB1 plotted in track four together with core permeability for validation. The calculated permeability is in a good match range with core permeability and will be used as permeability model.

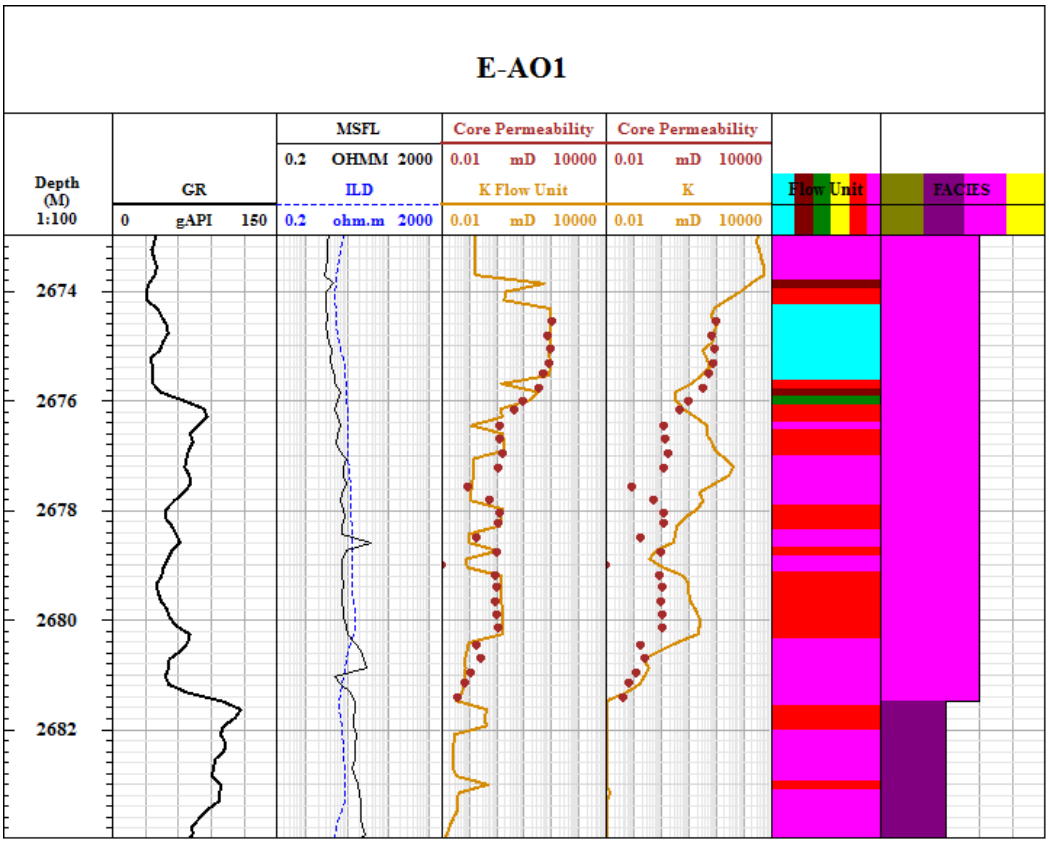

Figure 5.19: Comparison of core and log permeability models for Well E-AO1.

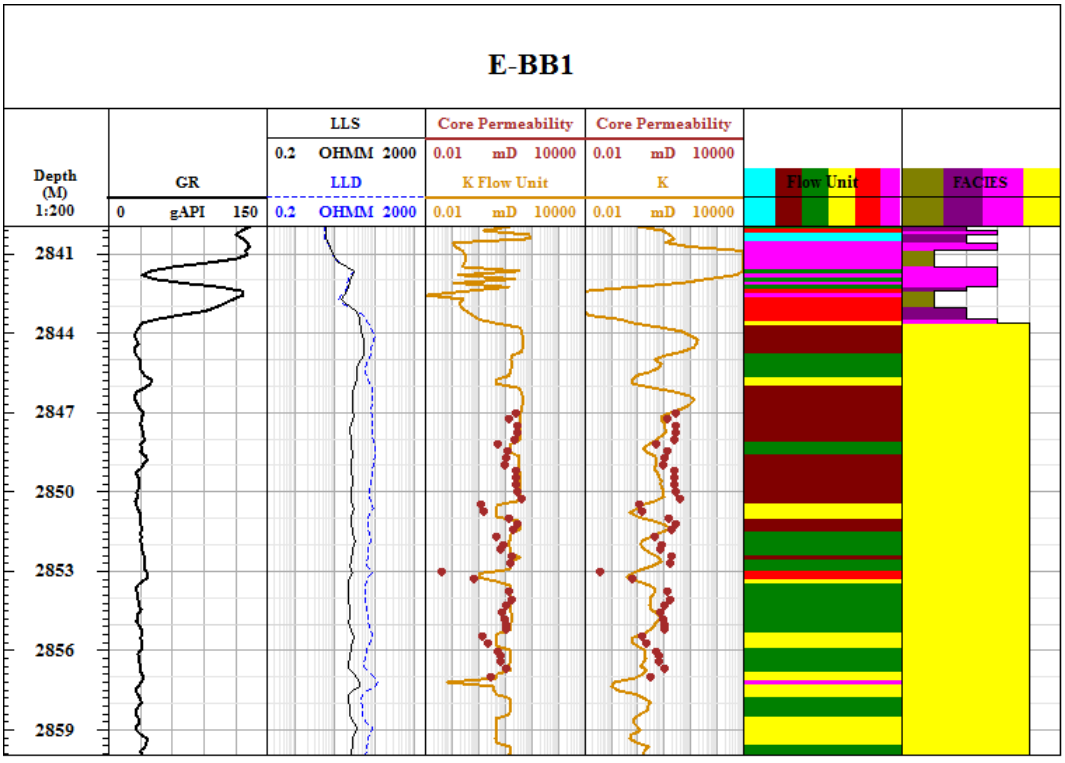

Figure 5.20: Comparison of core and log permeability models for Well E-bb1.

Chapter 6

Determination of Cut-Off and Net Pay

This chapter discusses the final petrophysical results of the studied reservoirs. It includes determinations of the net pay intervals within the 13 reservoirs identified in the previous chapters.

For any reservoir characterization; determination of net pay is needed to calculate volumetric hydrocarbons in place. Net pay is defined as any interval that contains producible hydrocarbon at economic rates. Normally the net pay thickness is related to the reservoir rock by the mean of net to gross ratio. The net to gross ratio is the ratio of the net pay thickness to the total thickness of the studied reservoir. (Worthington and Consentino, 2005) showed that net pay and net to gross ratio are crucial to compute the hydrocarbon reserves and have a significant impact on the economic possibility of hydrocarbon reservoir production.

The gross interval for the studied wells was determined by consider the top and bottom of the predefined reservoir zones.

6.1 Cut-Off Determinations

Net pay determination usually involves applying set of appropriate cut-offs on petrophysical parameter to distinguish between intervals that have reservoir potential, and intervals that do not.

Historically, several approaches have tried to locate productive zones by comparing the readings of different wireline logs at a certain depth to classify the gross interval into net pay and non-net pay intervals. These approaches include using of combination of gamma and resistivity logs as proposed by (Snyder, 1971). Modern methods include using a diffusivity equation to calculate net pay from wireline logs (Masoudi et al., 2011).

In this study the conventional method to calculate the cut-off has been used. This includes applying cut-off to permeability, porosity, shale volume and water saturation by making use of core measurements to get reliable estimations.

6.1.0.4 Permeability Cut-Off

Permeability cut-off is usually the starting point in net pay determinations (Cobb and Marek, 1998). It is considered as the controlling parameter that directly separate reservoirs from non-reservoir rocks (Widarsono, 2010). Pores with permeability less than cut-off values will not allow fluids to flow. In gas reservoirs, the permeability cut-off should be very low because gas is more mobile than oil.
In the studied wells the permeability cut-off value is considered to be 0.1 mD. Core permeability is available for the two key wells (E-AO1 and E-BB1). Figure 6.1 shows the core permeability histogram of these two wells showing the cut-off points and the reservoir and non-reservoir rocks.

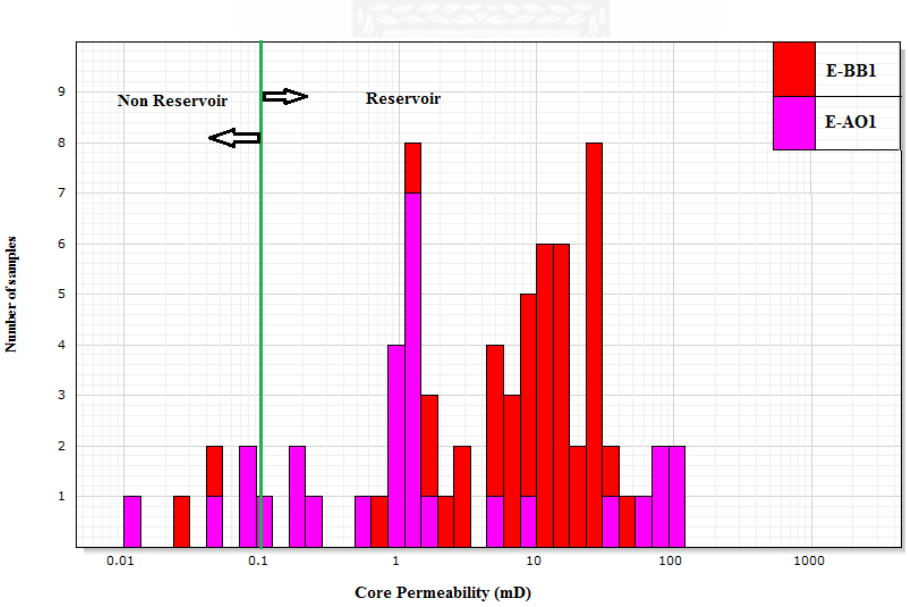

Figure 6.1: Core permeability histogram of the key wells showing the cut-off points.

6.1.0.5 Porosity Cut-Off

The determination of porosity cut-off values relies on a generating porosity-permeability relationship from the core measurement. A semi logarithmic porosity vs. permeability cross-plot of the key wells is presented in figure 6.2 below. The figure indicates that a porosity of 7 percent corresponds to the permeability cut-off (0.1mD).

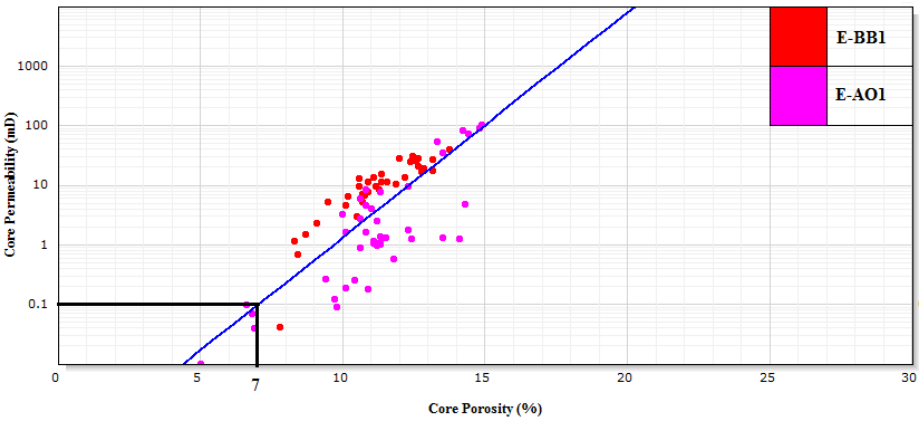

Figure 6.2: Porosity-permeability cross plot to estimate porosity cut-off values.

6.1.0.6 Shale Volume Cut-Off

The shale volume cut-off is used to distinguish between reservoir and non- reservoir rock. It defines the reservoir intervals by removing all intervals that have a volume of shale more than a certain value of shale.

The volume of shale versus porosity with gamma-ray log used as a colour mode of the studied wells is presented in figure 6.3 below. A value of 0.35 is determined as the shale volume cut-off.

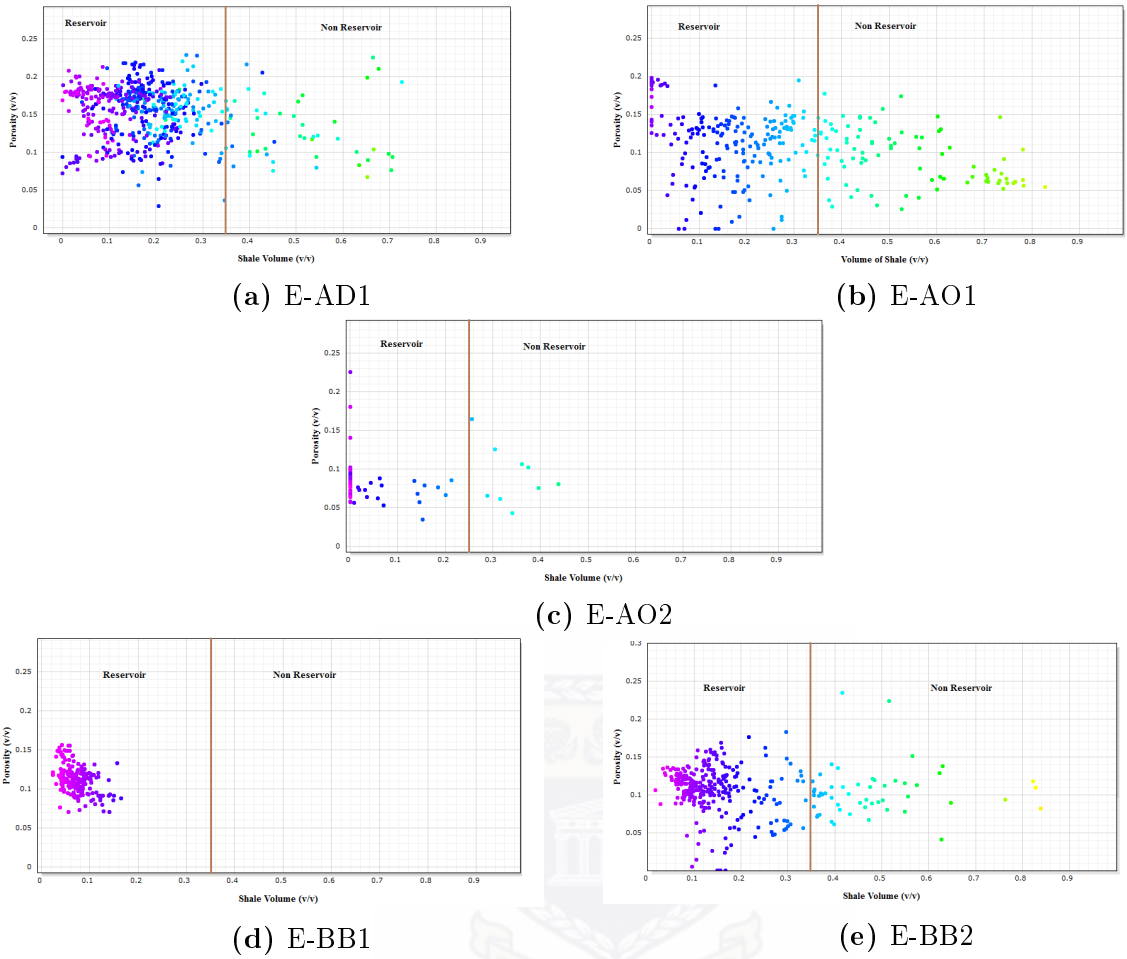

(a) E-AD1 **(b)** E-AO1

(c) E-AO2

(d) E-BB1 **(e)** E-BB2

Figure 6.3: Volumes of shale versus porosity cross plots of the five studied wells showing the reservoir and non-reservoir intervals

6.1.0.7 Water Saturation Cut-Off

To distinguish between the hydrocarbons pay zone and water zones; the saturation cut-off of the studied reservoirs is determined. Presented in figure 6.4, the water saturation of the studied reservoirs is cross plotted versus total porosity. A value of 60% is determined as water saturation cut-off. Intervals that identified as pay zone from porosity and shale volume cut-off must have values of water saturation less than 60% to consider as hydrocarbons zones.

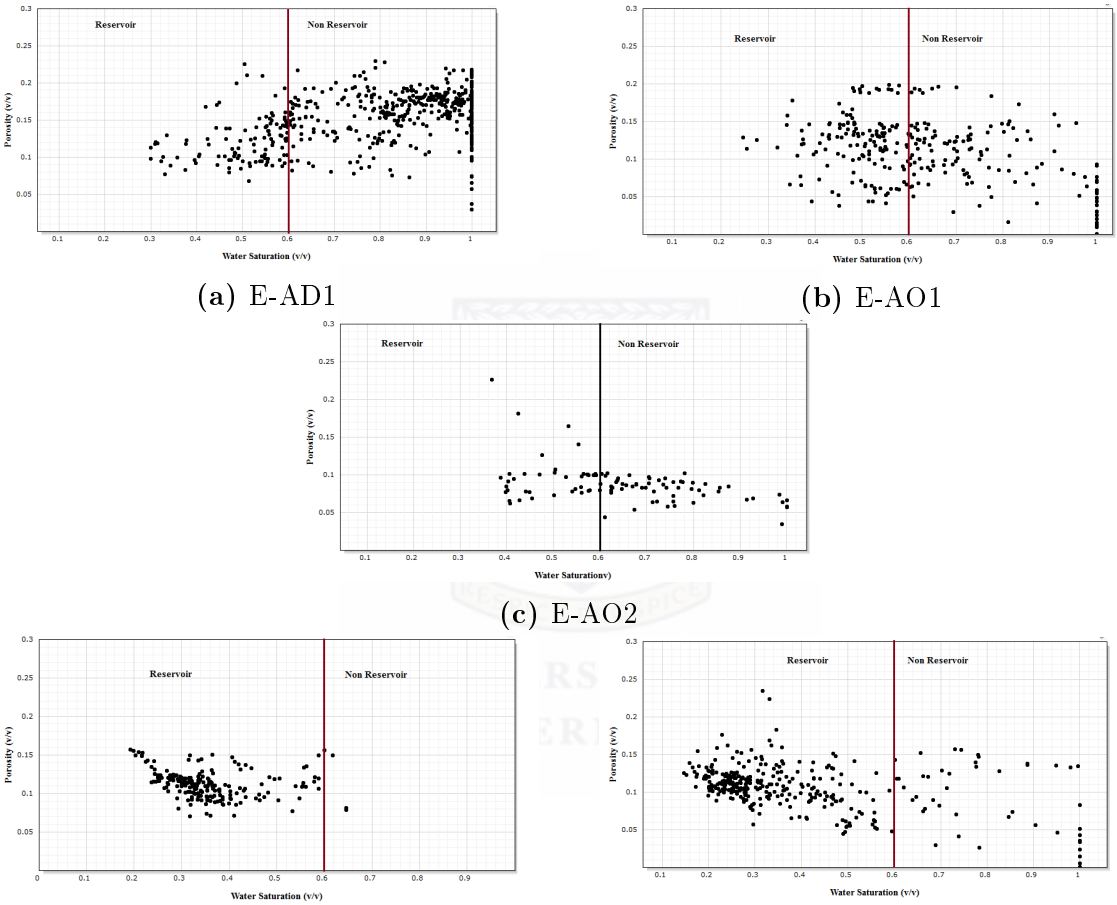

(a) E-AD1 **(b)** E-AO1

(c) E-AO2

(d) E-BB1 **(e)** E-BB2

Figure 6.4: Water saturation versus porosity cross plots of the five studied wells showing the reservoir and non-reservoir intervals.

6.2 Net Pay

This section determines, on the basis of predefined cut-offs, the reservoir intervals and thickness. The gross thickness is defined as the interval from the top to the bottom of the reservoir zone including all non-reservoir rock. Within this interval, net interval defines the thickness that contains producible hydrocarbon at an economic rate.
The calculated cut-off values have been applied to studied reservoirs to determine the net pay within each reservoir. The porosity cut-off (0.07), shale volume cut-off (0.35) and water saturation cut-off (0.6) are used for net pay calculation in this study. The non-net pay intervals were excluded by using a minimum porosity cut-off, maximum shale volume and water saturation cut-off. The obtained results are discussed further in this chapter.

6.2.1 E-AD1

As discussed in chapter four, E-AD1 has three reservoirs. The total gross thickness and net pay thickness are 82.18 and 11.58 respectively. The obtained results are given in figures 6.5, 6.6 and 6.7. 6.1 presents the calculated net pay summary for each reservoir with the average bulk volume water, shale volume, porosity, water saturation and permeability. The bulk volume water (BVW)is product of total porosity and water saturation.

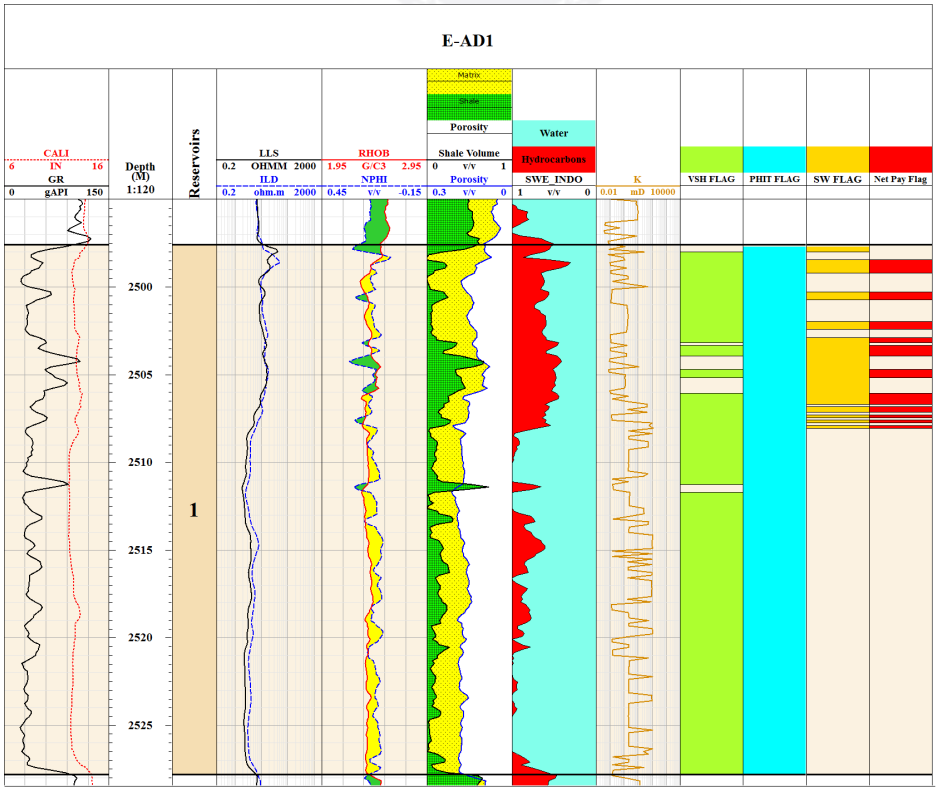

Figure 6.5: Calculated reservoir parameters and net pay interval for reservoir one in E-AD1.

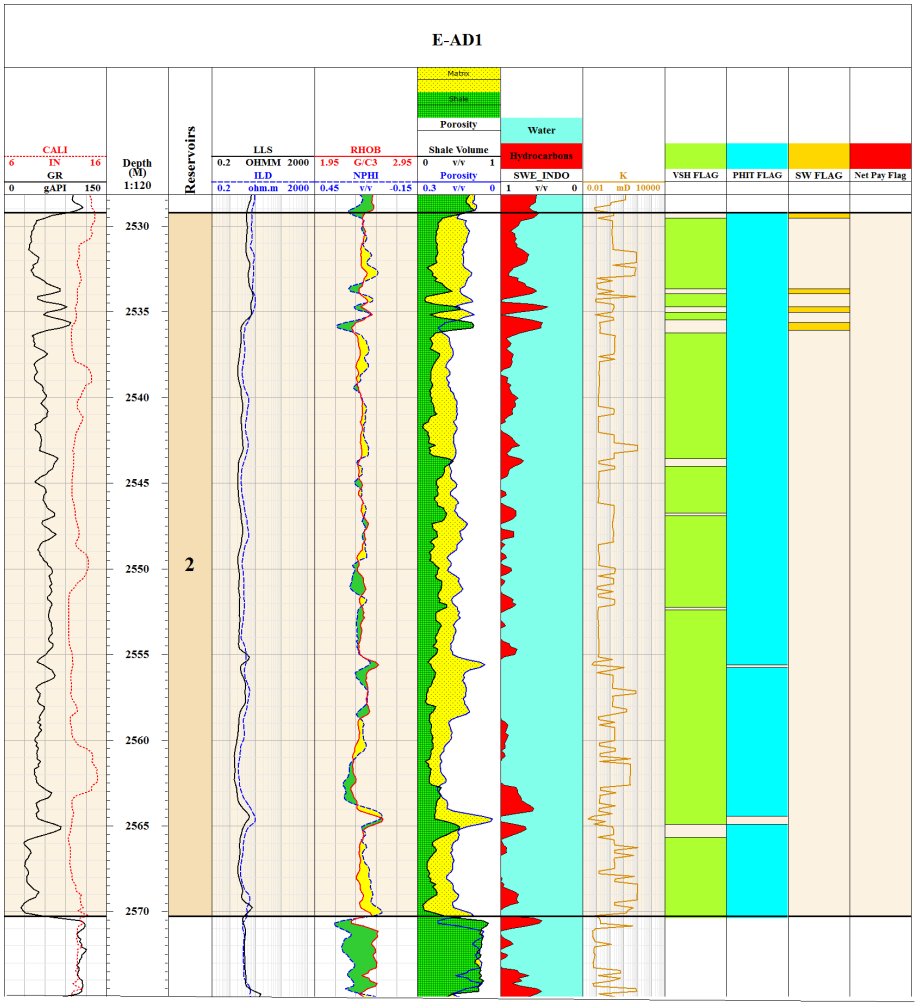

Figure 6.6: Calculated reservoir parameters and net pay interval for reservoir two in E-AD1.

Table 6.1: Summary of calculated reservoir pay parameters for E-AD1

Reservoir	Top	Bottom	Gross	Net	Net/Gross	BVW	VSh	Φ	Sw	K
One	2497.57	2527.81	30.24	4.42	0.146	0.324	0.204	0.138	0.53	4.311
Two	2529.21	2570.27	41.065	0	0	-	-	-	-	-
Three	2827.84	2838.72	10.877	7.163	0.659	0.405	0.115	0.109	0.519	2.489

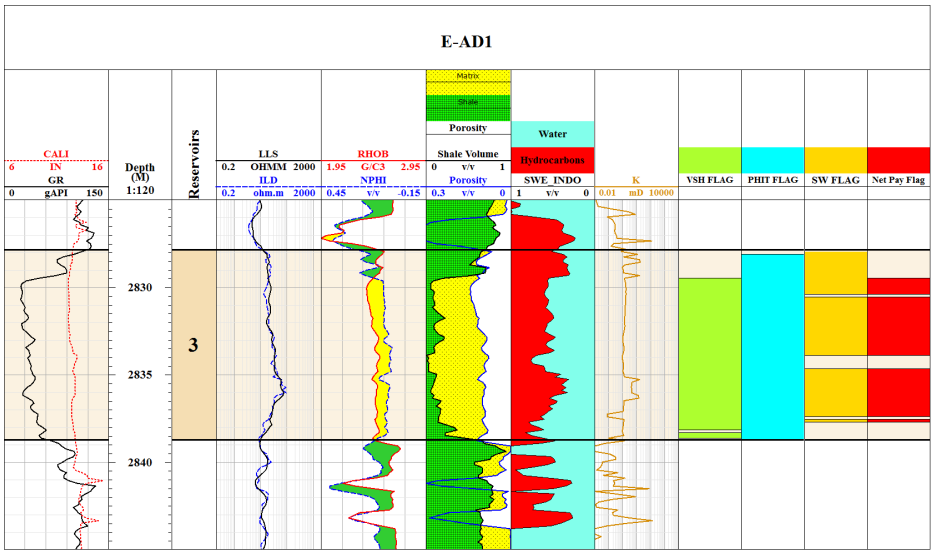

Figure 6.7: Calculated reservoir parameters and net pay interval for reservoir three in E-AD1.

6.2.2 E-AO1

Four reservoirs were identified in E-AO1 with a total gross thickness of 43.22m, and net thickness of 18.35m. The obtained results are given in figures 6.8 to 6.11. Presented in table 6.2 is the calculated net pay summary for each reservoir with the average bulk volume water, shale volume, porosity, water saturation and permeability.

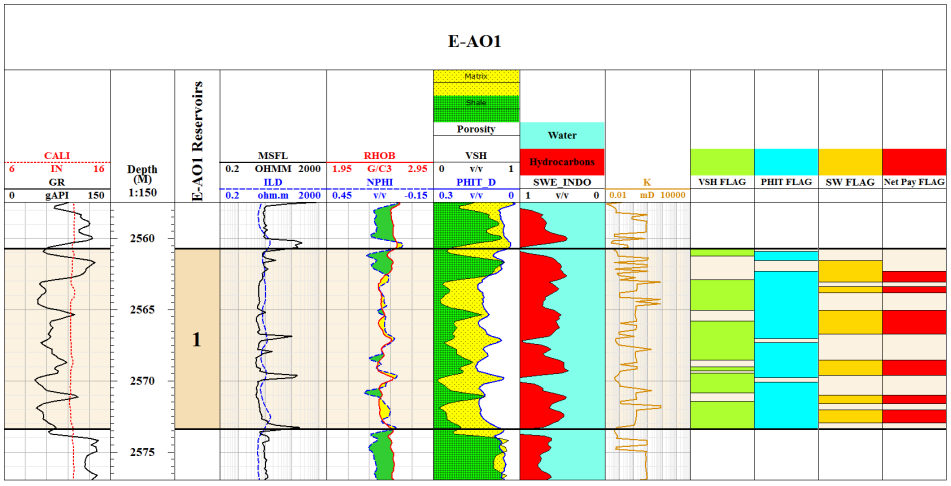

Figure 6.8: Calculated reservoir parameters and net pay interval for reservoir one in E-AO1.

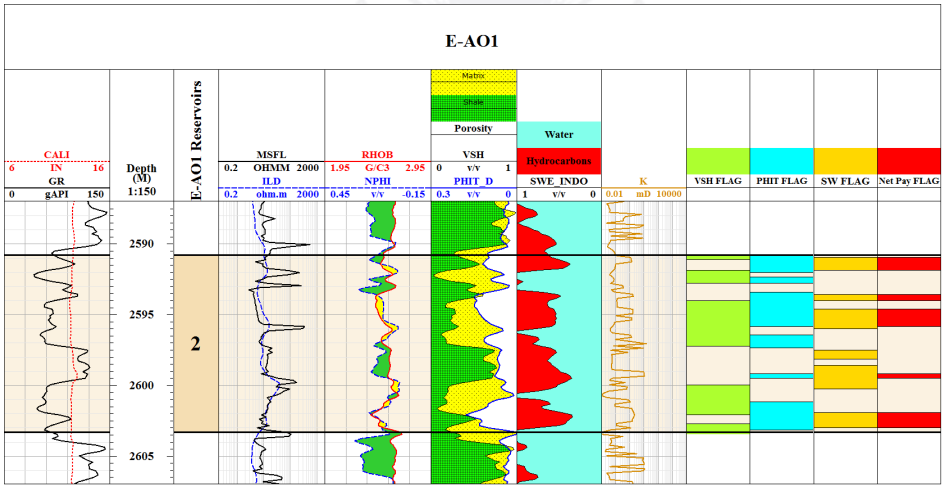

Figure 6.9: Calculated reservoir parameters and net pay interval for reservoir two in E-AO1.

Table 6.2: Summary of calculated reservoir pay parameters for E-AO1

Reservoir	Top	Bottom	Gross	Net	Net/Gross	BVW	VSh	Φ	Sw	K
One	2560.71	2573.4	12.689	5.486	0.432	0.366	0.012	0.128	0.521	1.434
Two	2590.77	2603.3	12.535	3.962	0.316	0.227	0.028	0.122	0.471	1.740
Three	2670.4	2681.56	11.162	5.446	0.488	0.43	0.004	0.157	0.503	3.176
Four	2796.89	2803.73	6.836	3.458	0.506	0.161	0.041	0.112	0.415	0.728

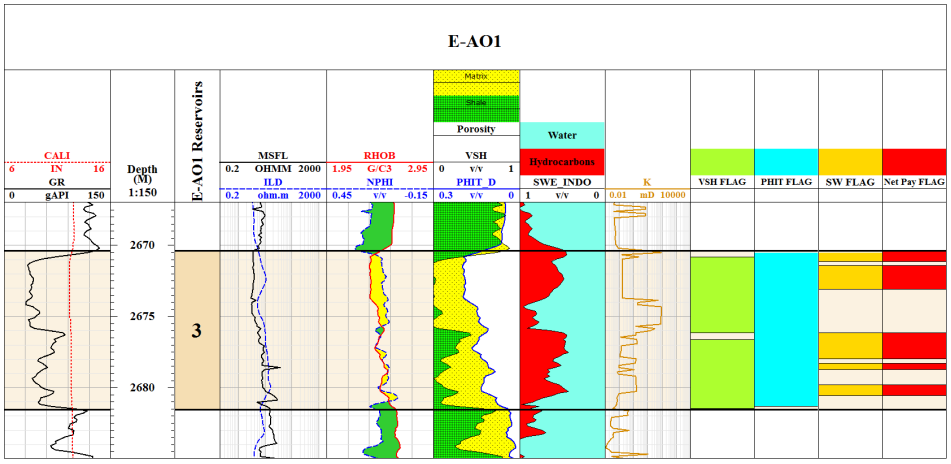

Figure 6.10: Calculated reservoir parameters and net pay interval for reservoir three in E-AO1.

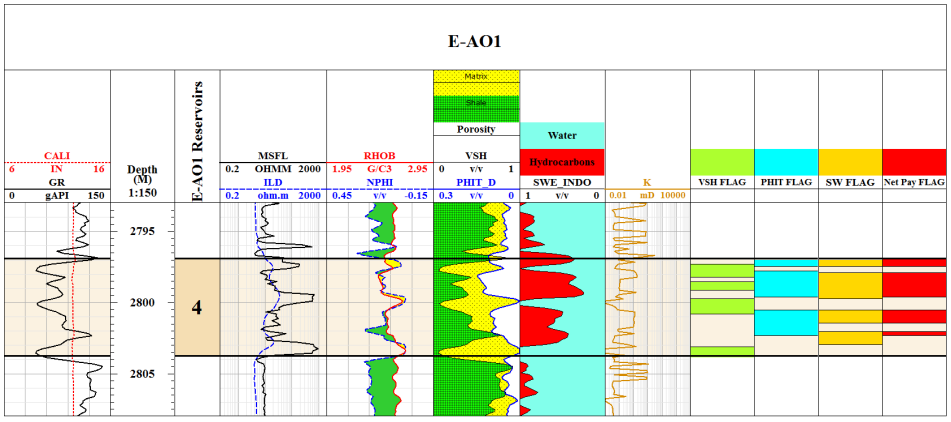

Figure 6.11: Calculated reservoir parameters and net pay interval for reservoir four in E-AO1.

6.2.3 E-AO2

E-AO2 has two reservoirs, and both showed net pay potentials. The total gross thickness and net pay thickness are 15.12m and 5.33m respectively. The obtained results are given in figure 6.12. Table 6.3 shows the calculated net pay summary for each reservoir with the average bulk volume water, shale volume, porosity, water saturation and permeability.

Table 6.3: Summary of calculated reservoir pay parameters for E-AO2

Reservoir	Top	Bottom	Gross	Net	Net/Gross	BVW	VSh	Φ	Sw	K
One	2911.01	2921.3	10.29	2.591	0.252	0.132	0.066	0.105	0.483	5.273
Two	2923.64	2928.46	4.826	2.743	0.568	0.139	0.001	0.097	0.523	10.248

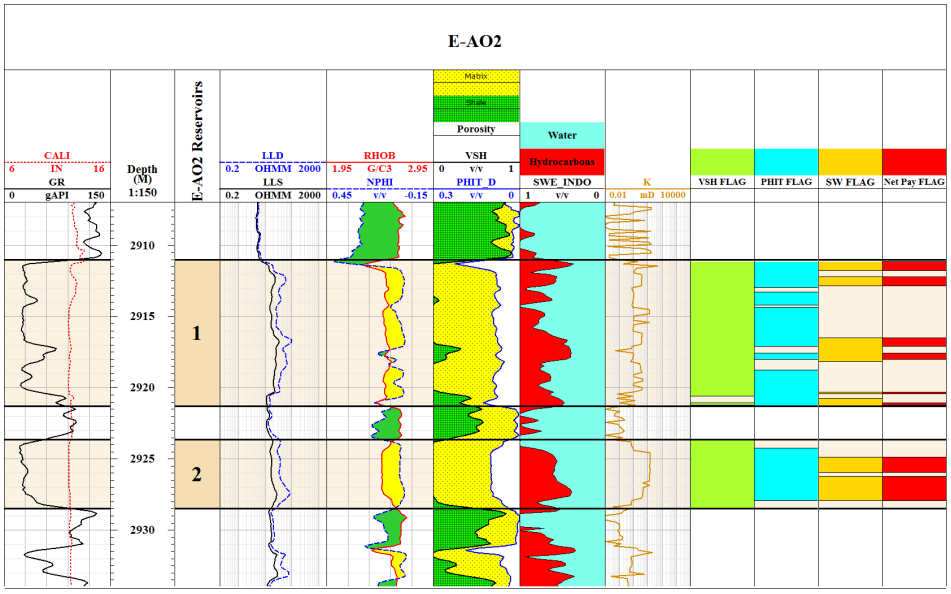

Figure 6.12: Calculated reservoir parameters and net pay interval for reservoir one and two in E-AO2.

6.2.4 E-BB1

Only one reservoir was identified in E-BB1 with a total gross thickness of 29.19m, and net thickness of 28.58m. The obtained results are given in figure 6.13. Presented in table 6.4 is the calculated net pay summary for each reservoir with the average bulk volume water, shale volume, porosity, water saturation and permeability.

Table 6.4: Summary of calculated reservoir pay parameters for E-BB1

Reservoir	Top	Bottom	Gross	Net	Net/Gross	BVW	VSh	Φ	Sw	K
One	2843.7	2872.89	29.193	28.583	0.979	1.116	0.074	0.112	0.35	15.399

6.2.5 E-BB2

Three reservoirs were identified in E-BB1 with a total gross thickness of 49.28m, and net thickness of 38.73m. The obtained results are given in figures 6.14, 6.15 and 6.16. Shown in table 6.5 is the calculated net pay summary for each reservoir with the average bulk volume water, shale volume, porosity, water saturation and permeability.

Table 6.5: Summary of calculated reservoir pay parameters for E-BB2

Reservoir	Top	Bottom	Gross	Net	Net/Gross	BVW	VSh	Φ	Sw	K
One	2539.31	2550.59	11.279	7.925	0.703	0.377	0.064	0.114	0.415	2.594
Two	2577.43	2585.25	7.815	1.219	0.156	0.048	0.06	0.086	0.458	3.414
Three	2847.42	2877.6	30.186	29.592	0.98	0.922	0	0.114	0.273	12.561

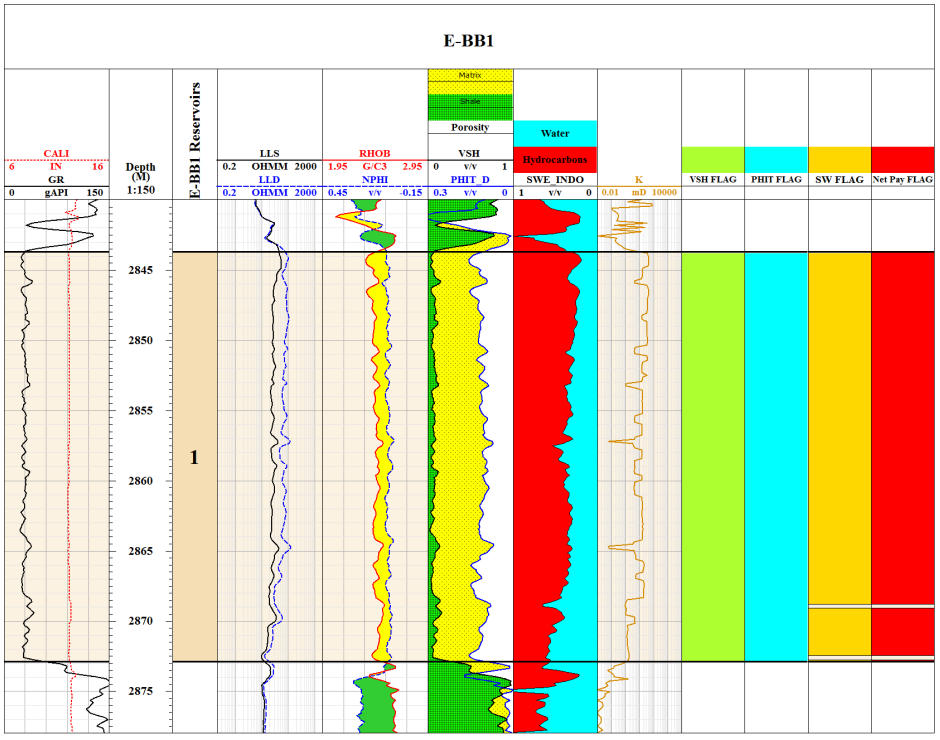

Figure 6.13: Calculated reservoir parameters and net pay interval for reservoir four in E-BB1.

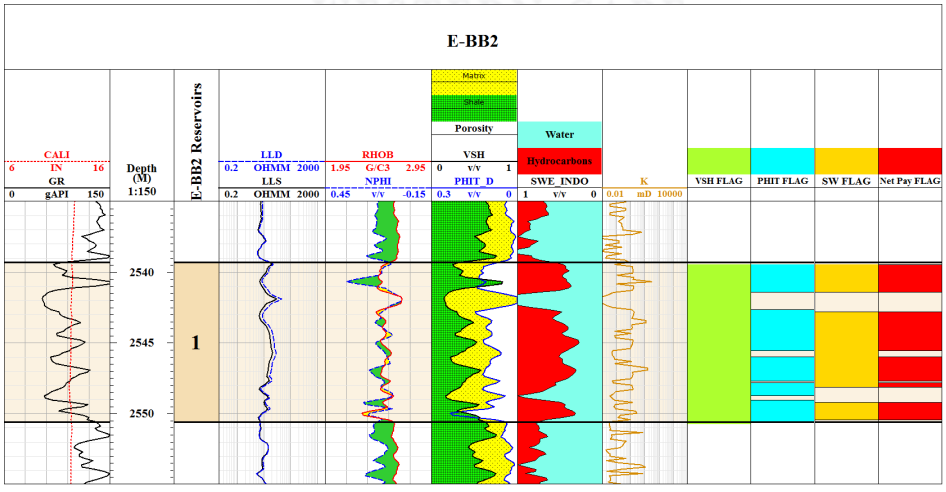

Figure 6.14: Calculated reservoir parameters and net pay interval for reservoir one in E-BB2.

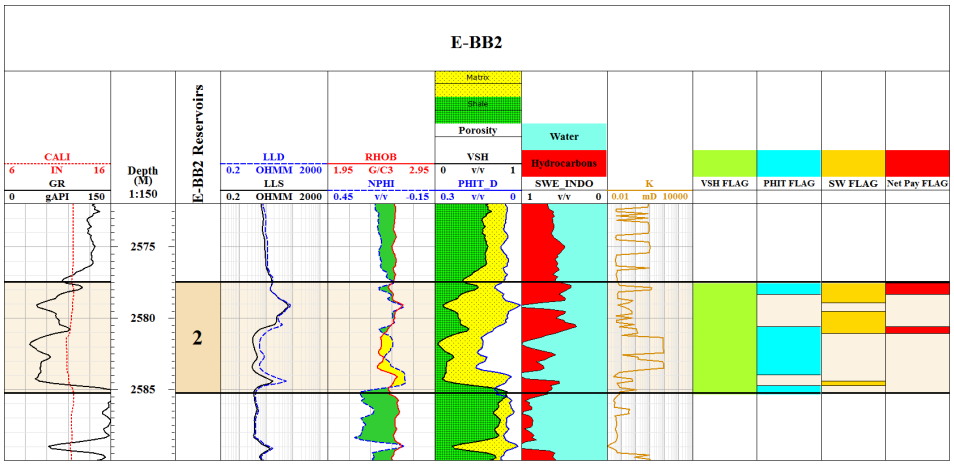

Figure 6.15: Calculated reservoir parameters and net pay interval for reservoir two in E-BB2.

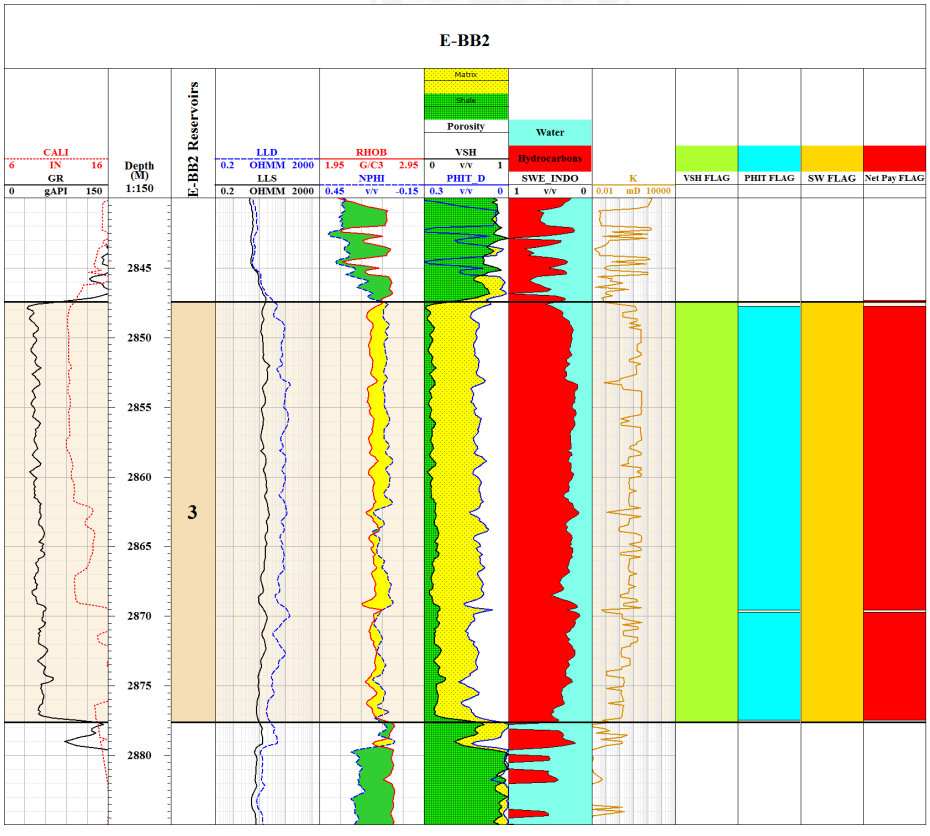

Figure 6.16: Calculated reservoir parameters and net pay interval for reservoir three in E-BB2.

Chapter 7

Conclusions and recommendations

7.1 Conclusions

In this research project; the petrophysical evaluation of 13A and 14A sequences in the central Bredasdorp Basin was been carried out. The study investigated the reservoir units encountered by five wells with insufficient wireline logs and limited core data.

Four different lithofacies were identified from core data according to grain size and sedimentary structure. Facies A and B are recognized as reservoir rocks, whereas facies C and D were considered as non-reservoir rocks. These lithofacies were used to predict the electrofacies from wireline logs in uncored intervals. The classifier used in this prediction resulted in a good match with core facies.

The 13A and 14A sequences boundaries were identified from wireline logs. The sequences range falls between 2570m to 2928m depending on the position of the well. Multi-well correlation between sequences was performed to link these sequences and determine trends between the wells. A total of 13 reservoirs zones were isolated across the depth of the five studied wells.

An integrated approach was used to predict the petrophysical parameters. The available core data and wireline logs were comprehensively analyzed to determine shale volume, porosity, water saturation and permeability. Core data was used to calibrate the petrophysical model.

Six hydraulic flow units were identified in the studied reservoirs by making use of core porosity and permeability. These core flow units were used to predict flow units from wireline logs in uncored intervals. The studied reservoirs were the subject of permeability predictions by hydraulic flow units to consider the complex variation in pore geometry within different rock types.

Net pay determinations were conducted to distinguish between reservoir and non-reservoir rocks. Cut-off values of 7% for porosity, 35% for shale volume, and 60% water saturation were used. The resulting distribution of these estimated petrophysical parameters suggested that the central Bredasdorp Basin is a potential field for gas.

7.2 Recommendations

This petrophysical study could have been more efficient with better quality wireline log data, and more core measurements. Such data could improve log interpretation of the Bredasdorp Basin.

A detailed study and petrophysical evaluation of water saturation is recommended to establish a water saturation model for the Bredasdorp Basin.

References

Adeoti, L., Ayolabi, E., and James, P. (2009). An integrated approach to volume of shale analysis: Niger delta example, orire field. *World Applied Sciences Journal*, 7(4):448–452.

Afify, W. E. and Hassan, A. H. I. (2010). Permeability and porosity prediction from wireline logs using neuro-fuzzy technique. *Ozean Journal of Applied Sciences*, 3(1):157–175.

Ahmed, U., Crary, S. F., Coates, G. R., et al. (1991). Permeability estimation: The various sources and their interrelationships. *Journal of Petroleum Technology*, 43(05):578–587.

Al-Saddique, M. A., Hamada, G., and Al-Awad, M. N. (2000). Recent advances in coring and core analysis technology new technique to improve reservoir evaluation. *Engineering journal of the University of Qatar*, 13.

Alger, R. P. (1980). *Geological use of wireline logs in development in petroleum geology*. Applied science publication London, 2 edition.

Amaefule, J. O., Altunbay, M., Tiab, D., Kersey, D. G., Keelan, D. K., et al. (1993). Enhanced reservoir description: using core and log data to identify hydraulic (flow) units and predict permeability in uncored intervals/wells. *Society of Petroleum Engineers, Annual Technical Conference and Exhibition*, pages 205–220.

Archie, G. E. (1942). The electrical resistivity log as an aid in determining some reservoir characteristics. *Petroleum Technology*, pages 54–62.

Asquith, G. and krygowski, D. (2004). *Basic well Log analysis for geologists*. Number 16. American Association of Petroleum Geologist, Tulsa, Oklahoma, USA.

Balan, B., Mohaghegh, S., and Ameri, S. (1995). State-of-the-art in permeability determination from well log data: Part 1-a comparative study, model development. *Society of Petroleum Engineers*, (30988).

Bassiouni, Z. (1994). *Theory, Measurement, and interpretation of well logs*, volume 4 of *textbook series*. Society of Petroleum Engineers.

Benedictus, T. (2007). Determination of petrophysical properties from well logs of the offshore terschelling basin and southern central north sea graben region (ncp-2a) of the netherlands.

Borhani, T. and Emadi, S. H. (2011). Application of hydraulic flow units and intelligent systems for permeability prediction in a carbonate reservoir. page 6.

Brown, L., Benson, J., Brink, G., Doherty, S., Jollands, A., Jungslager, E., Keenan, J., Muntingh, A., and Van Wyk, N. (1995). *Sequence Stratigraphy in Offshore South African Divergent Basins: An Atlas on Exploration for Cretaceous Lowstand Traps by Soekor (Pty) Ltd.* Number 41. American Association of Petroleum Geologists.

Burden, P. (1992). Soekor, partners explore possibilities in bredasdorp basin off south africa. *Oil and Gas Journal*, pages 109–115.

Burden, P. and Davies, C. (1997). Exploration to first production on block 9 off south africa. *Oil and Gas Journal*, 1(92-98.).

Catuneanu, O., Abreu, V., Bhattacharya, J. P., Blum, M., Dalrymple, R., Eriksson, P., Fielding, C., Fisher, W., Galloway, W., Gibling, M., Giles, K., Holbrook, J., Jordan, R., Kendall, C., Macurda, B., Martinsen, O., Miall, A., Neal, J., Nummedal, D., Pomar, L., Posamentier, H., Pratt, B., Sarg, J., Shanley, K., Steel, R., Strasser, A., Tucker, M., and Winker, C. (2009). Towards the standardization of sequence stratigraphy. *Earth-Science Reviews*, 92:1–33.

Clavier, Huyle, W., and D., M. (1971). Quantitative interpretation of t.d.t logs; part i and ii. *Journal of Petroleum Technology*, 23(6):743–763.

Cluff, S. and Cluff, R. (2004). Petrophysics of the lance sandstone reservoirs in jonah field, sublette county, wyoming. *in Jonah Field: Case Study of a Giant Tight-Gas Fluvial Reservoir American Association of Petroleum Geologists: Studies in Geology*, 52.

Cobb, W. and Marek, F. (1998). Net pay determination and waterflood depletion mechanisms. *Society of Petroleum Engineers 48952, in the Annual Technical Conference and Exhibition.*

De Wit, M. J. and Ransome, I. G. (1992). Regional inversion tectonics along the southern margin of gondwana. *Inversion tectonics of the Cape Fold Belt, Karoo and Cretaceous basins of southern Africa*, pages 15–21.

Ebanks, W. J., Scheihing, M., and Atkinson, C. (1993). Flow units for reservoir characterization. *Development geology reference manual: American Association of Petroleum Geologists: Methods in Exploration Series*, 10:282–285.

Ellis, D. and Singer, J. (2008). *Well Logging for Earth Scientists.* Springer, second edition netherlands edition.

Enikanselu, P. and Adekanle, A. (2008). A fortran programme for computing formation (connate) water resistivity from spontaneous potential logs. *American-Eurasian Journal of Scientific Research*, 3(2):172–177.

Fuad, M. Q. (2008). *Formation Evaluation of Upper Qamchuqa Reservoir, Khabbaz Oil Field, Kirkuk Area, Northeastern Iraq*. PhD thesis, University of Sulaimani.

Galford, J., Flaum, C., Gilchrist Jr., W., Soran, P., and Gardner, J. (1988). Improved environmental corrections for compensated neutron logs. *Society of Petroleum Engineers*, 3, Number 2:371–376.

Gluyas, J. and Swarbick, R. (2004). *Petroleum geoscience*. Oxford: Blackwell Publishing Co.

Gunter, G., Pinch, J., Finneran, J. M., and Bryant, W. T. (1997). Overview of an integrated process model to develop petrophysical based reservoir descriptions. *Society of Petroleum Engineers*, (38748).

Hamada, G. and Abushanab, M. (2008). Better porosity estimate of gas sandstone reservoirs using density and nmr logging data. *Emirates Journal for Engineering Research*, 13(3):47–54.

Kamel., M. H. and Mabrouk., W. M. (2003). Estimation of shale volume using a combination of the three porosity logs. *Journal of Petroleum Science and Engineering*, 40:145–157.

Krygowski, D. A. (2003). *Guide to Petrophysical Interpretation*. Austin Texas U.S.A.

Lehmann, K. (2010). Environmental corrections to gamma-ray log data: Strategies for geophysical logging with geological and technical drilling. *Journal of Applied Geophysics*, 70:17–26.

Liro, L. M. and Dawson, W. C. (2000). Reservoir systems of selected basins of the south atlantic. *in: Mello M.R. and Katz B.J. (eds.), Petroleum system of South Atlantic margins: American Association of Petroleum Geologists Memoir*, 73:77–92.

Masoudi, P., Tokhmechi, B., Zahedi, A., and M., A. J. (2011). Developing a method for identification of net zones using log data and diffusivity equation. *Journal of Mining and Environment*, 2(1):53–60.

McLachlan, I. and McMillan, I. (1976). Review and stratigraphic significance of southern cape mesozoic palaeontology. *Transactions of the Geologic Society of South Africa*, 79(197-212).

McMillan, I., Brink, G., Broad, D., and Maier, J. (1997). Late mesozoic sedimentary basins off the south coast of south africa. *Sedimentary Basins of the World*, 3:319–376.

Mitchum, R., Vail, P., Todd, R., Widmier, J., Thompson, S., Sangree, J., Bubb, J., and W.G, H. (1977). Seismic stratigraphy and changes of sea-level, part 1: Glossary of terms used in seismic stratigraphy. *In: Payton, C.E. (eds.), Seismic stratigraphy and application to hydrocarbon exploration. American Association of Petroleum Geologists Memoir*, 26:205–212.

Moake, G. (2008). An accelerometer- and tension-based depth correction suitable for image logs. *Society of Petrophysicists and Well-Log Analysts*, 2008-UU.

Nooruddin, H. A. and Hossain, M. E. (2011). Modified kozeny-carmen correlation for enhanced hydraulic flow unit characterization. *Journal of Petroleum Science and Engineering*, 80(1):107–115.

Octavian, C. (2006). *Principles of Sequence Stratigraphy*. Elsevier, first edition.

Opuwari, M. (2010). *Petrophsical Evaluation of The Albian Age Gas Bearing Sandstone Reservoir of the O-M Field, Orange basin, South Africa*. PhD thesis, University of the Western Cape.

PASA (2003). Petroleum exploration information and opportunities: Petroleum agency of south africa brochure.

PASA (2004/2005). Petroleum exploration information and opportunities: Petroleum agency of south africa brochure.

PASA (2008). Petroleum exploration information and opportunities: Petroleum agency of south africa brochure.

Poupon, A. and Leveaux, J. (1971). Evaluation of water saturation in shaly formations. *Society of Petrophysicists and Well Log Analysts. 12th Annual Logging Symposium*.

Qi, L. and Carr, T. (2006). Neural network prediction of carbonate lithofacies from well logs, big bow and sand arroyo creek fields, southwest kansas. *Computers and Geosciences*, 32:947–964.

Raymer, L., Hunt, E., and Gardner, J. (1980). An improved sonic transit time-to-porosity transform. *Society of Petrophysicists and Well Log Analysts. 21 Ann. Logging Symposium*.

Rider, M. (1996). *The geological Interpretation of well logs*. Rider-French consulting LTD, second edition.

Schalkwyk, H. J.-M. (2005). Assessment controls on reservoir performance and the affects of granulation seam mechanics in the bredasdorp basin, south africa. Master's thesis, Uniersity of the Western Cape.

Schlager, W. (1999). Type 3 sequence boundaries. *In: Harris, P, Saller, A. and Simo, A. (eds), Carbonate sequence stratigraphy: application to reservoirs, outcrops and models. Society of Sedimentary Geology, Spec. Pub. 63, p. 35-46*.

Schlumberger (1989). *Log Interpretation Charts*. Schlumberger Oilfield Services, Houston.

Selley, R. (2000). *Applied Sedimentology*. Academic Press, San Diego, California, USA., second edition.

Snyder, R. (1971). A review of the concepts and methodology of determining "net pay". *in Fall Meeting of the Society of Petroleum Engineers of AIME1971, New Orleans, Louisiana*.

Soto, B. R., Arteaga, D., Hidalgo, C. M., and Rodriguez, F. (2010). Correct shale-volume characterization increases hydrocarbon reserves: Case study of cretaceous formation lake of maracaibo venezuela. *In Society of Petroleum Engineers Latin American and Caribbean Petroleum Engineering Conference. Society of Petroleum Engineers*, (136811).

Steiber, R. (1973). Optimization of shale volumes in open hole logs. *Journal of Petroleum Technology*, 31:147–162.

Tang, H. and White, C. (2008). Multivariate statistical log log-facies classification on a shallow marine reservoir. *Petroleum Science and Engineering*, 61:88–93.

Thomson, K. (1998). When did the falklands rotate? *Marine and petroleum geology*, 15(8):723–736.

Tinker, J., de Wit, M., and Brown, R. (2008). Linking source and sink: evaluating the balance between onshore erosion and offshore sediment accumulation since gondwana break-up, south africa. *Tectonophysics*, 455(1):94–103.

Ushie, F. (2001). Formation water resistivity (rw) determination: the sp method. *Applied Environmental Manage*, 3:172–177.

Widarsono, B. (2010). Single or multiple porosity cut-off? a new relevange provided by application of a new approach. *LEMIGAS Scientific Contribution*, 33(1):1–8.

Worthington, P. (1991). Effective integration of core and log data. *Society of Core Analysis*, (9102).

Worthington, P. and Consentino, L. (2005). The role of cut-offs in integrated reservoir studies. *Society of Petroleum Engineers Reservoir: Evaluation and Engineering*, 8(4):276–290.

Yumei, L. (2006). Facies identification from well logs : A comparison of discriminant analysis and naive bayes classifier. *Petroleum Science and Engineering*, 53:149–157.

Zee Ma, Y. (2011). Lithofacies clustering using principal component analysis and neural network: Applications to wireline logs. *Mathematical Geosciences*, 43(4):401–419.

Appendices

Appendix A

Well E-BB1 core analysis results

Depth	Φ	K	K Air	Gas	Oil	Water	Grain Density
M	%	md	md	%	%	%	g/cm3
2846.05	13.8	29.05	26.29	70	5	25	2.67
2846.25	11.7	14.56	12.95				2.66
2846.54	13.1	30.06	27.66				2.65
2846.79	13.1	32.17	29.29				2.65
2847.05	13	25.94	23.56	66	4	30	2.66
2847.25	10.1	5.67	4.82				2.65
2847.5	11.2	13.88	12.41				2.65
2847.75	11.5	12.11	10.65				2.65
2848.03	11.2	10.34	9.04	67	5	28	2.65
2848.25	13.1	27.47	24.83				2.64
2848.5	13.2	27.25	24.87				2.65
2848.75	13.8	28.4	25.79				2.67
2849.05	12.6	30.47	28.11	67	0	33	2.65
2849.27	14.4	42.73	39.29				2.65
2849.53	8.9	1.4	1.01				2.66
2849.78	9.3	1.74	1.3				2.66
2850.05	12	16.1	14.44	67	4	29	2.65
2850.25	13.3	29.95	27.49				2.65
2850.47	13.3	22.31	20.03				2.65
2850.72	10.7	5.12	4.27				2.65
2851.05	11.9	9.04	7.78	66	5	29	2.66
2851.22	11.3	7.7	6.5				2.65
2851.46	13.5	20.22	18.19				2.66
2851.72	13.4	17.83	15.81				2.65
2852.03	8.4	0.21	0.1	47	19	34	2.67
2852.29	9	0.89	0.61				2.65
2852.79	12.8	14.33	12.56				2.65
2853.11	13.8	18.48	16.7	73	0	27	2.68

Depth	Φ	K	K Air	Gas	Oil	Water	Grain Density
M	%	md	md	%	%	%	g/cm3
2853.33	12.2	12.12	10.62				2.65
2853.58	11.5	8.19	7.04				2.66
2853.83	11.8	10.33	9				2.65
2854.05	12.5	11.36	9.91	65	4	31	2.67
2854.22	12	12.01	10.49				2.65
2854.51	9.3	1.72	1.25				2.65
2854.76	9.7	2.56	1.97				2.64
2855.05	11.3	5.64	4.68	66	5	29	2.66
2855.22	11.4	7.31	6.15				2.65
2855.47	10.8	6.97	5.87				2.64
2855.72	12.5	11.28	9.7				2.68
2856.05	11.1	3.38	2.65	62	8	30	2.67
2872.05	11.9	18.08	16.45	46	15	39	2.65
2872.27	9.6	3.55	2.88				2.65
2872.57	0.3	0.03	0.02				2.66

Appendix B

Well E-AO1 core analysis results

Depth	Φ	Corrected Φ	K	Corrected K	Water	Oil	Gas	Grain Density
M	%	%	md	md	%	%	%	g/cm3
2674.05	16.1	15.7	111.57	104.8	84	0	16	2.73
2674.3	15.5	14.9	109.31	103.48				2.68
2674.55	15.9	14.4	77.11	72.75				2.67
2674.8	15.3	14.8	96.83	91.54				2.68
2675.05	14.6	14.2	88	82.99	89	0	11	2.68
2675.25	13.8	13.3	55.89	52.74				2.69
2675.5	14	13.5	37.13	35.15				2.69
2675.75	12.7	12.3	10.22	9.6				2.7
2675.9	14.8	14.3	5.19	4.81	63	0	37	2.7
2676.2	14.2	13.5	1.56	1.29				2.68
2676.45	11.9	11.3	1.61	1.38				2.67
2676.7	12.9	12.3	2.15	1.8				2.67
2676.96	14.7	14.1	1.62	1.25	67	0	33	2.68
2677.3	10.4	9.8	0.16	0.09				2.66
2677.55	12.4	11.8	0.69	0.57				2.68
2677.8	12	11.5	1.63	1.32				2.68
2677.97	12.9	12.4	1.64	1.25	59	0	41	2.69
2678.25	11.8	10.9	0.33	0.18				2.68
2678.5	12	11.3	1.36	1				2.68
2678.75	5.5	5	0.04	0.01				2.72
2678.93	11.1	10.6	1.18	0.9	56	0	44	2.7
2679.15	11.7	11.1	1.32	1.08				2.68
2679.4	11.7	11.2	1.21	0.97				2.67
2679.65	11.9	11.3	1.35	1.1				2.67
2679.89	11.5	11.1	1.36	1.16	49	0	51	2.67
2680.2	10.6	10.1	0.28	0.19				2.67
2680.45	10.7	10.4	0.36	0.26				2.68
2680.7	10.4	9.7	0.19	0.12				2.69
2680.89	7.3	6.8	0.12	0.07	48	0	52	2.68
2681.15	7.5	6.9	0.08	0.04				2.68

Appendix C

Uncorrected Porosity and Corrected Porosity in E-BB1

Depth	Uncorrected Porosity	Corrected Porosity
M	%	%
2846.05	13.8	13.15664
2846.25	11.7	11.07651
2846.54	13.1	12.46326
2846.79	13.1	12.46326
2847.05	13	12.36421
2847.25	10.1	9.491648
2847.5	11.2	10.58124
2847.75	11.5	10.8784
2848.03	11.2	10.58124
2848.25	13.1	12.46326
2848.5	13.2	12.56232
2848.75	13.8	13.15664
2849.05	12.6	11.96799
2849.27	14.4	13.75096
2849.53	8.9	8.303002
2849.78	9.3	8.699217
2850.05	12	11.37367
2850.25	13.3	12.66137
2850.47	13.3	12.66137
2850.72	10.7	10.08597
2851.05	11.9	11.27462
2851.22	11.3	10.68029
2851.46	13.5	12.85948
2851.72	13.4	12.76043
2852.03	8.4	7.807733
2852.29	9	8.402056
2852.79	12.8	12.1661
2853.11	13.8	13.15664
2853.33	12.2	11.57178
2853.58	11.5	10.8784
2853.83	11.8	11.17556
2854.05	12.5	11.86894
2854.22	12	11.37367
2854.51	9.3	8.699217
2854.76	9.7	9.095433
2855.05	11.3	10.68029
2855.22	11.4	10.77935
2855.47	10.8	10.18503
2855.72	12.5	11.86894
2856.05	11.1	10.48219